



HAL
open science

Forecasting performance in particle identification with potential TOF detectors at HL-LHC

Antonin Maire

► **To cite this version:**

Antonin Maire. Forecasting performance in particle identification with potential TOF detectors at HL-LHC. 2022. hal-03563619

HAL Id: hal-03563619

<https://hal.science/hal-03563619>

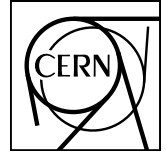
Preprint submitted on 9 Feb 2022

HAL is a multi-disciplinary open access archive for the deposit and dissemination of scientific research documents, whether they are published or not. The documents may come from teaching and research institutions in France or abroad, or from public or private research centers.

L'archive ouverte pluridisciplinaire **HAL**, est destinée au dépôt et à la diffusion de documents scientifiques de niveau recherche, publiés ou non, émanant des établissements d'enseignement et de recherche français ou étrangers, des laboratoires publics ou privés.



Distributed under a Creative Commons Attribution 4.0 International License



Forecasting performance in particle identification with potential TOF detectors at HL-LHC

Antonin Maire *

1. Université de Strasbourg, IPHC, 23 rue du Loess 67037 Strasbourg, France.
2. CNRS/In2p3, UMR7178, 67037 Strasbourg, France.

Analysis note

Upgrade

Abstract

[ANA-1073 - Version 2.0 - (git rev. dummy) - Tuesday 9th March, 2021, 04:57]

The document addresses comparative performances expected for various configurations of Time-Of-Flight detectors, for several CERN experiments (ALICE-1, ALICE-3, ATLAS, CMS). The figures are based on analytical formulae derived for charged particles traveling in a solenoidal magnetic field. While these performances correspond to ideal limits (with respect to real data or full simulations including particle transport), the main point is to assess the theoretical separation among various identified species (e^\pm , μ^\pm , π^\pm , K^\pm , p^\pm , d^\pm , t^\pm , ${}^3\text{He}^{2\pm}$, ${}^4\text{He}^{2\pm}$) at the horizon of runs IV (≈ 2027 -2029) or V (> 2030) of the High-Luminosity LHC, HL-LHC. The intent is thus to appreciate the experimental realm of possible physics cases.

Keywords:

– TOF separation, PID, central barrel, forward endcap / ALICE-1, ALICE-3, ATLAS, CMS / HL-LHC.

26 **Contents**

	I	Introduction : context of the HL-LHC run V	4
28	I-A	Experimental landscape at HL-LHC	4
	I-B	ALICE-3 proposal	4
30	II	Math of time of flight	5
	II-A	Prime equations related to TOF quantities	5
32	II-B	Core working hypotheses : purely helical trajectory	7
	II-C	Parametric equations of the relativistic helical motion	8
34	<u>II-C.i</u>	<i>Differential equation of relativistic motion</i>	8
	<u>II-C.ii</u>	<i>Sketch of the transverse projection (frames and notations)</i>	9
36	<u>II-C.iii</u>	<i>Acceleration vector as a function of time</i>	10
	<u>II-C.iv</u>	<i>Velocity vector as a function of time</i>	12
38	<u>II-C.v</u>	<i>Spatial coordinates as a function of time</i>	13
	II-D	Deriving path lengths and times	14
40	<u>II-D.i</u>	<i>Path length formula for a regular helix</i>	14
	<u>II-D.ii</u>	<i>Date to reach the TOF barrel layer</i>	15
42	<u>II-D.iii</u>	<i>Date to reach the TOF endcap plane</i>	16
	II-E	Visualising concrete helical trajectories calls for comments.....	16
44	<u>II-E.i</u>	<i>Introduction of the trajectory illustrations</i>	16
	<u>II-E.ii</u>	<i>Generic comment 1 : what to be seen actually behind the wording “η acceptance”</i>	22
46	<u>II-E.iii</u>	<i>Generic comment 2 : Helix versus straight-line approximations</i>	22
48	<u>II-E.iv</u>	<i>Generic comment 3 : looper particles spinning towards endcap</i>	23
	II-F	Acceptance thresholds : minimal p_T and inclination angles	24
50	<u>II-F.i</u>	<i>Minimal transverse momentum to reach TOF (barrel and endcap)</i>	24
	<u>II-F.ii</u>	<i>Inclination angle of the track with respect to the barrel detector surface</i> ..	26
52	<u>II-F.iii</u>	<i>Inclination angle of the track with respect to the endcap detector surface</i> .	27
	III	TOF separation power	29
54	III-A	General intent and different configurations	29
	III-B	Typical layout of the figures to come	30
56	IV	Using ALICE-1 in LHC runs I and II as a benchmark exercise	30
	IV-A	Analytics-based performances of the ALICE-1 TOF	34
58	IV-B	Measured performances of the ALICE-1 TOF sub-detector	34
	IV-C	Comparing and discussing analytics and real performances	37
60	<u>IV-C.i</u>	<i>Acceptance \times efficiency to reach TOF</i>	37
	<u>IV-C.ii</u>	<i>Validation with the measured separation among (π^\pm, K^\pm, p^\pm) species</i>	37

62	<u>IV-C.iii</u>	<i>Impact of multiplicity on the overall TOF performance, the start time</i>	38
	<u>IV-C.iv</u>	<i>Light nuclei, illustration with the deuteron identification</i>	39
64	V	Synopsis of the figures and corresponding TOF configurations tested	41
66	VI	Specifications and technological choices, ALICE-3 compared to ATLAS and CMS	48
	VII	TOF measurements in ALICE-3 (HL-LHC run V)	49
68	VII-A	Configuration with a TOF as barrel outer layer at $R = 1$ m	49
	VII-B	Configuration with a TOF as barrel intermediate layer at $R = 0.2$ m	50
70	VII-C	Possibility to have endcap TOF planes	51
	VIII	TOF measurement in CMS (HL-LHC run IV and V)	54
72	IX	TOF measurements in ATLAS (HL-LHC run IV and V)	58
	X	Conclusion	92
74	A	ROOT code snippet	94
	References	102

76 I Introduction : context of the HL-LHC run V

I-A Experimental landscape at HL-LHC

78 At the horizon 2030, the LHC will have already entered its High-Luminosity mode, HL-LHC, normally since one achieved run (Run IV, 2027-2030). By then, the ATLAS and CMS collaborations will have already carried out their major experiment upgrades (during Long Shutdown 3, 2025-2027); the LHCb and ALICE collaborations will be in similar positions, *i.e.* planning to renew their instrumentations in order to pursue/extend their respective physics cases while coping with/making the best of the enhanced instantaneous luminosity available at the time.

84 I-B ALICE-3 proposal

In the context of the European Strategy for Particle Physics (ESPP) initiated in 2018, a proposal for a new experiment has been submitted with the intent to take over the scientific programme from the ALICE-2 apparatus and to be located at Point 2 of the LHC. The timeline foreseen for such a novel instrument would develop along an installation during LHC Long Shutdown 4 (\approx 2030-2032) and a start of operations at HL-LHC run V ($>$ 2032).

90 Such an experiment has been outlined and roughly sketched in an expression of interest entitled *A Next-Generation LHC Heavy-Ion Experiment* [1]. While I have been using the acronym *ANGHIE* as a temporary nickname in the past months including in official presentations¹, as of today, an official acronym, *ALICE-3*, is proposed by the ALICE people interested in such a potential experiment at CERN. If such a name could be subject to yet another change in the coming years, it is for now a name officially approved internally. The intent is not to square the ALICE territory in order to forbid any outsider participation (experimentalists, theoreticians) but is essentially meant to keep a name immediately recognisable by authorities. Such a nickname will be used in the following.

The main physics focuses motivating this original experiment are :

- 100 (i) **quark flavour physics** : a goal is to cover equivalently any measurement in the light-flavour sector ($g + u, d, s$) as in the heavy-flavour one (c, b). This is of particular importance in order to be in position to correlate such observables.
- 102 (ii) **electrons and soft photons** : the QCD physics cases must be enlarged decisively to electromagnetic probes, such probes being at first order insensitive to interactions with the medium, once they are produced by the latter. On that front, studies of chiral symmetry restoration [2] and soft theorems stay [3, 4] the prime targets. Those physics cases have been promoted since several decades but have never been fully at reach : they are known to be especially delicate to address but remain of unique prominence.
- 104 (iii) **hermiticity** : being after an advanced exhaustiveness in the foreseen measurements, the phase space coverage should be widened to the greatest extent, this to get the picture of the particle production as complete as possible, on an event-by-event basis. This is of particular relevance for fluctuation measurements : *i*) the fluctuations stemming from the initial state, propagated in an almost unaltered way, through barely viscous hydrodynamics, up to the final state and *ii*) the fluctuations in net quantum numbers (electric charge, baryon number, strangeness, ...).
- 106
- 108
- 110
- 112
- 114
- 116

¹ Note that this was a temporary shortcut just resorted to for the sake of commodity, *i.e.* to avoid repeated periphrases and to simplify the uniqueness of labelling versus other experiments. It should have been considered as a notation and by no mean as an official acronym already approved by the proto-collaboration or by CERN authorities.

- 118 (iv) **low momentum** : the focus must be given to the phase space areas where the bulk pro-
duction of any identified particle arises, *i.e.* at intermediate ($2 \lesssim p_T < 10$ GeV/ c) and,
120 even more significantly, at low ($0 < p_T \lesssim 2$ GeV/ c) momenta, with special abilities of
detecting properly also in an ultra-low momentum domain ($0.03 \lesssim p_T < 0.15$ GeV/ c).
- 122 (v) **high integrated luminosities** : the statistical reach will be a key value of the ex-
periment. It is not only about the ability of the apparatus to *inspect* steadily high
124 instantaneous luminosity, then potentially trigger on it or, most of the time, not trig-
ger on it; the point is rather to *record* a very large genuine collection of inelastic (\approx
126 Minimum Bias) collisions (*e.g.* $\mathcal{O}(1-10\text{fb}^{-1})$ of pp collisions at $\sqrt{s} = 14$ TeV, having
typically a total inelastic cross-section of 80 mb, thus corresponding to an overall
sample of about 80 000 – 800 000. 10^9 events).

128 By correspondence, such key physics incentives clearly drive the key specifications of the in-
strument :

- 130 (a) **hyper-granularity** with space resolution per layer as low as $\mathcal{O}(3-5)$ μm ,
132 (b) **large pseudo-rapidity coverage** with sub-detectors equipped on $|\eta| < 4$ units,
(c) **moderate magnetic field** with $B \approx 0.2-1.0$ T,
134 (d) **ultra-low material budget** ranging from 0.05% of x/X_0 per layer for innermost lay-
ers to $\mathcal{O}(1)\%$ per layer for outermost ones,
136 (e) **extended particle identification** making use of TOF measurements with timing res-
olution of $\mathcal{O}(10-30)$ ps,
(f) **swift readout** with full-event record of $\mathcal{O}(1)$ MHz.

138 To remain on a realistic path for the 10 years to come, the feasibility of such an experiment
has to be regarded within the scope of concrete detector R&D, of actual technologies that
140 should become both, *i)* mature and *ii)* financially affordable at the horizon 2030. Under those
conditions, extra constraints must be brought to the reader's considerations.

142 The full experiment will have to be installed within a time span of one LHC Long Shutdown
(1.5-2.5 years or so). To that end, the full apparatus is compelled to be rather “compact” and
144 “simple”, *i.e.* the active surface to be equipped needs to remain moderate and the technology
should be essentially ready to be produced along an almost-industrial model. This militates
146 against a vast diversification of technologies brought into operations but rather advocates for
narrowing the choices to a limited set of detector technologies, ideally to a single type, to be
148 applied and declined as needed everywhere in the experiment. For those reasons, the candidate
technology to that purpose could only be at the time being silicon based, more specifically
150 CMOS based.

Figure 1 illustrates the first thoughts given to a such an experiment and gives a schematic view
152 of the possible anticipated layout.

II Math of time of flight

154 II-A Prime equations related to TOF quantities

Generic considerations for equations at stakes for TOF are given in section 4 of [5] and can
156 start from the Lorentz ratio β .

$$158 \quad \beta_{\text{tot}} = \frac{v_{\text{tot}}}{c} \quad (1)$$

$$160 \quad \beta_{\text{tot}} = \frac{\mathcal{L}}{t \cdot c} \quad (2)$$

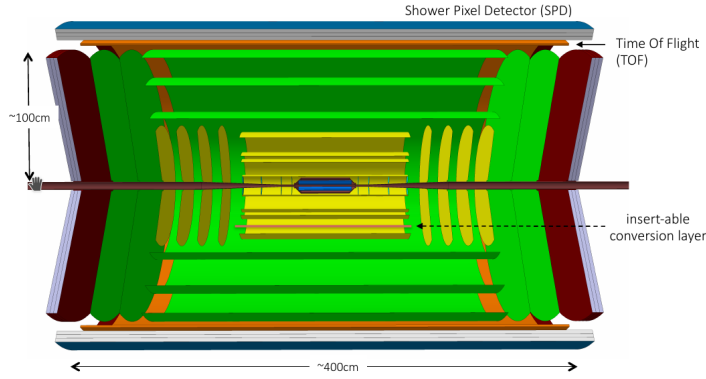


Fig. 1: First detector layout proposed in the early 2019 for the ALICE-3 experiment [1], with barrel covering a pseudo-rapidity range of $|\eta| < 1.4$ and endcaps extending the acceptance to $1.4 < |\eta| < 4.0$. The detector hinges on 3 types of sub-detectors : a pixellated tracker, a pixellated time-of-flight layer and a silicon-sampled electromagnetic preshower.

giving :

$$t_{\text{TOF}} = \frac{\mathcal{L}_{\text{flight}}}{c \cdot \beta_{\text{tot}}} \quad (3)$$

with :

- 164 ■ c the speed of light in vacuum,
- 164 ■ v_{tot} the norm in the 3 spatial dimensions of the velocity \vec{v}_{tot} ,
- 166 associated to Lorentz factors, $\beta_{\text{tot}} = \frac{v_{\text{tot}}}{c}$ (Eq. 1) and $\gamma_{\text{tot}} = \frac{1}{\sqrt{1 - \beta_{\text{tot}}^2}}$, (4)
- 168 ■ t the elapsed time for the particle to cover its flight between two considered points, typically the production and the arrival points,
- 168 ■ \mathcal{L} the integrated path length followed by the particle along such a flight,
- 170 → all these quantities being considered in the laboratory frame.

The TOF separation power $n\sigma_{\text{TOF}}$ between two particle species \mathbb{A} and \mathbb{B} can then be written as a multiple of the overall timing resolution of the TOF detector, σ_{TOF} :

$$n\sigma_{\text{TOF}} = \frac{|t_{\mathbb{A}} - t_{\mathbb{B}}|}{\sigma_{\text{TOF}}} \quad (5)$$

$$n\sigma_{\text{TOF}} = \frac{1}{\sigma_{\text{TOF}}} \cdot \frac{1}{c} \cdot \left| \frac{\mathcal{L}_{\mathbb{A}}}{\beta_{\text{tot},\mathbb{A}}} - \frac{\mathcal{L}_{\mathbb{B}}}{\beta_{\text{tot},\mathbb{B}}} \right| \quad (5a)$$

with the 2 key components :

$$\circ \frac{1}{\beta_{\text{tot},\mathbb{H}}} = \sqrt{1 + \left(\frac{m_{0,\mathbb{H}} \cdot c}{p_{\text{tot},\mathbb{H}}} \right)^2} \quad (6)$$

$$\frac{1}{\beta_{\text{tot},\mathbb{H}}} = \sqrt{1 + \left(\frac{m_{0,\mathbb{H}} \cdot c}{p_{\text{T},\mathbb{H}} \cdot \cosh(\eta_{\mathbb{H}})} \right)^2} \quad (6a)$$

$$[\text{because : } p_{\text{tot},\mathbb{H}} = p_{\text{T},\mathbb{H}} \cdot \cosh(\eta_{\mathbb{H}})] \quad (7)$$

$$\circ \mathcal{L}_{\mathbb{H}} = f(m_{0,\mathbb{H}}, q_{\mathbb{H}}, \eta_{\mathbb{H}}, p_{T,\mathbb{H}}, B) \quad (8)$$

depending on quantities related to the particle of interest, labelled generically \mathbb{H} here :

$$\begin{aligned} & \blacksquare m_{0,\mathbb{H}} && \text{the invariant mass at rest,} \\ & \blacksquare q_{\mathbb{H}} = n_{\mathbb{H}} \cdot e && \text{the electric charge,} \\ & \text{with : } n && \text{multiple of } e \text{ units and } n \in \mathbb{Z}, \text{ set of integers,} \\ & \quad e && \text{the primary electric charge, } e = 1.602\,176\,634 \cdot 10^{-19} \text{ C,} \\ & \blacksquare p_{\text{tot},\mathbb{H}} && \text{the norm of the total momentum,} \\ & \blacksquare \eta_{\mathbb{H}} && \text{the initial pseudo-rapidity,} \\ & \blacksquare p_{T,\mathbb{H}} && \text{the norm of the transverse momentum,} \end{aligned} \quad (9)$$

together with :

$$\blacksquare B \text{ the intensity of the magnetic field in the experiment,}$$

In HEP experiments, a *solenoidal* magnetic field is frequently in place, parallel to the beam axis ($\pm \vec{e}_Z$). This is in particular true for LHC experiments such as ALICE, ATLAS and CMS.

II-B Core working hypotheses : purely helical trajectory

In the above set of equations, it is not obvious *a priori* that $\beta_{\text{tot},\mathbb{H}}$ stays constant over the whole flight, from the primary production point up to the arrival point into the TOF detector, nor that the path itself is smooth or devoid of any sharp point. Indeed, along the way, interactions of various types can happen in the instruments : the trajectory can suddenly change due to multiple Coulomb scattering (direction of \vec{p}_{tot}), to some lineic energy loss happening while crossing material (direction and norm of \vec{p}_{tot}), as well as to quasi-continuous energy losses along the path with processes like bremsstrahlung (direction and norm of \vec{p}_{tot}).

In practice, the integrated time covering the full flight can rather be seen as the sum of segments taken each between two consecutive (particle-to-detector) interactions of such types, the distance $\mathcal{L}_{\text{flight},i}$ and the norm $\beta_{\text{tot},i}$ staying clearly defined in between such dates.

$$t_{\text{TOF}} = \sum_{\text{segment } i} \frac{\mathcal{L}_{\text{flight},i}}{c \cdot \beta_{\text{tot},i}} \quad (10)$$

In order to predict results including such phenomena, it usually entails Monte-Carlo simulations with full particle transport into the numeric detector geometry, addressed with software toolkits such as FLUKA [6] or GEANT4 [7].

Hypothesis 1 | In the current work, the intent is to derive analytically the performance of various TOF detectors. To that end, the ideal case is considered, meaning that along the particle flight, there is **no extra interaction other than the magnetic component of the Lorentz force**, $\vec{f}_L(t) = q \cdot \vec{v}_{\text{tot}} \times \vec{B}$, *i.e.* no energy loss, no scattering, no absorption, no bremsstrahlung, no $\vec{E} \times \vec{B}$ effects, ... are taken into account.

Hypothesis 2 | The magnetic field is assumed to be **perfectly static and homogeneous, exactly aligned along** ($\pm \vec{e}_Z$).

212 After such hypotheses, the exercise can be seen as an assessment of the ultimate performances,
 214 the horizons beyond which the experiments could simply not go. Under various detector con-
 216 figurations for ALICE, ATLAS and CMS, such limits of accessibilities will be posed. The
 consequences of such a strategic bias imply that, along the trajectory, the norm $\|\vec{\beta}_{\text{tot}}\|$ stays
 constant, *i.e.* the direction of \vec{p}_{tot} evolves along with the influence of the sole external mag-
 netic field but $\|\vec{p}_{\text{T}}\|$ and $\|\vec{p}_{\text{Z}}\|$ stay constant along the particle propagation.
 218 We thus fall back to the equation previously listed, Eq. 11.

$$t_{\text{TOF}} = \frac{\mathcal{L}_{\text{flight}}}{c \cdot \beta_{\text{tot}}} \quad (11)$$

220 II-C Parametric equations of the relativistic helical motion

If there is not much ambiguity about the literal expression to be used for β_{tot} (see Eq. 6a), there
 222 are on the other hand various options followed in the literature to approximate the path length,
 \mathcal{L} .

224 Under the aforementioned longitudinal B field configuration, the trajectory of any relativis-
 tic charged particle subjected to the Lorentz force can be represented following at least four
 226 approaches :

- 228 *a) a straight line extending the initial tangent* : derive the path and time as if there were no
 B field, the track thus becomes simply the straight flight continuation of the tangent
 230 to the trajectory at t_0 ($p_{\text{T}}(t_0)$, $\eta(t_0)$), prolonged up to the intersection with the TOF
 layer or plane. This option is likely the spontaneous idea that one may have as a first
 approximation.
- 232 *b) a straight line connecting the primary vertex and the TOF hit location* : such an option re-
 quires significant mathematical derivations, since the actual location ($x(t_f)$, $y(t_f)$, $z(t_f)$)
 234 of the final TOF hit needs to be obtained beforehand. This option is certainly not the most
 natural *a priori* but has the advantage to provide a distance which will remain closely re-
 236 lated to the actual trajectory; for the user, it avoids the integration of the curvilinear path
 length \mathcal{L} .
- 238 *c) a circular arc in the transverse plane* : the bending of the trajectory is now explicitly taken
 into account but the trajectory is only thought through its projection onto the transverse
 240 plane ($O; \vec{e}_x, \vec{e}_y$), ignoring the z component \vec{p}_z ; this provides a fair approximation of the
 situation in the barrel case near mid-rapidity $y \approx 0$.
- 242 *d) a 3D helix segment* : the most generic case meant to work without further approximation,
 for both barrel- and endcap-oriented particles.

244 In this document, the avenue pursued under any experimental configuration is the last one, **op-**
tion (d).

246

II-C.i Differential equation of relativistic motion

248 In order to develop such a line, the parametric equations of motion have been derived, apply-
 ing the fundamental principle of dynamics (FPD) in the relativistic case to a charged particle
 250 immersed into a static and homogeneous magnetic field.

Expressed with the four-force and four-acceleration, the FPD is written like :

$$\underline{\vec{F}} = m_0 \cdot \underline{\vec{A}} \quad (12)$$

$$\underline{\vec{F}} = \left(\gamma_{\text{tot}} \frac{\vec{f} \cdot \vec{v}}{c}, \gamma_{\text{tot}} \vec{f} \right) \quad (12a)$$

with :

$$\blacksquare \vec{f} \cdot \vec{v} = \frac{d}{dt} [\gamma_{\text{tot}}(t) m_0 c^2] = \frac{dE}{dt} \quad (13)$$

$$\blacksquare \vec{f} = \frac{d}{dt} [\gamma_{\text{tot}}(t) m_0 \vec{v}_{\text{tot}}(t)] = \frac{d\vec{p}_{\text{tot}}(t)}{dt} \quad (14)$$

In the present case, with the sole force to be considered being the Lorentz force :

$$\vec{f}_L(t) = q \cdot \vec{v}_{\text{tot}}(t) \times \vec{B} \quad (15)$$

$$\text{It implies that : } \forall t \in \mathbb{R}^+, \vec{f}_L(t) \perp \vec{v}_{\text{tot}}(t) \quad (16)$$

$$\text{so : } \forall t \in \mathbb{R}^+, \vec{f}_L(t) \cdot \vec{v}_{\text{tot}}(t) = 0 \quad (17)$$

$$\text{implying from Eq. 13 : } \forall t \in \mathbb{R}^+, \frac{dE}{dt} = 0 \quad (18)$$

$$\text{and then : } \forall t \in \mathbb{R}^+, \frac{d\gamma_{\text{tot}}}{dt} = 0 \quad (19)$$

Under such circumstances, the energy is conserved along the motion, so do in turn γ_{tot} and $\|\vec{v}_{\text{tot}}\|$. The equation 14 becomes :

$$\vec{f}_L(t) = \frac{d\vec{p}_{\text{tot}}(t)}{dt} \quad (20)$$

$$q \cdot \vec{v}_{\text{tot}}(t) \times \vec{B} = \frac{d\vec{p}_{\text{tot}}(t)}{dt} \quad (20a)$$

$$q \cdot \vec{v}_{\text{tot}}(t) \times \vec{B} = \frac{d}{dt} [\gamma_{\text{tot}} m_0 \vec{v}_{\text{tot}}(t)] \quad (20b)$$

Highlight II.1. *Differential equation of motion for a relativistic charged particle in a static and homogeneous magnetic field, \vec{B} .*

$$q \cdot \vec{v}_{\text{tot}}(t) \times \vec{B} = \gamma_{\text{tot}} m_0 \frac{d\vec{v}_{\text{tot}}(t)}{dt} \quad (20c)$$

270

II-C.ii Sketch of the transverse projection (frames and notations)

Before moving to the resolution of the differential equation, the notations need to be defined. The sketch depicted in Fig. 2 illustrates a projection of the trajectory onto the transverse plane; it highlights the angle $\alpha(t)$ to be considered for the motion of rotation around the curvature centre C , for a particle initiated at the primary vertex O in the laboratory frame.

276

Hypothesis 3

The particles considered here are generically supposed to be **emitted at the exact centre** of the experiment, conveniently coinciding with the origin $O(0,0,0)$ of the laboratory frame. This essentially relates to three assumptions :

- i) the derivations being performed here will only hold for **primary-particle** population (or "primary-like" as are decay products of short-lived resonances directly stemming the primary vertex);
- ii) the accelerator beams are perfectly aligned on the z axis, *i.e.* there is no (x,y) displacement of the beam (typically by a few mm) due to the accelerator optics as well as no further spread of the primary vertices in (x,y) [$\mathcal{O}(\text{mm})$];
- iii) there is no shallow spread of the primary vertices in z [$\mathcal{O}(10 \text{ cm})$] due to any actual length of crossing bunches.

278

Hypothesis 4

Geometry of both TOF barrel layer and endcap plane are considered fully **invariant under rotation** around the axis $(O; \vec{e}_z)$. Let's assume they are indeed plain cylinder and plain ring, respectively, without finite elements that would break the invariance in practice. With such a simplification, starting from the origin $O(0,0,0)$, one can conveniently make a choice for the initial orientation of \vec{p}_T . In the following, whatever will be considered for (m_0, p_T, η) , we will always define trajectories for which $\vec{p}_T(t_0) = +\|\vec{p}_T\| \cdot \vec{e}_x$. Any other case with different initial orientation in azimuth, *i.e.* with an angle, $\varphi(t_0)$, between \vec{e}_x and $\vec{e}_r(t_0)$, can be derived from the previous case by a rotation of each point of the trajectory by $\varphi(t_0)$.

280 Figure 3 shows the frames exploited to derive the solution for Eq. 20c. The math for the moving particle M is primarily performed in the cylindrical frame centered around the curvature
 282 centre $(C; \vec{e}_r, \vec{e}_\varphi, \vec{e}_z)$, before moving back ultimately to the Cartesian coordinate system of the
 laboratory, $(O; \vec{e}_x, \vec{e}_y, \vec{e}_z)$.

284

II-C.iii Acceleration vector as a function of time

286 It follows the expression of the centripetal acceleration, derived in $(C; \vec{e}_r, \vec{e}_\varphi, \vec{e}_z)$.

$$\forall t[s] \in \mathbb{R}^+, \quad \vec{a}_M(t) = -|\rho| \cdot \left(\frac{q B_z}{\gamma_{\text{tot}} m_0} \right)^2 \vec{e}_r \quad (21)$$

288

$$\vec{a}_M(t) = -|\rho| \cdot (\omega_T)^2 \vec{e}_r, \quad (21a)$$

with the 2 notations :

Notation II.1. *Curvature radius which is constant with time.
 (Beware that this is taken here as a signed quantity, depending on q and B_z .)*

$$r(t) \cdot \vec{e}_r(t) \stackrel{\text{not}^\circ}{=} \rho \cdot \vec{e}_r(t),$$

$$\text{with : } \rho = \frac{\|\vec{p}_T\|}{\left(\frac{c \cdot 10^{-9}}{1V} \right) n B_z} \quad (22)$$

290 The units in the present formula may need to be further explicitated here, since they are a bit

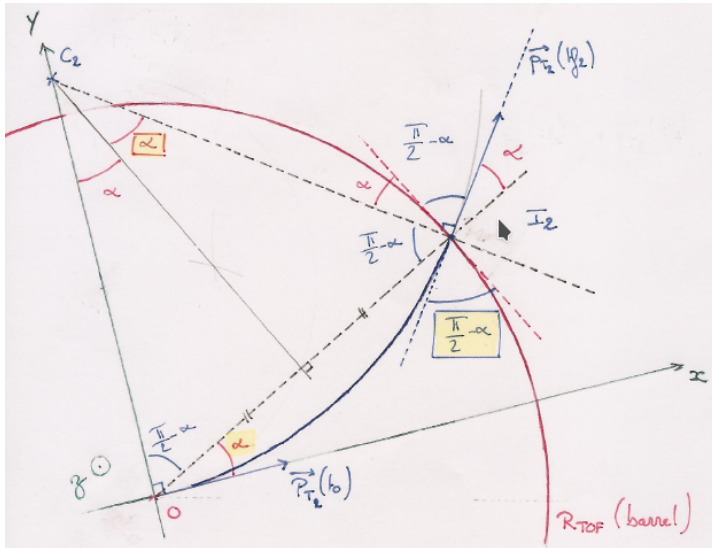


Fig. 2: Sketch introducing the notations for the angles at stakes in the component of motion that is transverse to B field.

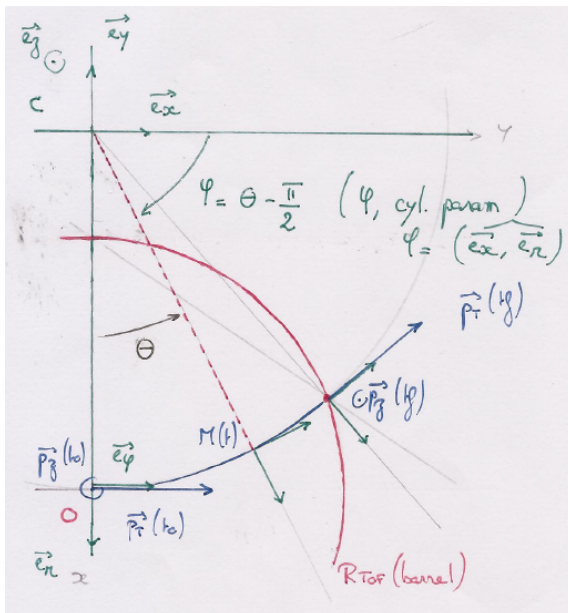


Fig. 3: Sketch laying the frame notations for $(C; \vec{e}_r, \vec{e}_\phi, \vec{e}_z)$ anchored to the centre of rotation C of the motion and for $(O; \vec{e}_x, \vec{e}_y, \vec{e}_z)$ anchored to the lab frame.

The illustration here is outlined for :

- i) $\vec{B} = B_z \cdot \vec{e}_z$ with $B_z < 0$
- ii) $q > 0$.

Note :

- the initial angular position, $\varphi(t_0) = -\pi/2$.
- the curvature radius, $\rho = \overline{CM} \propto (+\vec{e}_r)$ but $\propto (-\vec{e}_y)$.
- the pulsation, $-\omega_T > 0$.

specific for concrete numerical applications that will be performed later.

$$\rightarrow \underbrace{\rho}_{[m]} = \frac{\overbrace{\|\vec{p}_T\|}^{[GeV/c]}}{\underbrace{0.299\,792\,458}_{[m.s^{-1}.V^{-1}]} \underbrace{B_Z}_{[T]} \underbrace{n}_{[\emptyset, \text{multiple of } e \text{ units}]}} \quad (22a)$$

Notation II.2. Larmor angular frequency (or gyromagnetic pulsation) in the relativistic case.

$$\frac{q B_Z}{\gamma_{\text{tot}} m_0} \stackrel{\text{not}^o}{=} \omega_T, \quad (23)$$

Contrary to the situation considered for ρ in Eq. 22, the formula of ω_T has to be considered with standard units, meaning especially that m_0 is expressed in kg.

$$\rightarrow \underbrace{\omega_T}_{[\text{rad}.s^{-1}]} = \frac{\overbrace{(q = n.e)}^{[C]} \overbrace{B_Z}^{[T]}}{\underbrace{\gamma_{\text{tot}}}_{[\emptyset]} \underbrace{m_0}_{[kg]}} \quad (23a)$$

II-C.iv Velocity vector as a function of time

Looking for a primitive defined with the initial conditions on $\vec{v}_{\text{tot}}(t_0)$, one obtains the velocity expression as a function of time :

$$\forall t[s] \in \mathbb{R}^+, \quad \vec{v}_M(t) \stackrel{\text{not}^o}{=} \vec{v}_{\text{tot}}(t) \quad (24)$$

$$\vec{v}_M(t) = \frac{d\vec{CM}}{dt} \quad (25)$$

$$\vec{v}_M(t) = \underbrace{v_\varphi(t)}_{\|\vec{v}_T\|(t)} \cdot \vec{e}_\varphi + v_z(t) \cdot \vec{e}_z \quad (25a)$$

$$\vec{v}_M(t) = v_T(t_0) \cdot \vec{e}_\varphi(t) + v_z(t_0) \cdot \vec{e}_z \quad (25b)$$

$$\vec{v}_M(t) = [-|\rho| \omega_T] \cdot \vec{e}_\varphi(t) + [\beta_z(t_0) c] \cdot \vec{e}_z \quad (25c)$$

$$\vec{v}_M(t) = [-|\rho| \omega_T] \cdot \vec{e}_\varphi(t) + \left[\frac{p_z(t_0)}{E_{\text{tot}}(t_0)} c \right] \cdot \vec{e}_z \quad (25d)$$

β_z expressed here in HEP units (“natural units”),
i.e. ratio of $p_z[\text{GeV}/c]$ and $E_{\text{tot}}[\text{GeV}]$ (“ $c=1$ ” HEP logic)²

Highlight II.2. Velocity vector as a function of time

$$\vec{v}_M(t) = \left[-|\rho| \omega_T \right] \cdot \vec{e}_\varphi(t) + \left[\frac{\|\vec{p}_T\| \sinh(\eta)}{\gamma_{\text{tot}} m_0} c \right] \cdot \vec{e}_z \quad (25e)$$

because :

² In standard units, one would have $\beta_z = \frac{c p_z [\text{kg}.m.s^{-1}]}{E_{\text{tot}} [\text{J}]}$, *i.e.* with an extra c appearing at the numerator.

$$p_z = \underbrace{\|\vec{p}_T\|}_{[\text{GeV}/c]} \sinh(\eta) \quad (26)$$

$$E_{\text{tot}} = \gamma_{\text{tot}} \underbrace{m_0}_{[\text{GeV}/c^2]} \quad (27)$$

As previously done, Eq. 25e can be revised with the perspective of units, revealing on the way what has to be taken for the component v_z .

$$\rightarrow \vec{v}_M(t) = - \underbrace{|\rho|}_{[m]} \underbrace{\omega_T}_{[\text{rad.s}^{-1}]} \cdot \vec{e}_\varphi(t) + \frac{\underbrace{\|\vec{p}_T\|}_{[\text{GeV}/c]} \underbrace{\sinh(\eta)}_{[\emptyset]}}{\underbrace{\gamma_{\text{tot}}}_{[\emptyset]} \underbrace{m_0}_{[\text{GeV}/c^2]}} \underbrace{299\,792\,458}_{[\text{m.s}^{-1}]} \cdot \vec{e}_z \quad (27a)$$

It should be noted that, if the direction of the velocity vector evolves with time, notably due to $\vec{e}_\varphi(t)$, the individual components of the velocity, $\|\vec{v}_T\|$ and $\|\vec{v}_z\|$, are constant with time and, in turn, $\|\vec{v}_{\text{tot}}\|$ is constant as well, as we anticipated earlier. So instead of taking the norm of the aforementioned Eq. 25e, the norm of the velocity can be rewritten into a simpler form (with m_0 in $[\text{GeV}/c^2]$ and $\|\vec{p}_T\|$ in $[\text{GeV}/c]$):

$$\forall t[s] \in \mathbb{R}^+, \quad \|\vec{v}_M(t)\| = \|\vec{v}_{\text{tot}}\| \quad (28)$$

$$\|\vec{v}_M(t)\| = \beta_{\text{tot}} \cdot c \quad (28a)$$

$$\text{(see Eq. 6a)} \quad \|\vec{v}_M(t)\| = \left(\sqrt{1 + \frac{m_0^2}{\|\vec{p}_T\|^2 \cosh^2(\eta)}} \right)^{-1} \cdot c \quad (28b)$$

II-C.v Spatial coordinates as a function of time

The last integration step leads to the spatial coordinates of the relativistic motion, taking into account initial positions, first for \vec{CM} and finally for \vec{OM} in $(O; \vec{e}_x, \vec{e}_y, \vec{e}_z)$. The set of parametric equations is meant to be generic to accommodate the possible change of sign for the B_z configuration ($\pm \vec{e}_z$) together with the sign of the electric charge of the particle of interest ($q = n \cdot e < 0$ or $q > 0$), leading to 4 configurations of $[B_z, q]$ to consider.

Highlight II.3. Parametric equations of the spatial coordinates as a function of time, for a charged particle propagating into a static and homogeneous magnetic field, $\vec{B} = B_Z \vec{e}_Z$, expressed in the frame at rest in the laboratory (O ; $\vec{e}_x, \vec{e}_y, \vec{e}_z$).

$$\forall t[s] \in \mathbb{R}^+, \quad \vec{OM}(t) = \frac{\overbrace{\|\vec{p}_T\|}^{-\rho}}{0.299\,792\,458\,nB_Z} \sin\left(\frac{\omega_r}{\underbrace{\gamma_{\text{tot}} m_0}} t\right) \cdot \vec{e}_x$$

$$+ \frac{\|\vec{p}_T\|}{0.299\,792\,458\,nB_Z} \left[\cos\left(\frac{neB_Z}{\gamma_{\text{tot}} m_0} t\right) - 1 \right] \cdot \vec{e}_y$$

$$+ \underbrace{\left[\frac{\|\vec{p}_T\| \sinh(\eta)}{\gamma_{\text{tot}} m_0} c t \right]}_{\beta_z} \cdot \vec{e}_z \quad (29)$$

$$\text{with : } \gamma_{\text{tot}} = \sqrt{1 + \frac{\|\vec{p}_{\text{tot}}\|^2}{m_0^2}} = \sqrt{1 + \frac{\|\vec{p}_T\|^2 \cosh^2(\eta)}{m_0^2}} \quad (30)$$

328

Note in particular that n and B_Z are considered as signed quantities and that the equations encompass a two-fold logic as far as the units are concerned, depending on the considered term : ρ (Eq. 22a), β_z (Eq. 26 combined with Eq. 27) and γ_{tot} (Eq. 30) abide by the HEP units hinged on GeV; ω_r follows the standard physics units, as exposed in Eq. 23a. All in all, t has to be in [s] and the 3 space components of $\vec{OM}(t)$ will be in [m].

334

The vectorial equation 29 is meant to cover both trajectory cases, should it hit a barrel layer or an endcap plane, and to work for particle rotations for which the *absolute* angle around the curvature centre C stays within $[0; +\pi]$ (barrel and endcap) but also rotations which cover more than a half-turn ($[+\pi; \infty[$, “looper tracks” met in the endcap case).

336

338 II-D Deriving path lengths and times

II-D.i Path length formula for a regular helix

340

After the derivation of the parametric equations, one can calculate the actual quantities of interest, the path length \mathcal{L} and the time needed to cover such a curvilinear distance, t_{TOF} , introduced in Eq. 5a. Starting from the curvilinear abscissa s along the curve, the path length is the integral from the starting time t_0 to the final one t_f .

342

344

$$\mathcal{L} = \int_{t_0}^{t_f} ds \quad (31)$$

$$\mathcal{L} = \int_{t_0}^{t_f} \|\mathrm{d}\vec{CM}\| = \int_{t_0}^{t_f} \|\mathrm{d}\vec{OM}\| \quad (31a)$$

346

$$\mathcal{L} = \int_{t_0}^{t_f} \left\| \frac{\mathrm{d}\vec{OM}}{\mathrm{d}t} \right\| \mathrm{d}t \quad (31b)$$

$$\mathcal{L} = \int_{t_0}^{t_f} \|\vec{v}_{\text{tot}}\| \mathrm{d}t \quad (31c)$$

348 Since $\|\vec{v}_{\text{tot}}\|$ is constant with time (see Eq. 28b), the path length can finally be expressed as :

$$\mathcal{L} = \|\vec{v}_{\text{tot}}\| \int_{t_0}^{t_f} dt \quad (31d)$$

350
$$\mathcal{L} = \|\vec{v}_{\text{tot}}\| [t]_{t_0}^{t_f} \quad (31e)$$

Highlight II.4. Path length along the regular helical trajectory covered by a (relativistic) charged particle in a static and homogeneous magnetic field.

$$\mathcal{L} = \|\vec{v}_{\text{tot}}\| t_f \quad (31f)$$

352 From the above equation, $\|\vec{v}_{\text{tot}}\|$ being known from the initial conditions (Eq. 28b), it is now understood that the whole stress to assess the path length is in fact reported onto the determination of the date t_f , for either the flight to reach the barrel layer or the endcap plane.

354 **II-D.ii** *Date to reach the TOF barrel layer*

356 In the barrel case, the TOF layer is reached when the transverse location is equal for the first time to the TOF radius. We look for :

$$t_f \in \mathbb{R}^+ \quad / \quad \|\vec{OM}(t_f) \cdot \vec{e}_r\| = R_{\text{TOF}} \quad (32)$$

358 i.e.
$$t_f \quad / \quad \sqrt{x^2(t_f) + y^2(t_f)} = R_{\text{TOF}} \quad (33)$$

360 Using the abscissa and ordinate components defined in Eq. 29 to solve this equation, we obtain :

Highlight II.5. TOF date in the barrel case.

$$t_f^{\text{barrel}} = \frac{1}{|\omega_T|} \arccos\left(1 - \frac{R_{\text{TOF}}^2}{2\rho^2}\right) \quad (34)$$

$$= \frac{\gamma_{\text{tot}} m_0}{|n e B_Z|} \arccos\left(1 - \frac{R_{\text{TOF}}^2}{2} \frac{[0.299\,792\,458 |n B_Z|]^2}{\|\vec{p}_T\|^2}\right) \quad (34a)$$

alternatively :
$$t_f^{\text{barrel}} = \frac{1}{|\omega_T|} 2 \arcsin\left(\frac{R_{\text{TOF}}}{2|\rho|}\right) \quad (35)$$

see Eq. 30

$$= \frac{\gamma_{\text{tot}} m_0}{|n e B_Z|} 2 \arcsin\left(\frac{R_{\text{TOF}}}{2} \frac{0.299\,792\,458 |n B_Z|}{\|\vec{p}_T\|}\right) \quad (35a)$$

leading to :
$$\mathcal{L} = \underbrace{\|\vec{v}_{\text{tot}}\|}_{\text{see Eq. 28b}} t_f^{\text{barrel}} \quad (36)$$

$$(37)$$

II-D.iii Date to reach the TOF endcap plane

362 In the endcap case, the TOF plane is reached when the longitudinal position is equal to the TOF location in z . We look for :

$$364 \quad t_f \in \mathbb{R}^+ \quad / \quad \|\overrightarrow{OM}(t_f) \cdot \vec{e}_z\| = Z_{\text{TOF}} \quad (38)$$

$$\text{i.e. } t_f \quad / \quad z(t_f) = Z_{\text{TOF}} \quad (39)$$

366 Using the longitudinal component defined in Eq. 29 to solve this equation, we obtain :

Highlight II.6. *TOF date in the endcap case.*

$$t_f^{\text{endcap}} = \frac{|Z_{\text{TOF}}|}{|v_z|} = \frac{|Z_{\text{TOF}}|}{|\beta_z c|} \quad (40)$$

$$= |Z_{\text{TOF}}| \frac{\gamma_{\text{tot}} m_0}{\|\vec{p}_T\| |\sinh(\eta)| c} \quad (\eta \neq 0) \quad (40a)$$

$$\text{leading to : } \mathcal{L} = \underbrace{\|\vec{v}_{\text{tot}}\|}_{\text{see Eq. 28b}} t_f^{\text{endcap}} \quad (41)$$

$$\text{in fact : } \mathcal{L} = |Z_{\text{TOF}}| \frac{1}{|\tanh(\eta)|} = |Z_{\text{TOF}}| \frac{\|\vec{p}_{\text{tot}}\|}{|p_z|} \quad (41a)$$

368 In the present situation, the path length turns out to be only function of Z_{TOF} and η , and this way, independent of B_z . Should B_z be zero, be of small value or be set to a large one, once p_T and p_z are decided at t_0 , the Larmor radius will admittedly get smaller and smaller for increasing magnetic field but the corresponding path length will be in any case the same.

372

II-E Visualising concrete helical trajectories calls for comments...*II-E.i Introduction of the trajectory illustrations*

374 Before moving into the actual map in (p_T, y) of the TOF separation for various species, it could be profitable to illustrate some aspects of helical trajectories, based on a few selected cases. There are indeed several subtleties that the reader should be made aware of beforehand.

378 For such a purpose, we will use the configuration foreseen for the CMS detector in run IV (2027-2029) at HL-LHC, it is the first experiment planning to be concretely instrumented with both a barrel- and an endcap TOF [8].

380 On the one hand, Figs. 4 and 5 are examples of trajectories for a proton and an antiproton, respectively, both reaching the TOF barrel, placed at a radial position of $R_{\text{TOF}} = 1.16$ m. Figure 6 is also derived for a proton reaching the TOF barrel layer, but for a higher p_T . On the other hand, Figs. 7, 8 and 9 embody three cases of trajectories towards the endcap plane, located at $Z_{\text{TOF}} = 3.04$ m.

386 For each figure, the initial kinematic hypotheses are given (m_0 , q , p_T , η and β_{tot}), together with the detector key characteristics (B_z , σ_{TOF} , R_{TOF} , Z_{TOF}). Beyond the simple visualisation of the trajectories, the outcome in the figures also includes quantitative pieces of information. It concerns :

- 390 (i) the TOF hit itself such as its location $x(t_f), y(t_f), z(t_f)$,
- 392 (ii) the overall rotation and the Larmor radius, both imprinted by the magnetic field,
- 394 (iii) three path lengths and associated times t_f to cover such flight distances
- the exact one, \mathcal{L} , along the curvilinear path (solid green curve) standing for option
 - 396 (d) among the possibilities described p.8
 - the straight segment, a , along the tangent to the helix at the origin ($O; 0,0,0$)
 - 398 prolonged up to the TOF detector, displayed as a diagonal dotted azure line in
 - figures, standing for approximation (a) given on the same page 8.
 - the straight segment, b , connecting the origin ($O; 0,0,0$) to the TOF hit, displayed
 - 400 as the diagonal dashed olive line in figures, standing for approximation (b) given
 - on p.8.

Both distances a and b are further related to \mathcal{L} via their respective difference and ratio to the

402 curvilinear distance, the same comparisons are also performed for the pair of corresponding time

t_f . The intent with such tests is to assess down to which point a straight line approximation

404 holds for a given σ_{TOF} anticipated, *i.e.* is the straight-line approximation transparent for our

performance study so that any difference is absorbed under the blurring of σ_{TOF} ? or is it like

406 the approximation is too coarse so that the TOF results become clearly altered by it ?

Out of such illustrations of trajectories, several generic comments emerge.

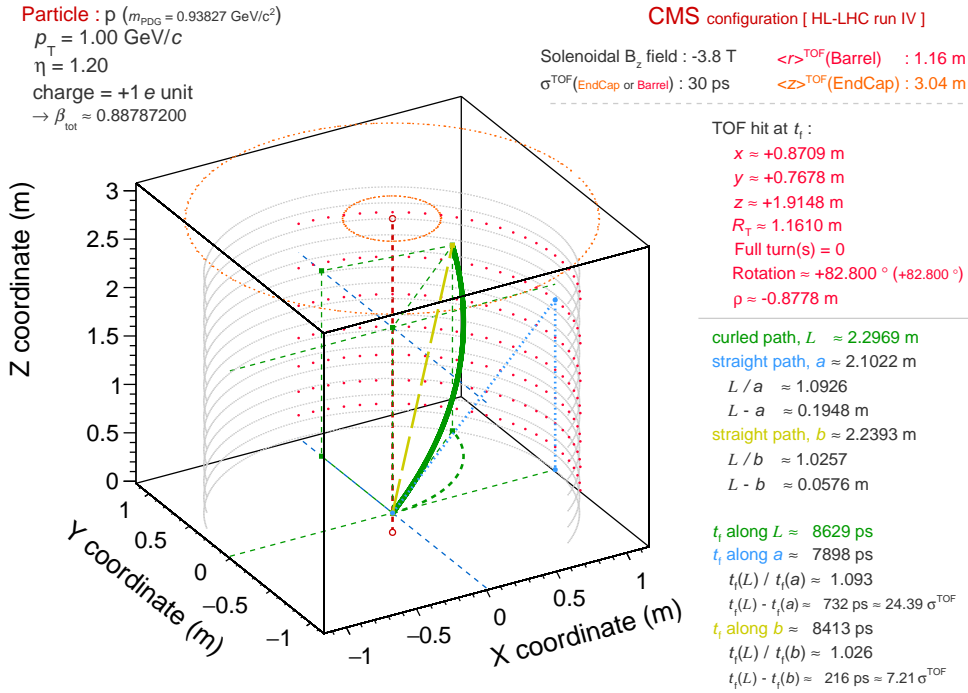


Fig. 4: Helical trajectory for a proton of $p_T = 1.0 \text{ GeV}/c$ with $\eta = 1.2$, emitted with $\vec{p}_T(t_0)$ along $+\vec{e}_X$ direction, into the standard CMS configuration foreseen for the barrel pile-up tagger (MTD-BTL) at the HL-LHC run IV (2027-2029).

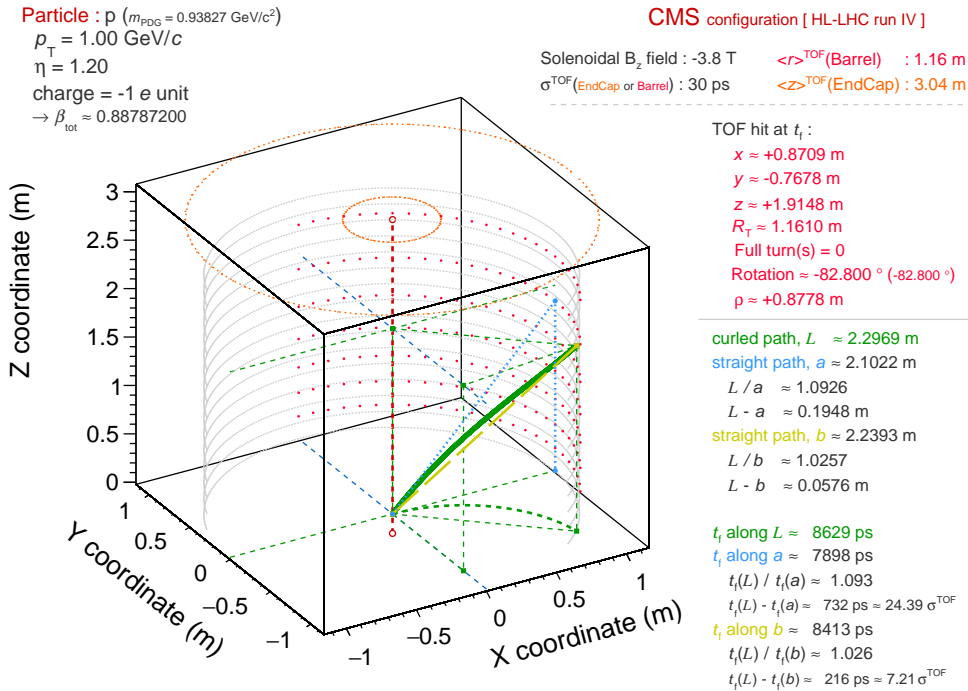


Fig. 5: Helical trajectory for an antiproton of $p_T = 1.0 \text{ GeV}/c$ with $\eta = 1.2$, emitted with $\vec{p}_T(t_0)$ along $+\vec{e}_X$ direction, into the standard CMS configuration foreseen for the barrel pile-up tagger (MTD-BTL) at the HL-LHC run IV (2027-2029).

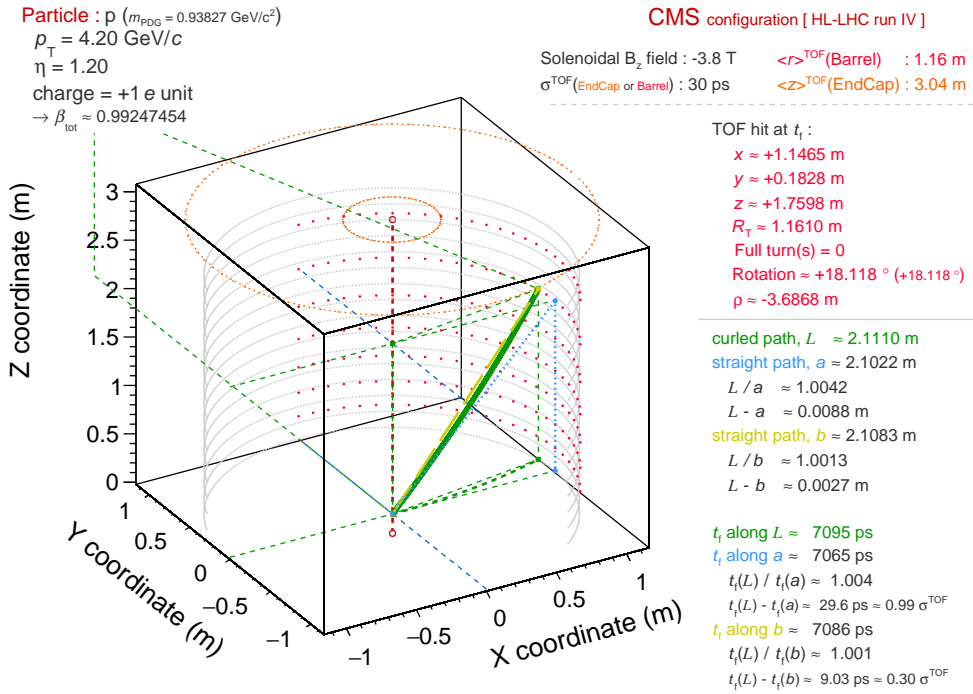


Fig. 6: Helical trajectory for an antiproton of $p_T = 4.20 \text{ GeV}/c$ with $\eta = 1.2$, emitted with $\vec{p}_T(t_0)$ along $+\vec{e}_x$ direction, into the standard CMS configuration foreseen for the barrel pile-up tagger (MTD-BTL) at the HL-LHC run IV (2027-2029).

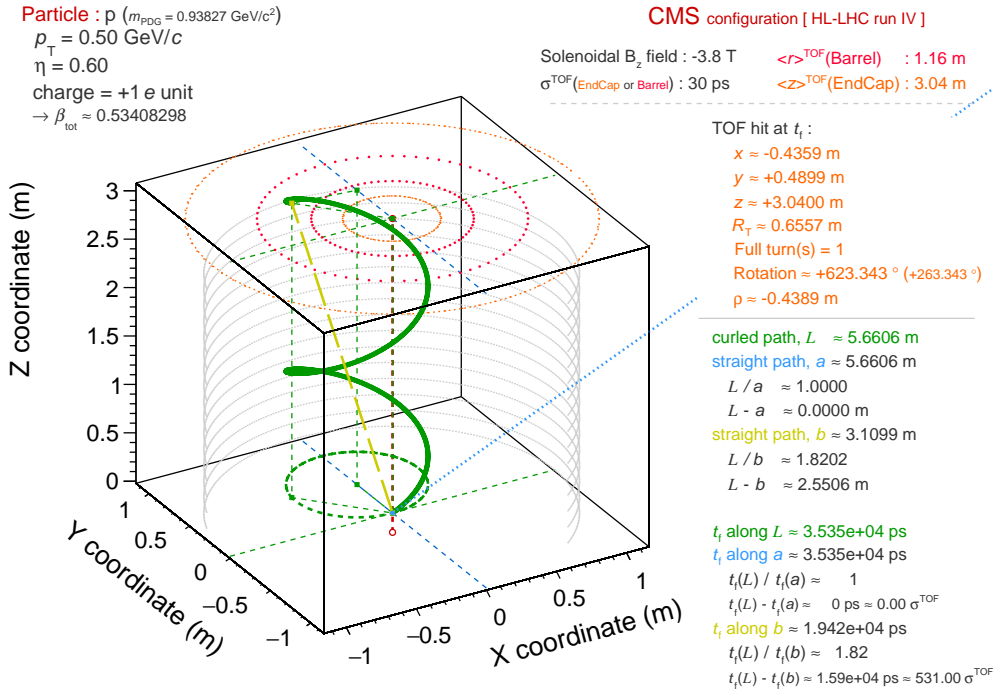


Fig. 7: Helical trajectory for a proton of $p_T = 0.5 \text{ GeV}/c$ with $\eta = 0.6$, emitted with $\vec{p}_T(t_0)$ along $+\vec{e}_x$ direction, into the standard CMS configuration foreseen for the endcap pile-up tagger (MTD-ETL) at the HL-LHC run IV (2027-2029).

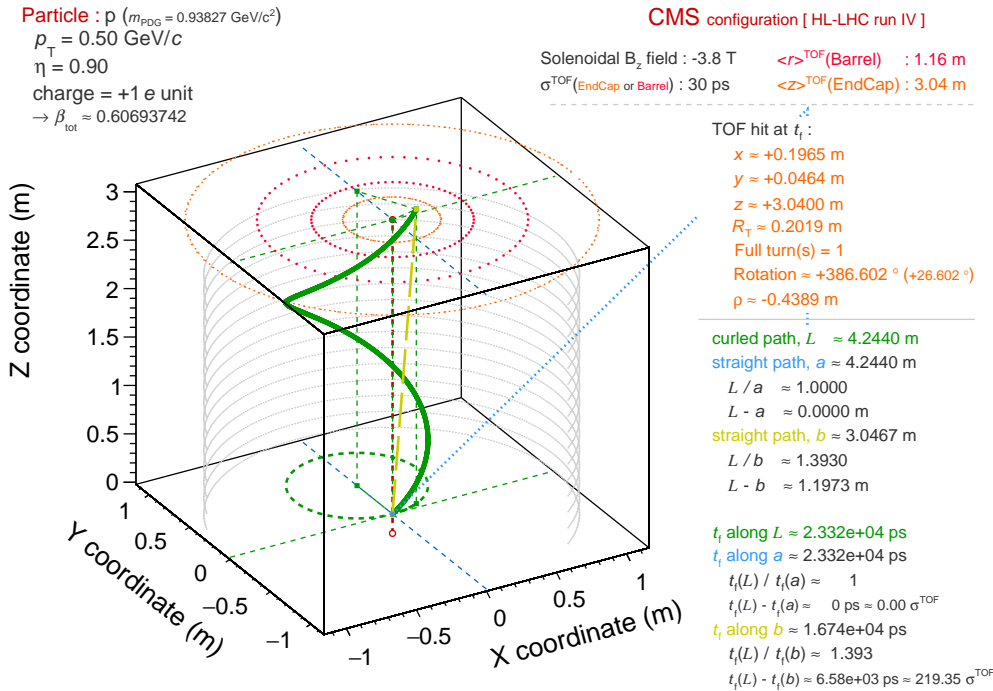


Fig. 8: Helical trajectory for a proton of $p_T = 0.5 \text{ GeV}/c$ with $\eta = 0.9$, emitted with $\vec{p}_T(t_0)$ along $+\vec{e}_x$ direction, into the standard CMS configuration foreseen for the endcap pile-up tagger (MTD-ETL) at the HL-LHC run IV (2027-2029).

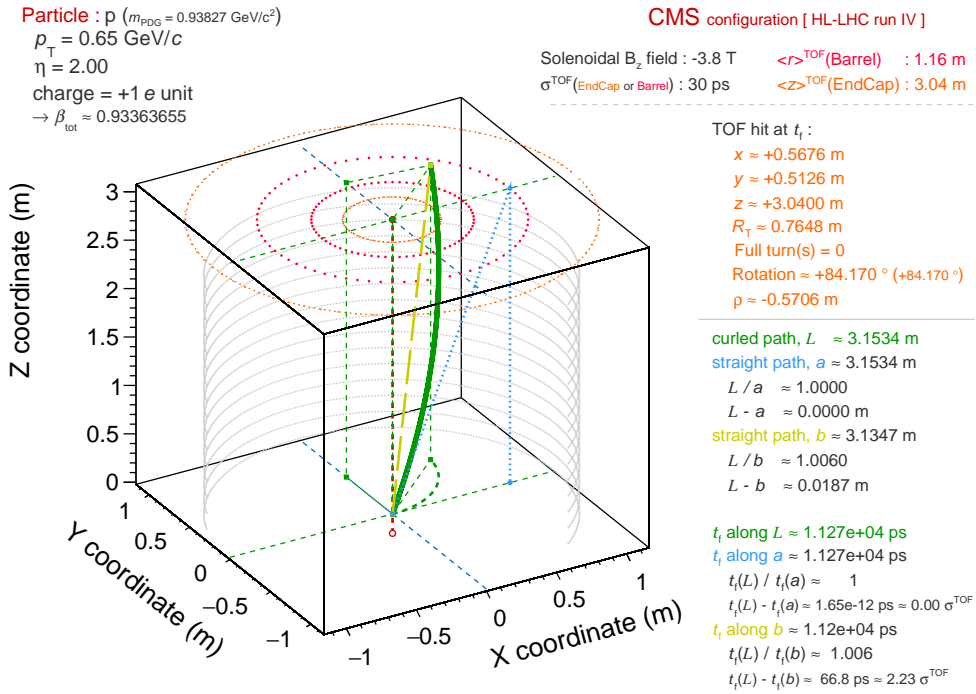


Fig. 9: Helical trajectory for a proton of $p_T = 0.65 \text{ GeV}/c$ with $\eta = 2.0$, emitted with $\vec{p}_T(t_0)$ along $+\vec{e}_x$ direction, into the standard CMS configuration foreseen for the endcap pile-up tagger (MTD-ETL) at the HL-LHC run IV (2027-2029).

408 II-E.ii *Generic comment 1 : what to be seen actually behind the wording “ η acceptance”*

410 It is quite casual to quote the zenithal acceptance of a given sub-detector in terms of pseudo-
 412 rapidity. For instance, the detector MTD-BTL for CMS is meant to cover “up to ± 1.48 units
 of η ” (sec. 2.1 p.29 in [8]). However such a sentence has to be read as a shortcut to the ac-
 414 tual situations met in concrete detection. Behind the scene, it is silently assuming the case of
 straight tracks, so particle of infinite p_{tot} on which the solenoidal magnetic field has barely an
 influence. That means that the track is very near the straight prolongation of the direction taken
 416 originally, defined by the tangent to the curve at t_0 time. In practice, seen from the TOF point
 of view, the particle will always have an “apparent” η which is larger... Such a sentence may
 418 look odd to the reader : the pseudorapidity is a kinematic property of the particle; in the ideal
 case pursued in the present document, there is no reason for it to change along the trajectory,
 420 isn’t there ? - It is tried to be more concrete in the following.

In the barrel, the final location $z(t_f)$ will always be larger than what is anticipated as $z(t_f)$ for
 422 a straight track being the continuation of the initial tangent at t_0 . In Fig. 4, the proton is defined
 with $\eta = 1.20$. The final $z(t_f)$ is equal to 1.9148 m, This corresponds to the final z position
 424 of a straight track of $\eta = 1.27$. In the figure, the dotted red arc circles drawn along the TOF
 cylinder stand for the apparent η of $+0.2k$ with $k \in \llbracket 1; 7 \rrbracket$; the curled trajectory arrives beyond
 426 such a dotted line at $\eta = 1.2$.

In the endcap, the final transverse radius of the TOF hit will always occur at a lower radius
 428 than what is anticipated for the straight track characterised by the initial η . In Fig. 9, the final
 hit is located below the ring representing the apparent η of 2.0, at a final radius $r_T = 0.7648$ m,
 430 corresponding to an apparent $\eta = 2.09$.

It is clear that such differences vanish as p_{tot} grows. The concrete consequence of this is that
 432 the actual acceptance in η is in fact B -field and/or momentum-dependent³ : such an acceptance
 is in fact narrower than the announced number, the latter being only the limit case for high-
 434 momentum track. For instance, in the CMS MTD case, for a track of $p_T = 0.661$ GeV/c,
 the maximum acceptance of the barrel BTL is in fact reduced from ($\eta = \pm 1.48$) down to
 436 ($\eta \approx \pm 1.12$), that is a difference of ± 0.36 units in η . For a track of $p_T > 3.5$ GeV/c, the barrel
 acceptance of the CMS MTD becomes indeed close to ± 1.48 in η . For the endcap, we can gain
 438 a bit of acceptance on the low η side, since particle a priori expected outside the endcap η may
 finally sneak in nearby the outer radius of the instrumented disk. At the inner ring, towards
 440 the maximum η , we loose again some η acceptance. Note that, in the endcap case, the gains
 and losses in η will be more moderate than in the central barrel region, and the p_T needed to
 442 converge towards the limit acceptance is lowered : with growing η , p_z and, in turn, p_{tot} , are
 growing faster than at mid-rapidity. For instance, a track of $p_T = 0.661$ GeV/c and $\eta = 1.61$
 444 will hit the endcap at $r_T = 1.0356$ m thus giving a apparent η of 1.80, *i.e.* $+0.2$ η units, a
 $p_T > 2.5$ GeV/c only (*i.e.* not 3.5 GeV/c as in the barrel case above) is enough to look like a
 446 straight track. For $p_T = 0.661$ GeV/c but $\eta = 3.00$, the particle escapes the endcap acceptance
 below the ETL inner radius by less than 3 mm, corresponding already to less than 0.01 unit of
 448 η .

450 II-E.iii *Generic comment 2 : Helix versus straight-line approximations*

The various figures discussed in the previous sub-section give a glimpse of the straight line
 452 approximations with respect to the helical computation. In the casual cases where particle per-

³ The η acceptance is not species-dependent on the other hand : once p_T , η and thus p_z are fixed, any particle species will follow the same helical path, but with a velocity which will then depend on m_0 so with a different timing.

454 form less than half a turn before reaching the TOF detector, barrel or endcap, the difference in
 455 terms of covered distances often reduces to several centimeters over a flight distance necessar-
 456 ily ranging above the R_{TOF} or Z_{TOF} values, so above $\mathcal{O}(1 \text{ m})$ usually. As a length difference, this
 457 can easily be perceived as something relatively negligible. In the TOF perspective, one can be
 458 all the more comforted into such an intuition that particles typically travel at highly relativistic
 459 velocities (*e.g.* for a proton of $p_T = 0.661 \text{ GeV}/c$, β_{tot} ranges from 0.57 at $\eta = 0$ to 0.99 at
 460 $\eta = 3.0$), so a few cm more covered at a velocity close to speed of light should not make much
 461 difference in terms of time ($t = l/v$) at the end of the flight... However, TOF detectors that we
 462 are considering here, be they from ALICE, ATLAS or CMS, typically have a time resolution
 463 $\sigma_{\text{TOF}} \mathcal{O}(10 - 10^2 \text{ ps})$. And an extra 5-cm distance covered at $1.0 c$ already leads to a time sup-
 464 plement of 166 ps, meaning already several σ_{TOF} apart. The straight line approximations can
 465 thus easily falsify the TOF results and should be considered with caution, such approximations
 466 being most of the time everything but neutral in view of the timing resolution at stakes.

466 “*Most of the time*” ... Among the cases proposed by the illustrative figures, the reader may
 467 need to stop on the endcap cases (Figs. 7, 8, 9). There is indeed a peculiarity that must be
 468 underlined : in any endcap case, the approximation (a) is in fact not an approximation any-
 469 more: moving with β_{tot} along the tangent at t_0 to the trajectory, further prolonged up to the
 470 TOF endcap, yields in fact the exact same length and time as for the associated helix path, as
 471 announced already in subsection II-D.iii. In the endcap figures, to be concrete, it means that
 472 the length of the straight azure dotted line and of the curled solid green line are the same.

473 The fact that the path length towards the endcap is independent of B_z (Eq. 41a) implies that
 474 “approximation” (a) is an alternative but equivalent way to determine the value of the curvilinear
 475 length \mathcal{L} . The determination of \mathcal{L} boils down to the determination of the length covered
 476 by the trajectory followed by the particle under all the same initial conditions (η , p_T , m_0 , ...)
 477 except the dummy condition of $B_z = 0$, so when the trajectory becomes naturally straight. The
 478 reason for this counter-intuitive fact is due to the magnetic force $\vec{f}_L(t)$ which does not apply
 479 any work along \vec{e}_z direction ($\forall t, \vec{f}_L(t) \perp B_z \vec{e}_z$, so $\vec{f}_L(t) \cdot \vec{v}_z = 0$), so that the time to cover a
 480 certain z distance should remain constant once the ratio $\|\vec{p}_{\text{tot}}\|/\|\vec{p}_z\|$, *i.e.* the inclination angle
 481 between the velocity components, is set.

482

II-E.iv Generic comment 3 : looper particles spinning towards endcap

484 Looking at Figs. 7 and 8, the reader is driven to consider that the TOF endcap can become a low-
 485 p_T TOF detector for mid-rapidity particles. In the case of small p_T , the particle may be unable
 486 to reach the TOF barrel layer, the Larmor radius being too small for that; it will instead start to
 487 loop towards the encap plane, driven by the p_z momentum. Exploring this singular possibility
 488 requires the tracking algorithms of the experiment to be tailored to quest looper tracks. This
 489 tracking feature may come with 2 limits. *i)* In practice, low momentum particle are of course
 490 more vulnerable to multiple scattering, absorption, ... On the looping path towards endcap, the
 491 particle will multiply the chances to be scattered, especially by crossing many layers which
 492 are usually of increasing radiation length X/X_0 as one goes away from mid-rapidity towards
 493 forward or backward directions. *ii)* Provided that multiple scattering is not dooming the full
 494 idea, the detection is not granted under any circumstances *a priori*. Figure 8 illustrates a point
 495 of phase space ($p_T(t_0)$, $\eta(t_0)$, $\phi(t_0)$) for which the particle escapes finally the TOF endcap
 496 acceptance, arriving at the end of the flight into the inner part of the endcap plane which is not
 497 instrumented, next to the beam pipe, below the inner radius of the detector. Even in the ideal
 498 case exposed in this document, due to simple geometric considerations and the way the helix
 499 evolves, there will be some deadzones in phase space for detecting looper particles.

500 **II-F Acceptance thresholds : minimal p_T and minimal inclination angle to detector surface**

502 Two extra aspects of the problem that can still be explored analytically are related to acceptance matters, momentum thresholds and incidental angle to detector surface.

504 *II-F.i Minimal transverse momentum to reach TOF (barrel and endcap)*

For Eq. 35a to be defined, the (arcsin) function needs to be defined, *i.e.* $R_{\text{TOF}}^{\text{barrel}}/2|\rho|$ needs to be in $[-1;1]$, that means in the current situation, smaller than 1. This is obtained for $R_{\text{TOF}}^{\text{barrel}}/2 < |\rho|$. $R_{\text{TOF}}^{\text{barrel}}/2$ is a minimal radius of curvature which is necessary to touch the TOF barrel layer. Translated in terms of p_T , and using thus 22a, one gets :

$$\left(\frac{R_{\text{TOF}}^{\text{barrel}}}{2} 0.299\,792\,458 |B_Z n| = p_{T\text{min}}^{\text{barrel}} \right) < p_T \quad (42)$$

510 (Note that the above formula is a sort of bare minimum to be required for the barrel case : when $p_T \rightarrow p_{T\text{min}}^{\text{barrel}}$, the particle performs almost a half-turn in the transverse plane and approaches tangentially the surface of the barrel cylinder.)

514 Similar considerations have to be taken into account for the endcap. There exists a lower radius for the endcap ring, near the beampipe, $R_{\text{TOF,min}}^{\text{endcap}}$. Such a radius can be obtained via the alleged η_{max} acceptance of the endcap sub-detector (see II-E.ii).

$$516 \quad R_{\text{TOF,min}}^{\text{endcap}} = R(\eta_{\text{max}}^{\text{endcap}}) \quad (43)$$

$$R_{\text{TOF,min}}^{\text{endcap}} = \frac{|Z_{\text{TOF}}^{\text{endcap}}|}{\sinh(\eta_{\text{TOF,max}}^{\text{endcap}})} \quad (43a)$$

518 On the same model as Eq. 42, one can then define for the endcap a minimal p_T requested for regular particles flying towards the endcap as well as for looper particles :

$$520 \quad \left(\frac{R_{\text{TOF,min}}^{\text{endcap}}}{2} 0.299\,792\,458 |B_Z n| = p_{T\text{min}}^{\text{endcap}} \right) < p_T \quad (44)$$

Highlight II.7. *Minimum p_T threshold necessary in endcap to reach TOF plane above the inner ring radius, $R_{\text{TOF,min}}^{\text{endcap}}$.*

$$\left(\frac{|Z_{\text{TOF}}^{\text{endcap}}|}{2 \sinh(\eta_{\text{TOF,max}}^{\text{endcap}})} 0.299\,792\,458 |B_Z n| = p_{T\text{min}}^{\text{endcap}} \right) < p_T \quad (44a)$$

522 In such an endcap case, there is no specific angle of approach to be anticipated towards the vertical plane of the TOF endcap. To encounter a tangential arrival, one needs to consider an almost infinite looper, with $\eta \approx 0^+$ or 0^- but $\neq 0$.

526 In order to anticipate the future discussion regarding the various experimental configurations that will be studied later in this document, Tab. 1 lists a few examples of p_T threshold for different setups, depending on B_Z , $R_{\text{TOF}}^{\text{barrel}}$ for barrel TOF and B_Z , $\eta_{\text{TOF,max}}^{\text{endcap}}$ and $Z_{\text{TOF}}^{\text{endcap}}$ for endcap TOF.

	Configuration label	$ B_z $	sub-det.	$\langle R_{\text{TOF}}^{\text{barrel}} \rangle$	$p_{T\text{min}}^{\text{barrel}}$	
BARREL	ALICE-1 run II	0.5 T	(TOF)	3.80 m	0.285 GeV/c	
	ATLAS run IV+V	2.0 T	(hyp.)	1.00 m	0.300 GeV/c	
	ATLAS run IV+V	2.0 T	(hyp.)	0.29 m	0.087 GeV/c	
	CMS run IV	3.8 T	(BTL)	1.16 m	0.661 GeV/c	
	ALICE-3 run V	0.5 T	(hyp.)	1.00 m	0.075 GeV/c	
	ALICE-3 run V	0.5 T	(hyp.)	0.20 m	0.015 GeV/c	
	Configuration label	$ B_z $	sub-det.	$\eta_{\text{TOF,max}}^{\text{endcap}}$	$\langle Z_{\text{TOF}}^{\text{endcap}} \rangle$	$p_{T\text{min}}^{\text{endcap}}$
ENDCAP	ALICE-1 run II	0.5 T	-	\emptyset	\emptyset	-
	ATLAS run IV+V	2.0 T	(HGTD)	4.0	3.45 m	0.076 GeV/c
	ATLAS run IV+V	2.0 T	(hyp.)	2.1	1.50 m	0.112 GeV/c
	CMS run IV	3.8 T	(ETL)	3.0	3.04 m	0.345 GeV/c
	ALICE-3 run V	0.5 T	(hyp.)	4.0	2.00 m	0.011 GeV/c

Table 1: Minimal p_T thresholds based on Eq. 42 and 44a obtained for particles of electric charge $q = n.e = \pm 1.e$ Coulomb, like π^\pm . Several TOF detector configurations are considered, among the ones found or possibly expected at the (HL-)LHC. The detector cases which are conjectured here without being endorsed officially by the concerned collaboration are notified with the label (*hyp.*), the sub-detector acronym is mentioned otherwise.

530 **II-F.ii Inclination angle of the track with respect to the barrel detector surface**

532 The track will arrive onto the detector surface with a certain inclination angle. It can be anticipated that a tangential approach will not give a decent detection. To cross properly the active thickness of the detector and avoid malfunctioning of the TOF response, it is likely that
 534 a minimal angle is required in practice.

536 In the case of the TOF barrel, the angle to focus on is sketched in Fig. 10. The goal is to determine the expression of the angle δ between $\vec{p}_{\text{tot}}(t_f)$ and the local plane of the TOF barrel nearby the TOF hit. Using the notations defined in the figure, we have:

538
$$\sin(\delta) = \frac{AB}{BI} \quad (45)$$

540
$$\sin(\delta) = \frac{1}{\cosh(\eta)} \sqrt{1 - \left(\frac{R_{\text{TOF}}^{\text{barrel}}}{2\rho}\right)^2} \quad (45a)$$

542
$$\sin(\delta) = \frac{1}{\cosh(\eta)} \sqrt{1 - \left(\frac{R_{\text{TOF}}^{\text{barrel}}}{2}\right)^2 \left(\frac{0.299\,792\,458 |B_Z n|}{\|\vec{p}_T\|}\right)^2} \quad (45b)$$

δ , being then a function of η , $R_{\text{TOF}}^{\text{barrel}}$, n , B_Z and p_T

544 From Eq. 45b, we revert the logic and now express p_T as a function of (δ, η, \dots) . Doing so, we arrive to the final constraint:

Highlight II.8. Minimum p_T threshold necessary in barrel to reach TOF with a certain inclination angle δ .

$$\|\vec{p}_T\| > \left(p_{T_{\text{min}}}^{\text{barrel}}(\delta) = \underbrace{\frac{R_{\text{TOF}}^{\text{barrel}}}{2} \cdot 0.299\,792\,458 |B_Z n|}_{= p_{T_{\text{min}}}^{\text{barrel}}(\text{Eq. 42})} \underbrace{\frac{1}{\sqrt{1 - \sin^2(\delta) \cosh^2(\eta)}}}_{\stackrel{\text{not}^o}{=} (k_\delta)^{-1}} \right) \quad (46)$$

546 So, imposing a minimal angle of approach to the TOF surface implies, in the barrel, a modulation of the bare minimum case of $p_{T_{\text{min}}}^{\text{barrel}}$ (Eq. 42, *i.e.* tangential approach) by the extra factor $(k_\delta)^{-1}$. Note that, for the factor $(k_\delta)^{-1}$ to be defined, there is a preliminary condition to be met, meaning that :

$$[k_\delta^2 = 1 - \sin^2(\delta) \cosh^2(\eta)] > 0 \quad (47)$$

552 As an underlying constraint, this leads to define a maximum pseudorapidity value η_δ allowed for the particle to tackle the TOF surface with a large enough inclination angle.

554
$$|\eta| < \left(\text{arccosh} \left[\frac{1}{\sin(\delta)} \right] \stackrel{\text{not}^o}{=} \eta_\delta \right) \quad (47a)$$

556 Table 2 gives a set of example values to bear in mind for η_δ , once the inclination angle to the TOF surface is limited to a range $[\delta; \pi/2]$.

Min. δ angle	Max. η_δ
45°	0.88
30°	1.32
25°	1.51
20°	1.74
15°	2.03
10°	2.44

Table 2: Values of η_δ , the maximum allowed pseudo-rapidity value affordable to cross the TOF barrel surface with a tilt angle bigger than δ .

558 So, provided that one has $|\eta| < \eta_\delta$,

$$\text{then : } \forall \delta \in \left[0; \frac{\pi}{2}\right], k_\delta \in]0; 1]$$

560 thus : $(k_\delta)^{-1} > 1$

562 meaning that $p_{T\min}^{\text{barrel}}(\delta)$ will always be lifted to higher p_T values with respect to $p_{T\min}^{\text{barrel}}$, and that such an increase depends on η .

564 Table 3 further illustrates by how much the values of $p_{T\min}^{\text{barrel}}$ listed in Tab. 1 are raised depending on η of the particle of interest. The non-linear evolution of the factor $(k_\delta)^{-1}$ can be noted : it rises monotonously with η slowly at first but then starts to increase exponentially as η gets
566 closer to η_δ .

		$\eta (< \eta_\delta)$								
δ	η_δ	0.0	0.2	0.5	0.8	1.0	1.2	1.3	1.5	1.7
30°	1.32	1.155	1.162	1.211	1.345	1.572	2.355	5.885	∅	∅
25°	1.51	1.103	1.108	1.137	1.212	1.319	1.553	1.807	9.275	∅
20°	1.74	1.064	1.067	1.084	1.125	1.177	1.274	1.476	1.684	3.945
		$(k_\delta)^{-1}$								

Table 3: Values of $(k_\delta)^{-1}$, the extra factor that shift upwards the value of $p_{T\min}^{\text{barrel}}$ as one request a minimal incilation angle δ for the approach of the particle to the TOF barrel surface. Note that, for a retained value of δ , this in turn restricts the range allowed for $|\eta|$ to $[0; \eta_\delta]$.

II-F.iii Inclination angle of the track with respect to the endcap detector surface

568 In the case of the TOF endcap, the angle to focus on is sketched in Fig. 12. Under such
570 circumstances, the inclination angle is in fact defined from the very beginning, by the initial conditions. The inclination angle with respect to the TOF vertical plane corresponds directly to λ , the angle between \vec{p}_{tot} and \vec{p}_T ⁴. Using the notations defined in the figure, we have:

$$572 \quad \tan(\lambda) = \frac{\|\vec{p}_Z\|}{\|\vec{p}_T\|} = \frac{\|\vec{p}_T\| \sinh(\eta)}{\|\vec{p}_T\|} \quad (48)$$

$$\tan(\lambda) = \sinh(\eta) \quad (48a)$$

⁴ Note that such an angle is the $\pi/2$ complement to θ , the angle usually bound to the pseudo-rapidity definition, the angle between \vec{p}_Z and \vec{p}_{tot} .

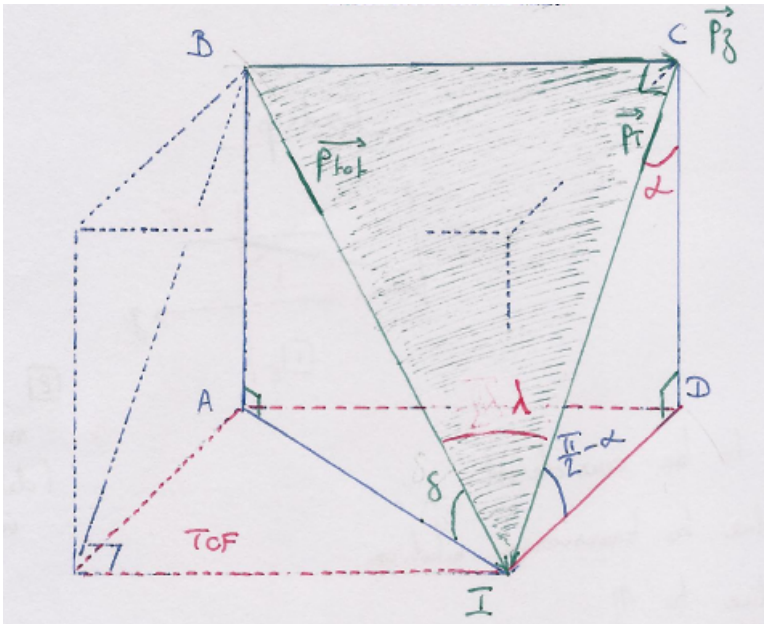


Fig. 10: Sketch of the various angles at stakes when considering the inclination angle of the trajectory to the detector surface of the TOF barrel. The angle that is necessary to be assessed is the angle δ in the figure, to be related to $\alpha(t_f)$, the transverse rotation and/or λ , the inclination angle between \vec{p}_{tot} and \vec{p}_T .

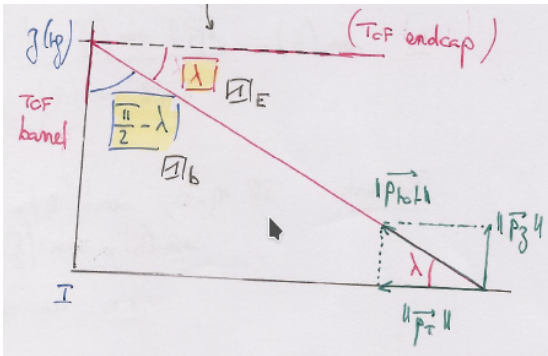


Fig. 11: Sketch of the unfolded helix of the trajectory, letting appearing the angle λ , the inclination angle between \vec{p}_{tot} and \vec{p}_T .

The horizontal axis is the flattened length of the transverse projection to the B field [arc circle onto $(O; \vec{e}_x, \vec{e}_y)$]; the vertical axis stands for the $z(t_f)$ component along \vec{e}_z .

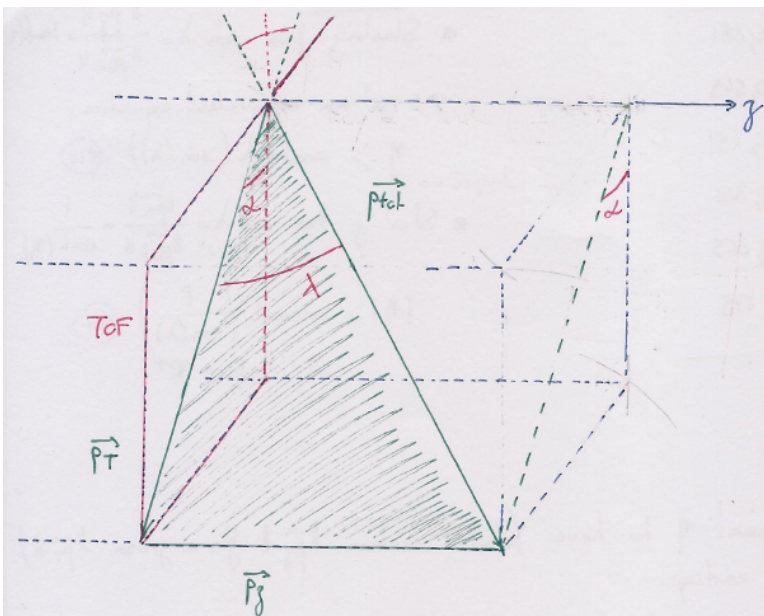


Fig. 12: Sketch of the various angles at stakes when considering the inclination angle of the trajectory to the detector surface of the TOF endcap. The angle that is necessary to be assessed is simply λ , the inclination angle between \vec{p}_{tot} and \vec{p}_T .

574 Meaning that if we want to set a minimal value for λ , one needs to require :

$$\tan(\lambda) > \tan(\lambda_{\min}) \quad (49)$$

576 giving :

Highlight II.9. *Minimum η threshold, η_{\min}^{λ} , necessary to reach the TOF endcap plane under a certain inclination angle λ .*

$$\eta > \left(\operatorname{arcsinh}[\tan(\lambda_{\min})] \stackrel{\text{not } \circ}{=} \eta_{\min}^{\lambda} \right) \quad (49a)$$

578 There is a minimal pseudorapidity value to satisfy in order to reach the TOF end-plane un-
 580 der a sizeable angle. This is clearly not an issue *a priori* for particles expected directly in
 the endcap, because the incidental angle is large anyhow and converging towards $\pi/2$ with
 582 increasing η . For instance, for $\eta = +1.5$, $\lambda = 64.8^\circ$; for $\eta = +4.0$, $\lambda = 87.9^\circ$ (using Eq. 48a,
 $\lambda = \arctan[\sinh(\eta)]$). However, Eq. 49a has to be borne in mind for low- p_T looper particles :
 584 tracks that do not reach the TOF barrel will not necessarily be properly detected in the endcap,
 even if they manage to survive and actually reach the vertical instrumented plane.

Table 4 gives a glimpse of what can be the actual minimum η_{\min}^{λ} induced by an explicit re-
 586 quirement on the authorised range for the tilt angle to endcap $[\lambda_{\min}; \pi/2]$.

λ_{\min} angle	η_{\min}^{λ}
45°	0.881
30°	0.549
25°	0.451
20°	0.356
15°	0.265
10°	0.175

Table 4: Values of η_{\min}^{λ} taken for various minimal angles requested when a particle is about to hit the TOF endcap plane.

588 III TOF separation power

III-A General intent and different configurations

590 The goal is to determine the ability of TOF detectors, present or foreseen at the (HL-)LHC, to
 discriminate between particle species in terms of $n\sigma_{\text{TOF}}$ (Eq. 5a p.6), based on the analytical
 592 formulae derived in earlier sections. Such a separation power will be derived as 2D maps in
 phase space (p_T, y).

594 The code performing such an assessment of the TOF separation power under various experi-
 mental configurations is written in C++ within the ROOT framework. A code snippet is pro-
 596 vided as an appendix (see App. A); it gives the core of the code, computing the actual times of
 flight along p_T and y . The complete source code is further publicly released under github.com
 598 under the project name *TOFseparationPowerAsFuncPtY* [9].

III-B Typical layout of the figures to come

600 In Figure 13, the content of the figures to come is detailed, this allows us to settle the type of in-
 602 formation to expect. For a given experimental TOF setup (B_Z , σ_{TOF} , R_{TOF} , Z_{TOF}), corresponding
 typically to one of the LHC experiment configurations, (ALICE-1, ALICE-3, ATLAS, CMS),
 604 8 sub-figures forecast the formula-based separation among identified species : e^\pm , μ^\pm , π^\pm ,
 K^\pm , p^\pm , d^\pm , t^\pm , ${}^3\text{He}^{2\pm}$, ${}^4\text{He}^{2\pm}$. The separation power is addressed with 2-by-2 strategy among
 606 “neighbouring” species, *i.e.* one given species and the closest particle(s) in mass at lower and/or
 higher m_0 in the previous list.

608

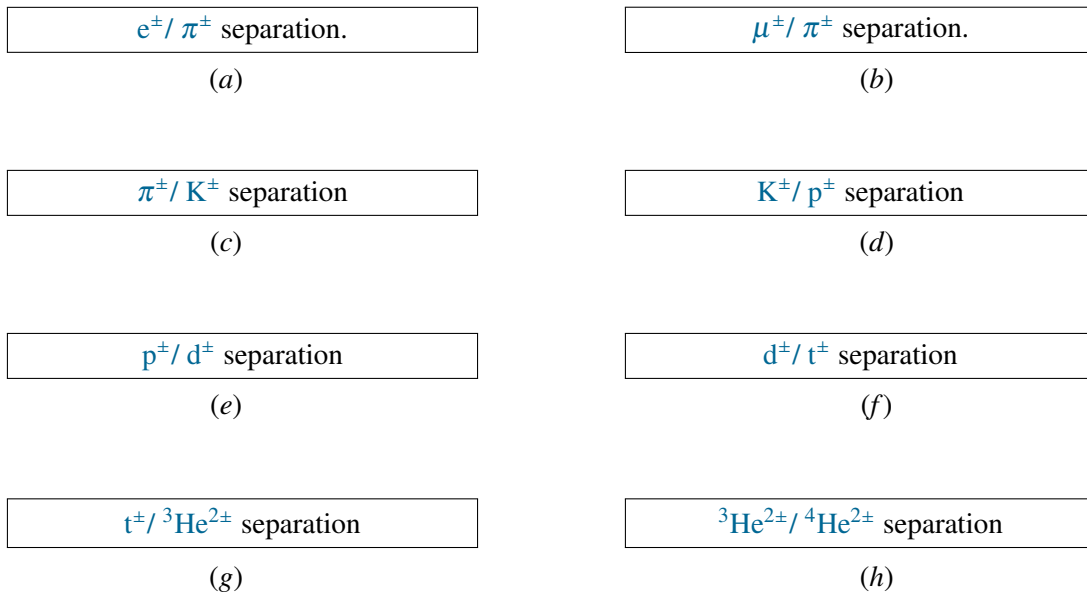


Fig. 13: Template layout of the typical sub-figures to be shown for each configuration tested per experiment, based on the set of working hypotheses drawn : detector timing resolution (σ_{TOF}), magnetic solenoidal field (B_Z), radial position of central barrel TOF (R_{TOF}), longitudinal position of the endcap TOF (Z_{TOF}) and the respective η coverages in barrel and endcap.

IV Using ALICE-1 in LHC runs I and II as a benchmark exercise

610 At the LHC, there is already an operational TOF detector in a central rapidity region, the one
 from the ALICE experiment. It is a sub-detector based on Multi-Resistive Plate Chamber
 612 (MRPC), located at $\langle R_{\text{TOF}} \rangle = 3.80$ m, covering up to $|\eta| = 0.88$, and it is a sub-detector for
 which real performances are already known, measured and monitored. In the following, we
 614 focus on the ALICE-1 configuration⁵, *i.e.* the setup running during LHC runs I (2009-2013)
 and II (2015-2018). Such a concrete example can be used to assess the realm of the proposed
 616 exercise : by letting the reader know to what extent the analytical formulae at use here do match
 the performances met under real conditions, one can better grasp the limits of the forecast
 618 provided in later sections; there, the point will be to provide analytically-derived projections
 for future detector configurations at the LHC that are currently developed or simply considered
 620 (...) but in any case not yet installed and operated.

⁵ The same detector will still be in place in ALICE-2, after the LHC Long Shutdown 2 [2019-2021], for the LHC runs III and IV (≥ 2022).

Fig. 15: Expected TOF performances in terms of particle separations as a function of p_T and y for the configuration already foreseen or possibly anticipated for the [ALICE-1](#) experiment, with hypotheses :
 i) $\langle r_{TOF}^{barrel} \rangle = 3.80$ m, ii) $\langle z_{TOF}^{endcap} \rangle = -$ m, iii) TOF timing resolution = 56 ps, iv) $B_{field} = -0.5$ T.

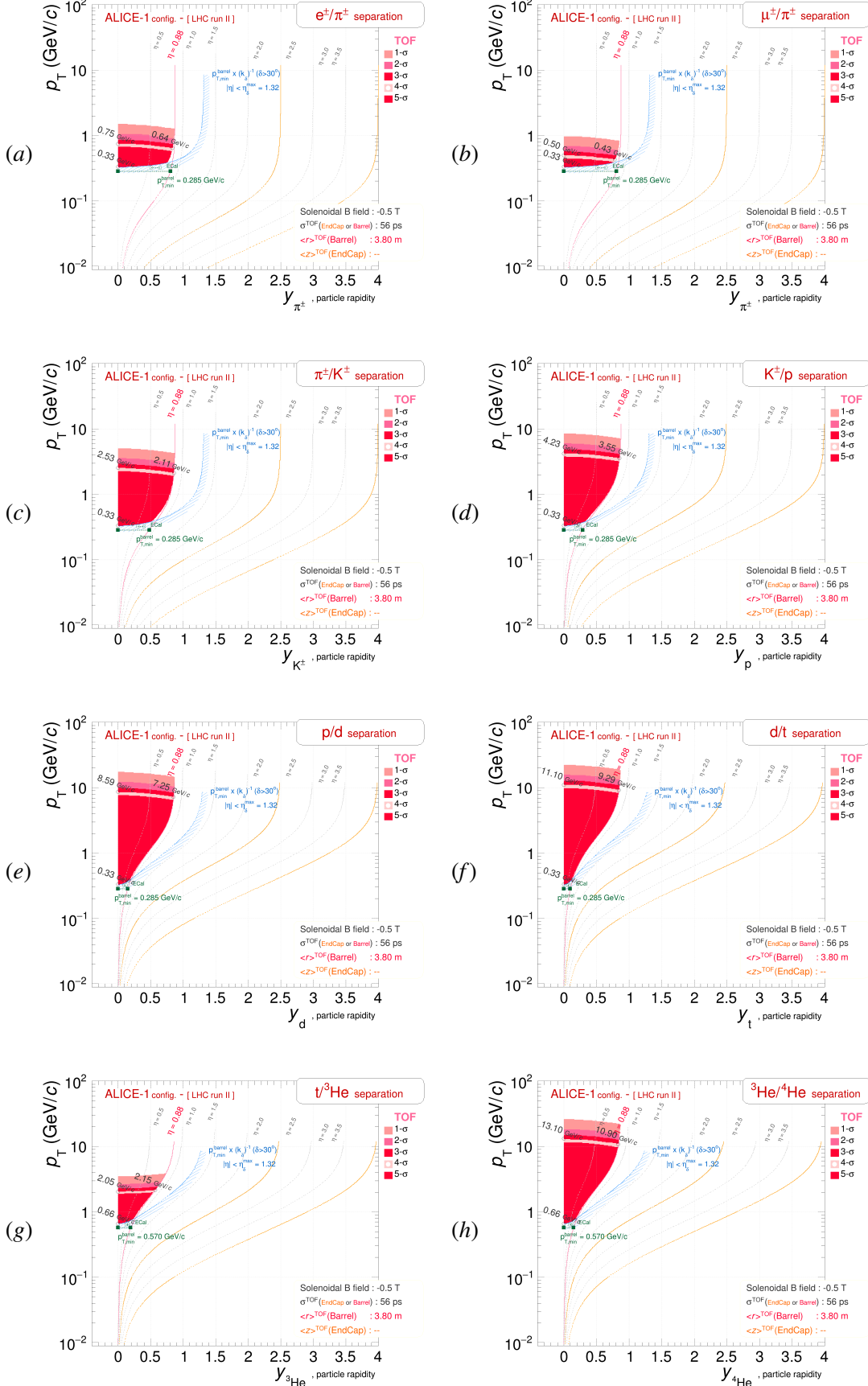
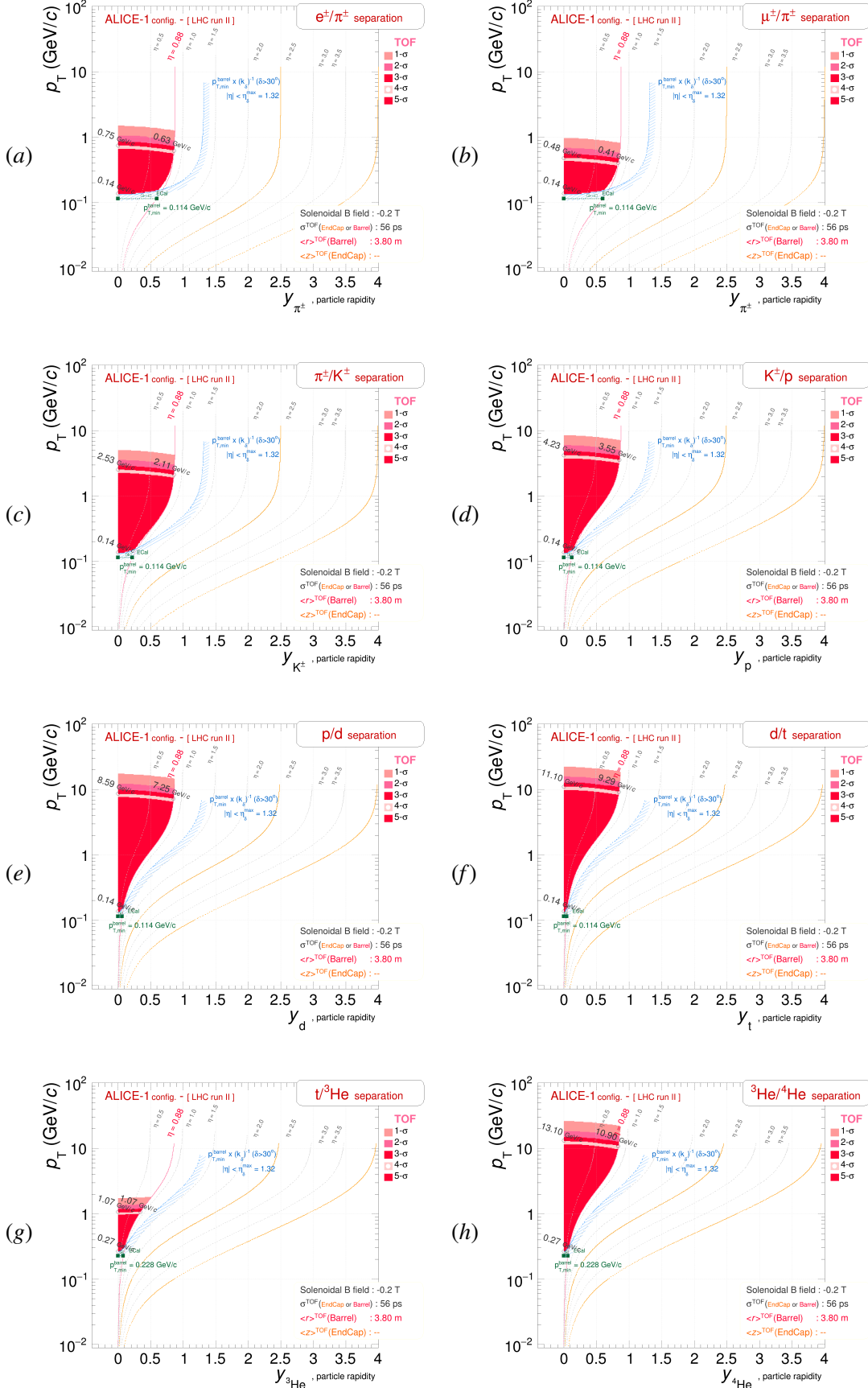


Fig. 16: Expected TOF performances in terms of particle separations as a function of p_T and y for the configuration already foreseen or possibly anticipated for the [ALICE-1](#) experiment, with hypotheses :

- i) $\langle r_{TOF}^{barrel} \rangle = 3.80$ m, ii) $\langle z_{TOF}^{endcap} \rangle = _$ m, iii) TOF timing resolution = 56 ps, iv) $B_{field} = -0.2$ T.



IV-A Analytical-formula-based performances of the ALICE-1 TOF

622 To that end, three sets of figures, making use of the aforementioned code and formulae, have
623 been derived in the ALICE-1 case, corresponding to :

624 *Figure 14* : ALICE run I configuration, with timing resolution set to 80 ps, with a L3 solenoidal
625 field of 0.5 T, valid in Pb–Pb or pp,

626 *Figure 15* : ALICE run II configuration, with improved timing resolution of the order of 56 ps,
627 with a L3 solenoidal field of 0.5 T, achieved in run II Pb–Pb at least,

628 *Figure 16* : ALICE run II “low field” configuration, with timing resolution of the order of
629 56 ps, with a L3 solenoidal field of 0.2 T, achieved in run II Pb–Pb and Xe–Xe at least.

630 IV-B Measured performances of the ALICE-1 TOF sub-detector

631 The previous figures have to be compared with the concrete performances of the TOF detector
632 in real conditions.

633 For ALICE TOF in Run I, generic performances can be found in the reference [10] and in the
634 dedicated section 7.3 in the publication about the ALICE Run-I general performances [11]. For
635 the same detector in Run II, the improved performances (in Pb–Pb notably) are summarised in
636 the proceedings [12].

637 To illustrate the detector achievements, several ALICE figures are brought to the reader’s at-
638 tention in the following.

639 *Figure 17* : the figure illustrates the β distributions a function of total momentum p . The
640 individual sub-figures are obtained with LHC run II data, for 4 different collision systems
641 (pp, p–Pb, Xe–Xe, Pb–Pb) at TeV-scale collisions energies and for 2 magnetic field
642 configurations of the L3 solenoid (0.5 T and 0.2 T). There on any graph, several bands
643 densely populated with counts emerge : e^\pm appear at very low momenta at $\beta_{\text{tot}} \approx 1$,
644 followed with clear contrasted bands of π^\pm , K^\pm , p^\pm and to a lesser extent, d^\pm .

645 *Figure 18* : TPC-TOF matching efficiency (here in A–A) *i.e.* ability of matching a track pro-
646 longation from TPC as detector placed at lower radius for (a) charged particles h^\pm in B
647 = 0.5 T and (b) positively-charged identified hadrons in $B = 0.2$ T.

648 *Figure 19 and Figure 20* : the summary plots indicate the mid-rapidity separation power in
649 terms of $n \cdot \sigma_{PID}$ for 3 stable hadrons (π^\pm/K^\pm and K^\pm/p^\pm). (Note especially in the lower
650 panels the p_T range covered by the ALICE TOF for a $> 2 \cdot \sigma_{PID}$ separation). The first
651 set of graphs is taken from [11] (Fig. 46) and is obtained considering Pb–Pb detector
652 conditions in LHC run I. The second one from [13] (Fig. 1), for Pb–Pb and pp detector
653 conditions in LHC run II.

654 *Figure 21* : Resolution on the event starting time, t_0 , assessed with the TOF itself (a) for low
655 TOF-hit multiplicities (pp, p–Pb, peripheral A–A) and (b) for high TOF-hit multiplicities
656 (A–A).

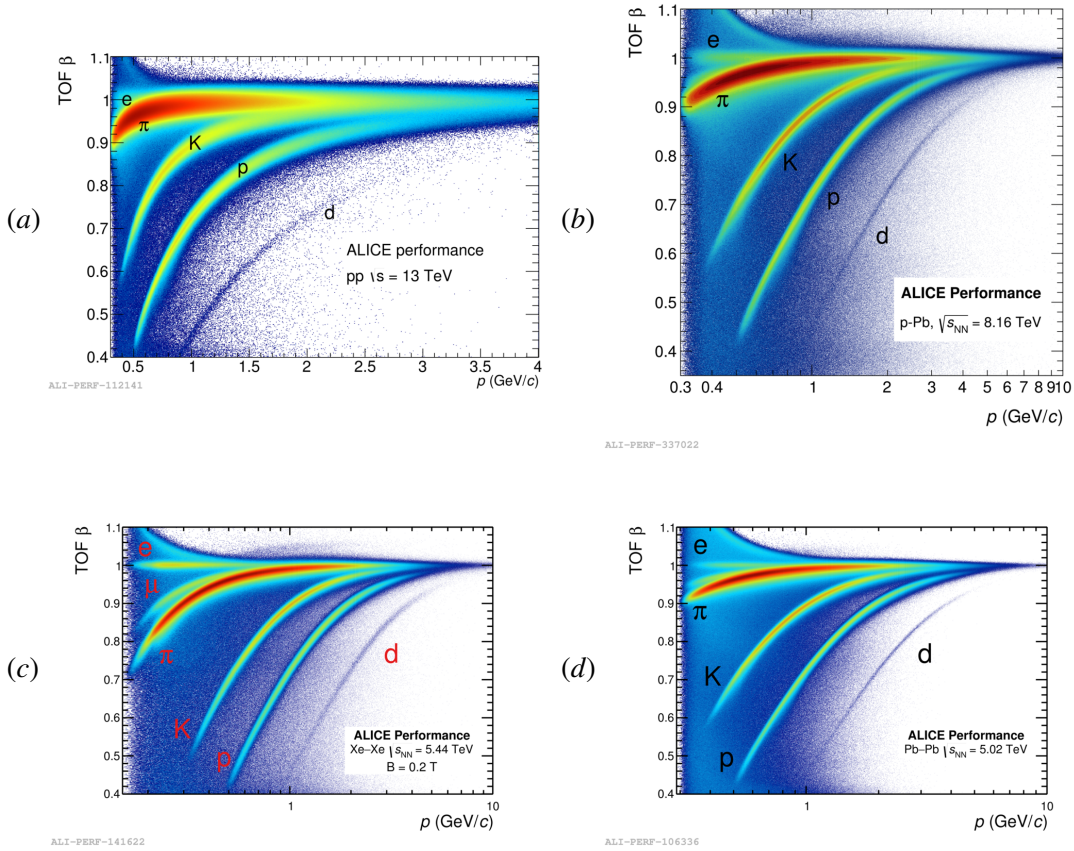


Fig. 17: Measured β distributions as a function of total momentum p , obtained with the ALICE TOF detector in data recorded in run II for various collision systems :

(a) pp , $\sqrt{s} = 13$ TeV [$B = 0.5$ T], (b) $p\text{-Pb}$, $\sqrt{s_{NN}} = 8.16$ TeV [$B = 0.5$ T] and

(c) Xe-Xe , $\sqrt{s_{NN}} = 5.44$ TeV [$B = 0.2$ T], (d) Pb-Pb , $\sqrt{s_{NN}} = 5.02$ TeV [$B = 0.5$ T].

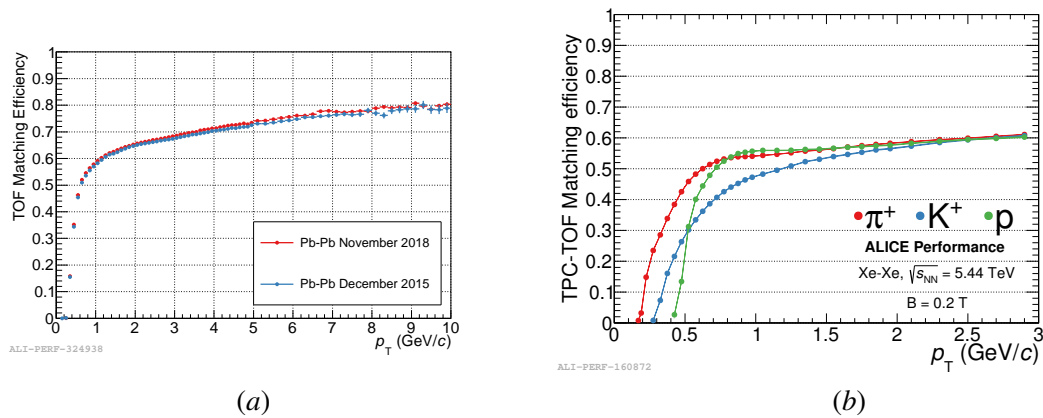


Fig. 18: Efficiency in TPC-TOF track matching (here for A–A) in ALICE-1, *i.e.* ability of matching a track prolongation out of TPC towards TOF, the TPC being the detector placed at lower radius for (a) charged particles h^\pm in $B = 0.5$ T and (b) positively-charged identified particles in $B = 0.2$ T.

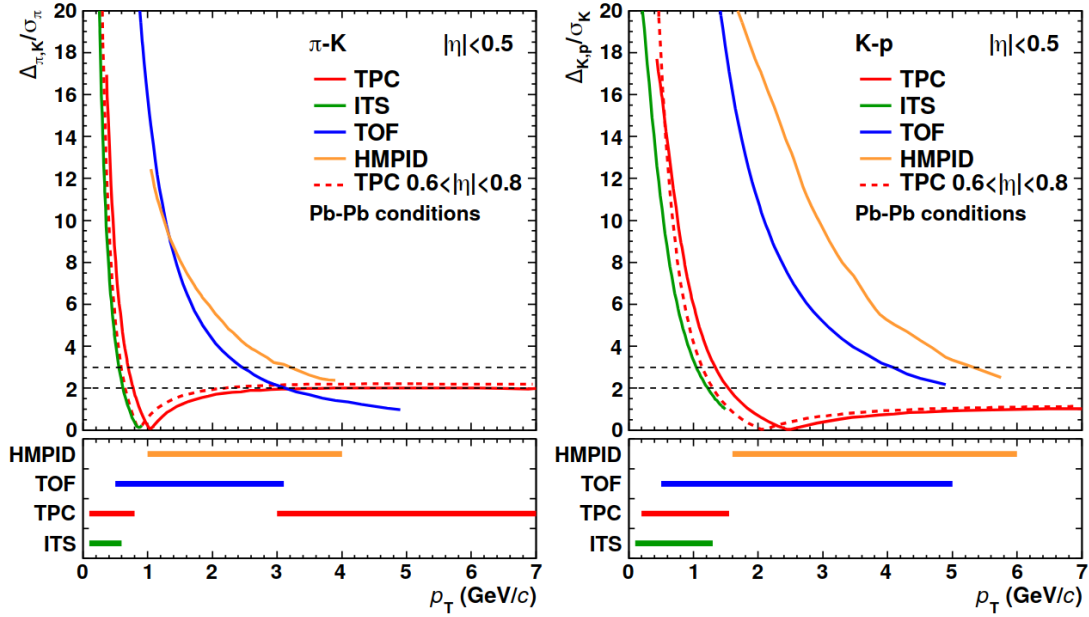


Fig. 19: Separation power for particle identification averaged over $|\eta| < 0.5$ for π^\pm/K^\pm and K^\pm/p^\pm with the dedicated ALICE sub-detectors under run-I conditions for Pb-Pb with the collision energy $\sqrt{s_{NN}} = 2.76$ TeV. The lower panels represent the range over which the different sub-detectors have a separation power of more than 2σ (Fig. 46 in [11]).

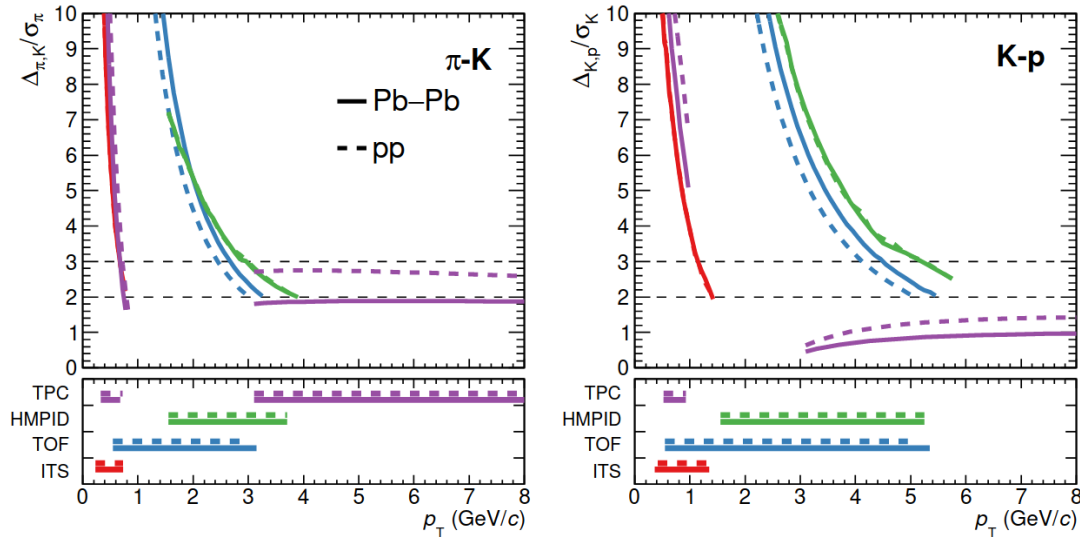


Fig. 20: Separation power for particle identification averaged over $|\eta| < 0.5$ for π^\pm/K^\pm and K^\pm/p^\pm with the dedicated ALICE sub-detectors under run-II conditions for pp and Pb-Pb with $\sqrt{s_{NN}} = 5.02$ TeV. The lower panels represent the range over which the different sub-detectors have a separation power of more than 2σ (Fig. 1 in [13]).

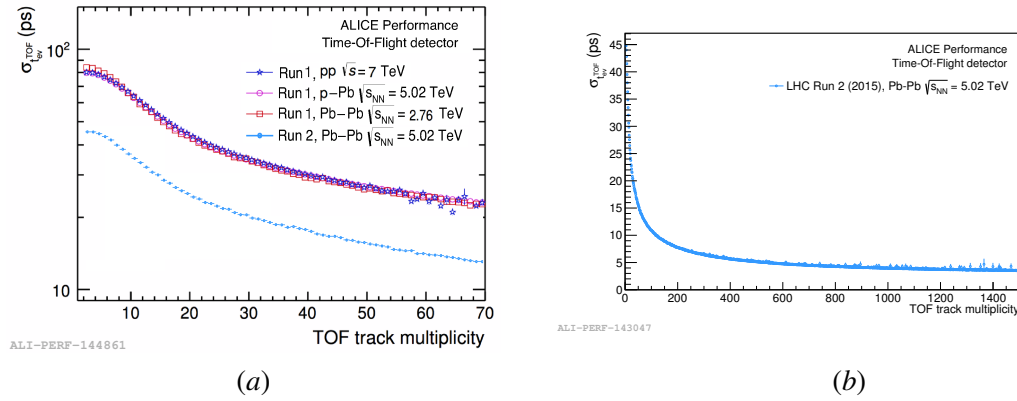


Fig. 21: Resolution on the event starting time, t_0 , determined with the TOF sub-detector itself (a) for low TOF-hit multiplicities (pp, p-Pb, peripheral A-A), updated by the ALICE collaboration from [14] and (b) for high TOF-hit multiplicities (A-A).

IV-C Comparing and discussing analytics and real performances

Such figures call for dedicated comments, that would pinpoint several specific aspects of the confrontation between analytical formulae and real performances.

IV-C.i Acceptance \times efficiency to reach TOF

As pointed by Tab. 1, the $p_{T\min}^{\text{barrel}}$ of mid-rapidity acceptance in case of ALICE-1 is on paper equal to 0.285 GeV/c. With a tangential approach to the TOF layer, tracks with this p_T are essentially at the edge of the tracking efficiency ($\mathcal{A} \cdot \varepsilon \mathcal{O}(1\%)$), illustrated by Fig. 18 (b). It stands for the bare minimum minimum, that is moreover usually achieved with π^\pm only. With such a value of p_T , one is not yet in a sort of comfort zone around a desirable functioning point ($\mathcal{A} \cdot \varepsilon \gtrsim 50\%$).

Still in the same figure, the reader may notice, for π^\pm , K^\pm and p^\pm cases, that the tracking of a particle up to the TOF sub-detector is a particle-species dependent feature, that, in addition, changes from one experiment to the next. For a given experiment, $\mathcal{A} \cdot \varepsilon$ becomes independent of the particle species only above a certain momentum; for instance, here in ALICE-1, p_T has to be above 2.5 GeV/c.

IV-C.ii Validation with the measured separation among (π^\pm , K^\pm , p^\pm) species

Figures 19 and 20 give a summary of the separation among the most abundantly produced hadrons. The separation is derived from concrete analyses of primary-like particles and concerns inclusive production of identified particles. The p_T ranges accessible with the help of TOF are further summarised for different LHC runs, systems and collision energies in Tab. 5. Note that the measurements are :

- (i) all performed under a field $|B_Z| = 0.5$ T,
- (ii) averaged over a certain extent in $|\eta| (< 0.5)$,
- (iii) dependent on the signal extraction methods that can subtly differ from one analysis to the next, improving as experience grows.

Considering the values listed in the table, it should be noted that the lower identification threshold values as well as the upper cut-off values are not universal but vary a little with LHC periods, collision systems, $\sqrt{s_{NN}}$ and thus, with running conditions and detector stress. All in all, comparing the table values to $4\text{-}\sigma_{\text{TOF}}$ and, more especially, to $3\text{-}\sigma_{\text{TOF}}$ of the “analytical” figures

LHC run	System	$\sqrt{s_{NN}}$	p_T range of measurements (GeV/c)			Ref.
			π^\pm	K^\pm	p^\pm	
run I	Pb–Pb	2.76 TeV	0.50-3.00	0.45-3.00	0.50-4.60	[15]
run I	pp	7.00 TeV	0.50-2.50	0.50-2.40	0.80-4.00	[16]
run II	Pb–Pb	5.02 TeV	0.50-3.50	0.60-3.50	0.80-4.50	[13]
run II	pp	5.02 TeV	0.50-3.50	0.65-3.50	0.80-4.50	[13]
run II	pp	13.00 TeV	0.70-4.00	0.60-3.00	0.90-4.00	[17]

Table 5: ALICE-1 TOF measurements of identified hadrons, π^\pm , K^\pm , p^\pm , in several analyses of LHC run-I and -II data.

(Figs. 14 and 15, sub-figures (c) and (d) related to π^\pm - K^\pm and K^\pm - p^\pm separations), one can state that :

- (1) the lower threshold is, in the analytic projections, always 0.33 GeV/c, independently of the species. Such a value is never met in real data, the TOF measurements systematically start at higher values, $\approx +0.2$ GeV/c being at least necessary for charged pions, rather +0.3 GeV/c required for charged kaons, and up to +0.5 GeV/c for protons.
- (2) the upper momentum bounds of separation are, for each particle species, in a similar ballpark (*i.e.* within 0.5 GeV/c, as is the spread among the various data analyses), showing a convergence of the analytic computation with measured performances. In turn, it reveals that, on the high momentum front, the location of the TOF layer R_{TOF}^{barrel} and its intrinsic time resolution σ_{TOF} become the two key parameters driving the TOF performances.

IV-C.iii Impact of multiplicity on the overall TOF performance, the start time

As detailed in [14] and mentioned in [12], the intrinsic resolution of the TOF sub-detector, which has been considered up to here, σ_{TOF} , is not the only component entering the final timing resolution at stakes for particle identification. The total timing resolution σ_{timing}^{tot} depends on :

$$(\sigma_{timing}^{tot})^2 = \sigma_{TOF}^2 + \sigma_{tracking}^2 + \sigma_{evt-t_0}^2 \quad (50)$$

- anything related to the assessment of actual length \mathcal{L} of the track can be wrapped in the uncertainty associated to tracking, $\sigma_{tracking}$
- The event timing, t_0 , can have a substantial impact on the total timing uncertainty. In ALICE-1, the event collision time can be provided, in a self-consistent way, by the TOF sub-detector itself and/or by another sub-detector T0. In both options, the quality of the information is weighed event-by-event based on the corresponding charged particle acceptance : on the one hand, the ALICE-1 TOF is covering $\approx 2 \times 0.88$ units of pseudo-rapidity, but is 3.80 m away from the interaction point, on the other hand, T0 is a two-side set of Cerenkov counters (T0A and T0C) at forward and backward rapidities, one being rather far away from the interaction point ($z_{T0A} = +374$ cm), the other rather close ($z_{T0C} = -70$ cm), but in both sides with a rather limited η coverage, ($+4.61 \leq \eta_{T0A} \leq +4.92$) and ($-3.28 \leq \eta_{T0C} \leq -2.97$). Focussing on the sole TOF detector and the standalone timing strategy, one can gauge (Fig. 21) the accuracy of the TOF-based σ_{evt-t_0} as a function of the TOF hit multiplicity While the contribution in semi-central and central Pb–Pb is contained with respect to σ_{TOF} [$\sigma_{evt-t_0} < 5 - 10$ ps, sub-Fig. (b)], the situation at low multiplicity [pp, p–Pb and peripheral Pb–Pb in sub-Fig. (a)] indicates an effect that is of the same order as σ_{TOF} : for a multiplicity below 30 charged particles reaching the TOF layers, σ_{evt-t_0} varies between [30;90] ps. Such an extra uncertainty can only degrade in a

sizeable manner the timing accuracy of the measurements via a larger $\sigma_{\text{timing}}^{\text{tot}}$, thus reducing
 reluctantly the upper p_T reach of any TOF measurement. In details, if it is certainly well-founded
 that such an uncertainty can be essentially neglected for the most of A–A cross-section, it will
 be on the contrary unavoidable for small systems like pp or p–Pb Minimum Bias.

IV-C.iv *Light nuclei, illustration with the deuteron identification*

In Fig. 17, the reader can guess there the appearance of the deuteron band, typically above
 1 GeV/c, for any collision system presented here (pp, p–Pb, Xe–Xe and Pb–Pb). That effective
 threshold value looks substantially larger than the value $p_{\text{Tmin}}^{\text{barrel}} = 0.285$ GeV/c, the value hold-
 ing a priori for any $\pm 1e$ charged particle, as pointed by Tab. 1. What can be noticed here on the
 graph is in line with various ALICE publications, where the TOF parts of the deuteron mea-
 surements indeed starts only for p_T above 1 GeV/c in pp ([18], [19] and [20]), and 1.4 GeV/c
 in Pb–Pb [21].

The reason for this is that the propagation of a light nucleus up to the TOF layers may encounter
 various issues.

First, the path itself to TOF detector is modified by the increased probability of interactions
 with detector material (tracking layers and their services), meaning that, compared to lower-
 mass/lower-charge particles, the nucleus itself can be more easily lost on the way to TOF.

Secondly, even if the heavy particle manages to hit the TOF layer, the nucleus signal can be
 drowned by the existing background. The contaminants located within the same expected zone
 in $(\beta_{\text{tot}}, p_{\text{tot}})$ phase space can be made of any species : stable hadrons such as π^\pm , K^\pm or p^\pm , as
 well as light nuclei, deuteron themselves (!) and other light nuclei.

Such a signal pollution can be due to :

- (1) TOF hit mismatches where the tracking fails, among the combinatorics of hits, to con-
 nect TOF to tracking sub-detectors of lower radii (TPC and/or, TRD in the ALICE-1
 case);
- (2) secondary particles emitted within the experimental volume, as secondary products
 from weak decays or as genuine products of inelastic interactions with detector materi-
 al⁶. For a fixed momentum, secondaries will have in turn a shorter \mathcal{L} and duration
 of flight, thus luring the TOF detector with wrong time assignment.
- (3) the tails of the $(\beta_{\text{tot}}, p_{\text{tot}})$ distributions of other “regular” primary particles.

The background problem is essentially a question of relative frequency of occurrence be-
 tween the background cases and the natural production rate of the light nucleus of inter-
 est in the given momentum range. The production of primary deuteron, for instance, is a
 rather rare process ($dN(d^\pm)/dy|_{y \approx 0} \approx 2 - 4 \cdot 10^{-4}$ in pp [18]), such a signal can easily be over-
 whelmed by the misidentification or ill-identification, admittedly rare, of particles that are far
 more copiously produced like π^\pm , K^\pm or p^\pm (e.g. at $y \approx 0$, in pp [16], the integrated yields
 $dN(\pi^\pm)/dy \approx 18 dN(p^\pm)/dy$, $dN(K^\pm)/dy \approx 2.3 dN(p^\pm)/dy$ and $dN(p^\pm)/dy = 0.25$).

For low-momentum nuclei below 1 GeV/c, in the ALICE-1 case, it is in fact the unique ca-
 pabilities of lineic energy loss dE/dx in the TPC that allow clean identification (up to 159
 dE/dx sampling). The case will have to be carefully considered in the future LHC configu-
 ration where no TPC is foreseen and, if dE/dx measurements may exist, they will be limited
 along each track to a few hits ($\mathcal{O}(5)$) in the silicon layers instrumented with analogous readout
 (typically micro-strips).

⁶ Considering knock-out nuclei, such a phenomenon is essentially absent for anti-nucleus production but is
 important for nucleus one at low momenta, e.g. , in pp 7 TeV or 13 TeV, knock-out deuterons typically stand for
 40% of the raw deuteron signal at $p_T = 0.6$ GeV/c and decreases exponentially with momentum, down to less than
 5% above 1.4 GeV/c [19, 20].

At the other side of the momentum spectrum, towards high p_{tot} , the TOF identification proves to be very efficient and clean. The slow motion of the *heavy* objects that the *light* nuclei are at last ($m_0 \approx A.m(\text{p}) > 2.m(\text{p}) \approx 1.87 \text{ GeV}/c^2$) allows for an extended momentum reach at high momentum : for a given p_{tot} , the light nuclei will have a clearly separated and lower β_{tot} compared to primary stable hadrons like π^\pm , K^\pm or p^\pm .

In Fig. 14(e) (80-ps), the maximum p_T possible for deuteron identification is anticipated to be between 7.17 GeV/c ($\eta=0$) and 6.05 GeV/c ($\eta=0.88$) for a $4\text{-}\sigma_{\text{TOF}}$ separation, it slightly overshoot the casual upper bound met in the measurements with the corresponding ALICE-1 set-up : 6 GeV/c achieved recently in a Pb–Pb analysis (Fig. 2 in [21]). However, in pp, the situation is dimmed, with an upper limit reduced typically to 3 GeV/c [18, 19] or 3.8 GeV/c [20]. – Why is that ? The impact of the start time resolution $\sigma_{\text{evt}-t_0}$ (see previous sub-section IV-C.iii) clearly becomes relevant but cannot explain solely the situation : with a time resolution increasing from 80 ps to 120 ps, the analytical formulae developed here predicts a reduction of the p_T reach further down, but only to 5.83 GeV/c ($\eta=0$) and 4.91 GeV/c ($\eta=0.88$) for a $4\text{-}\sigma_{\text{TOF}}$ separation. Very likely, the concrete situation is also a consequence of the impact of contaminants in view of the natural production rate of deuteron. At such p_T above 3 GeV/c, despite the already high integrated luminosities recorded with Minimum Bias triggers⁷, the deuteron production is certainly still scarce, a penalty factor being in place in small systems compared to Pb–Pb.

For nuclei, it should be finally noted that using time-of-flight measurements as identification strategy comes with one clear drawback, that is, the separation among nuclei with the same mass number A . Time-of-flight principles make it indeed difficult to distinguish between species very close in m_0 . This is especially the case for $A=3$, between t and ^3He . There essentially, the TOF difference can only be an indirect consequence of the curvature due to different electric charges : the helium nucleus will travel at very similar β_{tot} as triton, but due to $Z(\text{t})=1$ and $Z(^3\text{He})=2$, the helium will fly on a trajectory that is more curved [$\rho(^3\text{He})$, half of $\rho(\text{t})$] and so, of longer path length for a same [$p_T(t_0), \eta(t_0)$]. Beyond the separation of primary t and ^3He , such light nuclei enter frequently the decay chain of hypernuclei. For instance, ^3He plays a pivotal role in the reconstruction of a hypernucleus like hypertriton $^3_\Lambda\text{H}$ ($^3_\Lambda\text{H}^+ \rightarrow ^3\text{He}^{2+} \pi^-$ with B.R. $\approx 25\%$) [22, 23]; a blunted separation power among t and ^3He can clearly endanger the hyperphysics case in practice.

⁷ 950.10^{-6} MB pp events have been recorded from years 2016 and 2017 for [20], corresponding to about 12 pb^{-1} of integrated luminosity for inelastic pp cross-section.

794 V Synopsis of the figures and corresponding TOF configurations tested

796 In the following, several TOF configurations for LHC detectors will be exercised as announced
 798 earlier. Each exercise takes into account most of the problem aspects that have been pointed
 out and discussed in previous sections. The list of what has been retained or left aside is given
 in the overview Tab. 6.

800 The table 7 further gives the complete list of the experimental configurations tested in view of
 TOF performances, together with key parameters that make the differences from one configu-
 802 ration to the next.

804 To smooth the peregrinations of the reader through the various figures still to come (about 31
 experimental configurations \times 8 two-by-two TOF separations = 248 sub-figures), two figures
 806 have been isolated and annotated. This is meant to explicit the generic comments applicable
 to any of the results and, this way, to provide a reading template in order to tackle each figure
 808 with key items in mind. Both figures give the outcome of the K^\pm/p^\pm separation in a CMS-like
 TOF configuration with a standard (-3.8 T) magnetic field, having barrel (red and pink shades)
 810 and endcap (orange and ochre shades) 2D maps based upon the timing resolution of 30 ps
 anticipated for HL-LHC run IV. The $|\eta|$ acceptance in barrel is set to ± 1.50 and the range for
 812 endcap is defined between [1.60; 3.00].

Figure 22 is an illustration based on major hypotheses that are mostly artificial, *i.e.* in order to
 814 let the reader become aware of the manifold corners of potential phase space, the figure has
 been derived with :

- 816 (i) very loose requests on the inclination angles to barrel and endcap surfaces, $\delta > 10^\circ$
 and $\lambda > 5^\circ$ respectively;
- 818 (ii) the assumption that any detector layer remains sensitive while fully permeable as
 820 well to charged particles. In particular, the map is obtained with the idea that elec-
 tromagnetic calorimeter in the barrel (ECal), usually present next to the last tracking/
 822 TOF layer, neither stop nor disturb the particles but simply let them pass, unaltered,
 beyond the calorimeter lower radius.

824 Figure 23 corresponds to a more realistic case, where both δ and λ must exceed 30° and where
 the barrel ECal location signs definitively the end of any track hitting it; even at the beginning of
 826 its $\mathcal{A} \cdot \mathcal{E}$, the material budget (radiation length and nuclear interaction length) of the calorimeter
 is enough to destroy the ideal trajectory and the set of hypotheses discussed so far in the current
 828 study.

Labels P_b and P_e : due to the curvature of trajectory implied by the magnetic field, any par-
 830 ticle must have a minimal p_T to be able to touch the detector surface (the curvature radius
 needs to be large enough), and this is required for both barrel and endcap TOF ($p_{T\min}^{\text{barrel}}$
 832 from Eq. 42, $p_{T\min}^{\text{endcap}}$ from Eq. 44a). Such values just depend on the magnetic field B_Z
 and the electric charge q and is not dependent on m_0 , *i.e.* the numerical p_T values are
 834 shared among species of same charge.

Labels A_e^+ , A_e^- and A_b^- : the zenithal angle acceptance of a given detector is not an area
 836 that can be framed regularly by fixed edges given in η . In other words, in both figures,
 the pink solid line at 1.50 does not limit properly the barrel acceptance, the two orange
 838 solid lines at η at 1.60 and 3.00 do not circumscribe correctly the endcap acceptance.

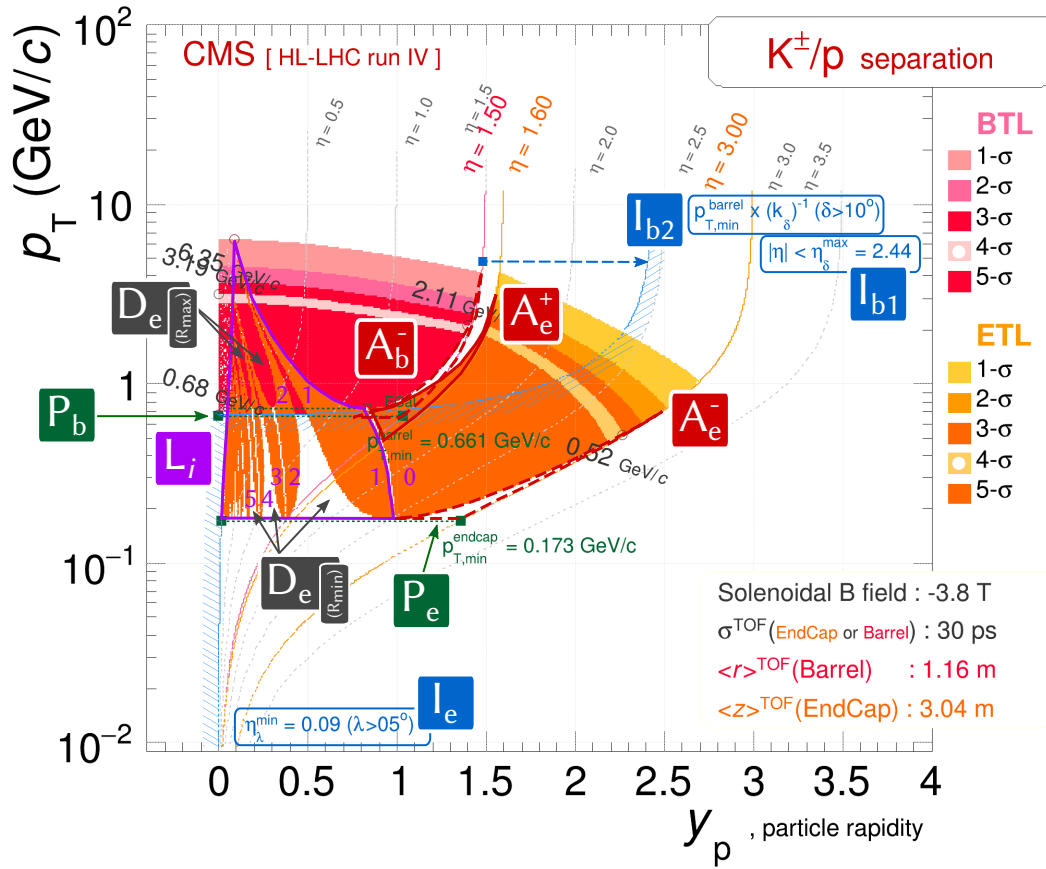


Fig. 22: Typical figure content with key elements highlighted, illustrated here with the K^\pm/p^\pm TOF separation in a CMS-like case. In the present illustration, the requested constraints on the inclination angles in barrel (δ) and endcap (λ) are relaxed, to 10° and 5° respectively. The phase space is artificially mapped further as if any detector layer remains active but fully transparent, *i.e.* it means in particular that the map is derived as if ECal did not disturb or stop the particles but let them fly unaltered beyond the calorimeter lower radius. See text for explanation of the different labels.

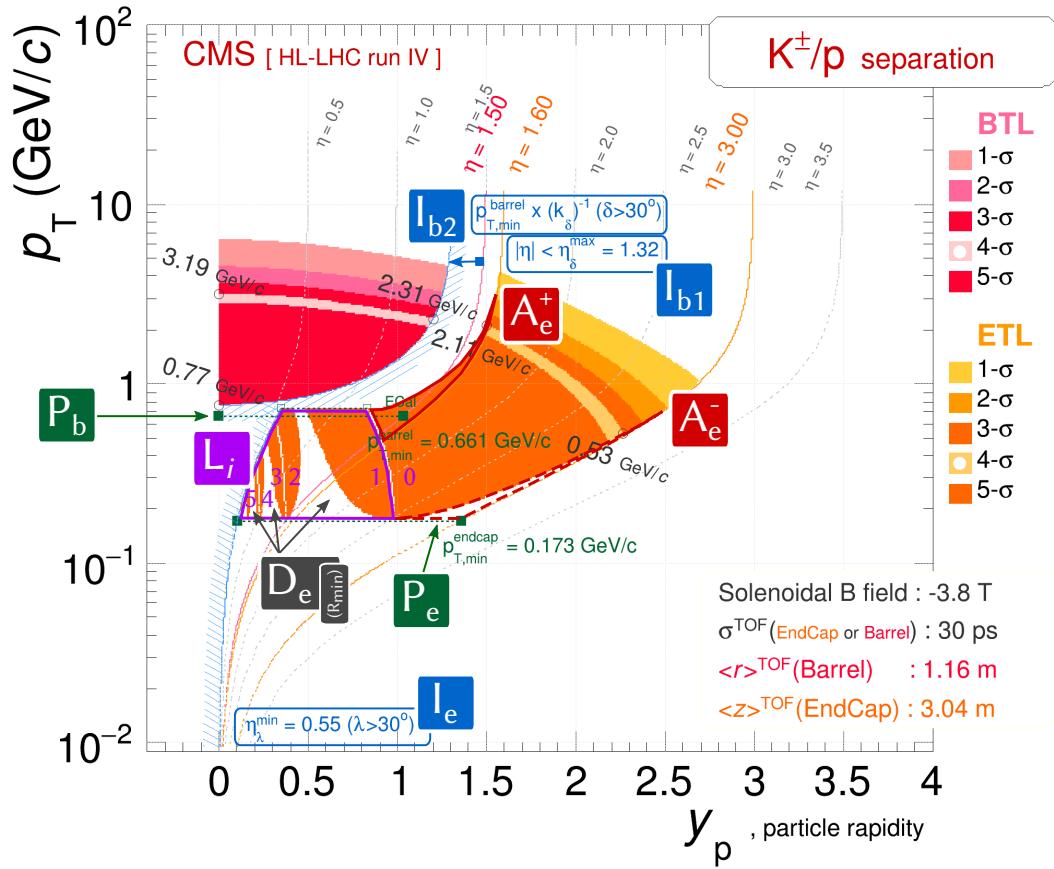


Fig. 23: Typical figure content with key elements highlighted, illustrated here with the K^\pm/p^\pm TOF separation in a CMS-like case. In the present illustration, the requested constraints on the inclination angles in barrel (δ) and endcap (λ) are set in both cases to 30° , a more realistic value. If the tracking and TOF layer are still considered as without effect on particles, the ECal is here envisaged as the term of the helical trajectory. See text for explanation of the different labels.

As explained in sub-section II-E.ii, the actual acceptances do depend on (p_T, y, B_Z) . Figure 22 gives a concrete illustration of the effect, where one can see the losses (red dashed broken lines) and gains (red solid broken line) in phase space, for barrel (A_b^-) and endcap (A_e^+ and A_e^-). Given the experimental layout chosen here, it is even up to the level where there are particles naively foreseen in barrel that in fact end up first and foremost into the endcap (e.g. primary protons of $p_T = 0.7 \text{ GeV}/c$, $\eta = 1.45$).

Label L_i : a peculiar case that to scrutinize concerns *looper* particles that finish their trajectory into the endcap ring. They can be defined as particles that perform at least one completed half-turn before reaching the TOF vertical plane. They are represented by the area framed in violet on Fig. 22 and Fig. 23. Their possible phase space is delimited by :

south : the TOF endcap comes necessarily with a lowest radius, below which the plane is not equipped anymore (beam pipe, services, ...). Such a minimal radius implies a minimum transverse momentum $p_{T\min}^{\text{endcap}}$ (Eq. 44a) for particles to have any chance to reach the active zone the TOF endcap ring.

west : an imposed minimal inclination angle to the endcap surface, translated in terms of minimal η_{\min}^λ , as is seen with the blue exclusion line labelled I_e

north : on the upper edge of the domain, two p_T quantities can border the looper acceptance :

- $p_{T\min}^{\text{barrel}}$ that favours the first detection into the TOF barrel,
- $p_{T\min}^{\text{ECal}}$, the p_T acceptance to enter the calorimeter.

Among the two thresholds, if looping up to $p_{T\min}^{\text{barrel}}$ only would be the most spontaneous option, it turns out that loops can decently happen up to the higher value of $p_{T\min}^{\text{ECal}}$. Such a quantity is defined by the B_Z field and the radial position of the barrel calorimeter, in the spirit of Eq. 42 defining $p_{T\min}^{\text{barrel}}$. In practice, setting the northern limit to $p_{T\min}^{\text{ECal}}$ means that one allows charged particles to cross the TOF barrel layer and continue their courses as long as they can, potentially up to the TOF endcap, implying a double acceptance, in both barrel *and* endcap, for some regions of phase space (p_T, y) . Such a double detection is apparently forbidden concretely in the specific setup studied in Fig. 23, but can be there potentially, behind the scene, as exposed in Fig. 22 where we see overlap regions between the red (barrel) and orange (endcap) areas. We will see later in this document experimental configurations where such barrel+endcap detections are present and may be more than the phoney case shown here for illustration. In a word, this will be important for cases where the barrel TOF layer is possibly at a much lower radius than ECal, stationed among the concentric layers of the tracker...

In terms of time separation, looper trajectories are generally from low- p_T particles shaping long track, this makes the identification clean ($> 5\sigma_{\text{TOF}}$ separation). The decisive issues are certainly not on the TOF timing itself but much more on the acceptance and efficiency aspects.

The tracking efficiency up to TOF plane is a prime issue, because with more and more half-turns, it is a longer and longer path to be carried out in the middle of the tracker material and thus, with more and more chances to loose energy, being scattered, etc. This makes the TOF detection less and less probable as the number of complete rotations grows (i.e. as the particle starts back with $y \rightarrow 0$). In real experiment, it is likely that the *western* limit of the looper domain will, rather than be defined by η_{\min}^λ usually taking values in a mid-rapidity scope, be set by a progressive degradation in efficiency, becoming irretrievable already with some still forward rapidities.

888 *east* : the looper area is in fact the set of sub-areas, made by populations of tracks having
 890 accomplished different numbers of half-turns. This is marked with violet numbers
 892 in the figures (0,1,2,3,4,5, ... half-turns). The limit between two consecutive half-
 894 turns is displayed with white solid lines. The first curled line at the largest rapidities
 896 stands for the first frontier, between 0 and 1 half-turn. In the “0” region, tracks
 stay in the same quadrant as the one they have been originating from (the azimuth
 difference $[\varphi(t_f) - \varphi(t_0)] \in [0; \pi/2]$), in the region “1”, they now rotate by more
 than 180° . For instance, the trajectory displayed in Fig. 9 with a rotation of 84°
 populates the region “0” (floor of the division $84./180.$), while Fig. 7 with a rotation
 of 623° enters the region “3” (floor of $623/180$), having done more than 1.5 full
 turns.

898 Labels $D_e(R_{\min})$ and $D_e(R_{\max})$: coming back to acceptance considerations for loopers into
 900 endcap, one should bear in mind that the looper area is not a continuous region but is in
 902 fact splitted into several pieces, each being associated to a certain number of half-turns
 and further separated by acceptance deadzones. To that respect, the fact that the endcap
 is not an infinite plane but a finite ring, with R_{\min} and R_{\max} , is the reason for such a
 twisted acceptance.

904 On the low p_T side, the R_{\min} value is responsible of the acceptance losses, the large
 906 white gaps in the shape of an orca dorsal fin, appearing between region “1” and “2”, “3”
 and “4”, visible on both Figs. 22 and 23. The trajectory visualised in Fig. 8, escaping
 surprisingly the TOF endcap acceptance by the low radius, is an example of trajectory
 908 that counts among the ones populated the first large white deadzone, between the orange
 regions “1” and “2”.

910 On the high p_T front, conversely, the acceptance irregularities stem from the outmost
 912 limit of the endcap ring with R_{\max} ; depending on its value, the dip (only visible in Fig. 22)
 separating region “2” and “3”, “4” and “5”, etc can be more or less pronounced : with a
 larger radius, the acceptance losses are reduced, the accessible phase space being pushed
 914 to higher p_T values.

916 Labels I_{b1} and I_{b2} : Requiring a minimal inclination angle δ to tackle the barrel TOF surface
 918 translates into 2 conditions to satisfy, on η and p_T . The upper bound η_δ in pseudo-
 rapidity defines the vertical asymptote to the curve that uplifts the $p_{T\min}^{\text{barrel}}$ as a function
 of η via the factor $(k_\delta)^{-1}$ (Eq. 46). The trend previously exposed with numbers in Tab. 3
 can be visualised in the figures, the slow increase at first followed by an exponential rise
 920 near the asymptote. Note that, for inclination angles $\delta = 30^\circ$ or 25° , such a modulation of
 $p_{T\min}^{\text{barrel}}$ becomes the most stringent constraint, superseding the acceptance considerations
 922 of A_b^- . At more moderate angles (20° , 15°), the effects remain sensible but only up to a
 certain p_T after which the acceptance losses A_b^- become dominant, if any. Lower angles
 924 ($< 15^\circ$) are almost of no consequence in terms of acceptance losses, as can be seen from
 Fig. 22 with $\delta = 10^\circ$, η_δ being rejected to high pseudo-rapidity values that are more
 926 typical of endcap detectors rather than barrel ones.

928 Label I_e^λ : The requirement of a minimal inclination angle λ for the TOF endcap results in a
 minimal η_{\min}^λ , typically repelled back to mid-rapidity values. It is of no effect for casual
 track directed to endcap, but is the ultimate limit for looper tracks.

Physics aspect	Considered here ?	Label in Fig. 22	Section	Eq.
Core hypotheses				
. Hyp. 1, no energy loss of any kind	✓	-	II-B	-
. Hyp. 2, static and homogeneous B_z field	✓	-	II-B	-
. Hyp. 3, (primary) particle emitted at (0,0,0)	✓	-	II-C.ii	-
. Hyp. 4, simplified TOF geometry (rotation inv.)	✓	-	II-C.ii	-
Trajectory approximations				
. Ideal helix derivation (\mathcal{L}, t_f)	✓	-	II-E.iii	Eq. 31f
. Straight line approx. (a) [tangent(t_0)]	-	✗	II-E.iii	-
. Straight line approx. (b) [PV to TOF hit]	-	✗	II-E.iii	-
Trajectory details				
. TOF η acceptance = $f(p_T, \eta)$	✓	-	A_x^\pm	II-E.ii -
. Looper particles towards endcap	✓	-	L_i	II-E.iv -
Minimum p_T				
. Barrel minimal p_T	✓	-	P_b	II-F.i Eq. 42
. Endcap minimal p_T	✓	-	P_e	II-F.i Eq. 44a
Inclination angle to TOF surface				
. max. η_δ for barrel tracks	✓	-	I_{b1}	II-F.ii Eq. 47a
. $(k_\delta)^{-1}$ factor for barrel tracks	✓	-	I_{b2}	II-F.ii Eq. 46
. η_{\min}^λ for looper in endcap	✓	-	I_e	II-F.iii Eq. 49a
Extra concrete considerations				
. Endcap deadzones for loopers	✓	-	$D_e(R)$	II-E.iv -
. $(\mathcal{A} \cdot \mathcal{E})_{\text{TOF}} = f(\text{species})$	-	✗		IV-C.i -
. p_T resolution = $f(\text{species}, p_T, \eta, x/X_0, B_z)$	-	✗		-
. Electric charge determination	-	✗		-
. $\sigma_{\text{evt}-t_0} = f(h^\pm \text{ multiplicity})$	-	✗		IV-C.iii -
. TOF hit background effects	-	✗		IV-C.iv -

Table 6: List of analytical aspects that are considered in the plotted TOF separation performances.

Experiment	$\langle R_{\text{TOF}}^{\text{barrel}} \rangle$	$\Delta\eta_{\text{barrel}}$	$\langle Z_{\text{TOF}}^{\text{endcap}} \rangle$	$\Delta\eta_{\text{endcap}}$	Timing resolution	B_z field	Figure
ALICE-1	• 3.80 m	• < 0.88	-	-	• 80 ps	• 0.5 T	Fig. 14
ALICE-1	• 3.80 m	• < 0.88	-	-	• 56 ps	• 0.5 T	Fig. 15
ALICE-1	• 3.80 m	• < 0.88	-	-	• 56 ps	• 0.2 T	Fig. 16
ALICE-3	1.00 m	< 1.40	2.00 m	1.5; 4.0	10 ps	• 0.2 T	Fig. 30
ALICE-3	1.00 m	< 1.40	2.00 m	1.5; 4.0	10 ps	• 0.5 T	Fig. 31
ALICE-3	1.00 m	< 1.40	2.00 m	1.5; 4.0	10 ps	1.0 T	Fig. 32
ALICE-3	1.00 m	< 1.40	2.00 m	1.5; 4.0	20 ps	• 0.2 T	Fig. 33
ALICE-3	1.00 m	< 1.40	2.00 m	1.5; 4.0	20 ps	• 0.5 T	Fig. 34
ALICE-3	1.00 m	< 1.40	2.00 m	1.5; 4.0	20 ps	1.0 T	Fig. 35
ALICE-3	1.00 m	< 1.40	2.00 m	1.5; 4.0	30 ps	• 0.2 T	Fig. 36
ALICE-3	1.00 m	< 1.40	2.00 m	1.5; 4.0	30 ps	• 0.5 T	Fig. 37
ALICE-3	1.00 m	< 1.40	2.00 m	1.5; 4.0	30 ps	1.0 T	Fig. 38
ALICE-3	0.20 m	< 1.40	2.00 m	1.5; 4.0	10 ps	• 0.2 T	Fig. 39
ALICE-3	0.20 m	< 1.40	2.00 m	1.5; 4.0	10 ps	• 0.5 T	Fig. 40
ALICE-3	0.20 m	< 1.40	2.00 m	1.5; 4.0	10 ps	1.0 T	Fig. 41
ALICE-3	0.20 m	< 1.40	2.00 m	1.5; 4.0	20 ps	• 0.2 T	Fig. 42
ALICE-3	0.20 m	< 1.40	2.00 m	1.5; 4.0	20 ps	• 0.5 T	Fig. 43
ALICE-3	0.20 m	< 1.40	2.00 m	1.5; 4.0	20 ps	1.0 T	Fig. 44
ALICE-3	0.20 m	< 1.40	2.00 m	1.5; 4.0	30 ps	• 0.2 T	Fig. 45
ALICE-3	0.20 m	< 1.40	2.00 m	1.5; 4.0	30 ps	• 0.5 T	Fig. 46
ALICE-3	0.20 m	< 1.40	2.00 m	1.5; 4.0	30 ps	1.0 T	Fig. 47
CMS	• 1.16 m	• < 1.48	• 3.04 m	• 1.6; 3.0	• 30 ps	• 3.8 T	Fig. 48
CMS	• 1.16 m	• < 1.48	• 3.04 m	• 1.6; 3.0	• 30 ps	1.9 T	Fig. 49
ATLAS	0.29 m	< 1.00	• 3.45 m	• 2.4; 4.0	• 32 ps	• 2.0 T	Fig. 50
ATLAS	0.29 m	< 1.00	• 3.45 m	• 2.4; 4.0	• 32 ps	1.0 T	Fig. 51
ATLAS	1.00 m	< 1.00	• 3.45 m	• 2.4; 4.0	• 32 ps	• 2.0 T	Fig. 52
ATLAS	1.00 m	< 1.00	• 3.45 m	• 2.4; 4.0	• 32 ps	1.0 T	Fig. 53
ATLAS	0.29 m	< 1.00	1.50 m	1.22; 2.1	20 ps	• 2.0 T	Fig. 54
ATLAS	0.29 m	< 1.00	1.50 m	1.22; 2.1	20 ps	1.0 T	Fig. 55
ATLAS	1.00 m	< 1.00	1.50 m	1.22; 2.1	20 ps	• 2.0 T	Fig. 56
ATLAS	1.00 m	< 1.00	1.50 m	1.22; 2.1	20 ps	1.0 T	Fig. 57

Table 7: List of the various TOF configurations tested and the corresponding figures. Values marked with • are the numerical values essentially established, either because they are in fact actual (ALICE-1), because they are quoted in the Technical Design Report of the corresponding sub-detectors anticipated for HL-LHC run IV (CMS MTD, ATLAS HGTD) or because they are simply the most plausible (B field).

930 VI Specifications and technological choices, ALICE-3 compared 931 to ATLAS and CMS

932 The initial proposal for the ALICE-3 experiment [1] includes one TOF sub-detector, in the
933 central barrel, towards the outer radius of the experiment, at about 1 m radial distance from the
934 beam interaction region.

On the hardware side, such a TOF detector would consist of CMOS Monolithic Active Pixel
936 Sensors (MAPS) combining both the sensitive part and the readout part, likely either based
937 on Low-Gain Avalanche Detectors (LGAD) architecture (with moderate reverse bias voltage
938 of the photodiode to work under a linear gain) or ideally on Single-Photon Avalanche Diode
939 (SPAD) architecture (with reverse bias voltage above the breakdown value letting the diode
940 operating in Geiger mode). The exact architecture among these two families is not yet decided
and calls for dedicated R&D in the coming years.

942 This poses the question of what will be the desired specifications for such a TOF detector in
ALICE-3.

944 Before answering to that question, let us first present the associated situation of instrumentation
research, to my current knowledge, dominated by LGAD technologies. At CERN, there is an
945 ongoing R&D programme, RD50, dedicated to “Radiation hard semiconductor devices for very
high luminosity colliders” [24]. LGAD technologies count among the sub-projects explored.
948 The goal is to provide *tracker* (*i.e.* not TOF as prime intention) technologies that are time
aware and time accurate, to enable tracking in 3+1D in the context of experiments exposed
950 to very high instantaneous flux of particles. With the ever increasing luminosity of HL-LHC,
some instrumented regions of ATLAS and CMS in runs IV and beyond will be more and more
952 severely irradiated; the radiation tolerance is typically the most stringent factor to satisfy in this
framework and is kept as the principal headline. In the context of the R&D programme, the
954 targeted level of radiation hardness are typically up to $\mathcal{O}(10^{16} \text{ 1-MeV } n_{eq}/\text{cm}^{-2})$.

For ALICE-3, the radiation tolerance will be a much less critical parameter : levels below
956 $\mathcal{O}(10^{12} - 10^{14}) \text{ 1-MeV } n_{eq}/\text{cm}^{-2}$ depending on the radial position within the experiment would
suffice, whereas such levels are nowadays already in the ballpark of the achieved radiation
958 tolerances $\mathcal{O}(10^{15}) \text{ 1-MeV } n_{eq}/\text{cm}^{-2}$. In the case of ALICE-3, the stress for the TOF detector
will be focused elsewhere, on other critical design parameters :

- 960 • the timing resolution must be as low as $\mathcal{O}(10\text{-}20 \text{ ps})$;
- the spatial resolution must be precise and as much as possible in line with the tracker preci-
962 sion, $\mathcal{O}(5\text{-}10 \text{ }\mu\text{m})$, usually obtained with pixels $\mathcal{O}(25 \times 25 \text{ }\mu\text{m}^2)$;
- last but not least, the material budget should absolutely be drastically limited [$\mathcal{O}(0.1\% \text{ } X/X_0)$
964 per silicon layer (sensor + read-out), considering that adjunct mechanics and services to
MAPS will typically contribute dominantly to an extra $1\% \text{ } X/X_0$ per layer or so].

966 The LGAD chosen by CMS and ATLAS for their respective endcap pile-up tagger in HL-LHC
run IV will not be properly suited for ALICE-3 :

- 968 • the timing resolution is a bit higher ($\mathcal{O}(30\text{-}40 \text{ ps})$) than what would be desired for ALICE-3.
- the spatial resolution is degraded by rather large pixel/pads size. It will be $1.3 \times 1.3 \text{ mm}^2$ for
970 both CMS and ATLAS LGAD in endcap, giving a typical spatial resolution of $1.3 \text{ mm}/\sqrt{12}$
 $= 375 \text{ }\mu\text{m}$.
- 972 • ATLAS and CMS LGAD are *hybrid* pads, that is the front-end electronics is not embedded
in the chip itself but is a secondary and independent application-specific integrated circuit
974 (ASIC), separated from the sensitive volume; it needs to be bump-bonded thus coming
with substantial added costs for the detector production (3.5 MCHF for electronics out of

- 976 a total 10.9 MCHF (Tab. 6.5 in [8]), to equip the $2 \times 31.6 \text{ m}^2$ – 2 sides, forward and
 978 backward, $\times (2+2)$ disks per side, with 4.0 m^2 active per disk – for the CMS timing endcaps;
 980 0.73 MCHF for front-end ASIC and 0.90 MCHF for bump-bonding in the ATLAS timing
 endcap out of a total cost at 8.5 MCHF (Tab. 6.3 in [25]), to instrument $2 \times 4.2 \text{ m}^2$ – 2 sides,
 forward and backward, $\times (2+2)$ disks per side, with 1.0 m^2 active per disk – for the ATLAS
 timing endcaps.
- 982 • the material budget ranges from moderate to high (*e.g.* $\approx 2 \text{ cm}$ -thick per disk, Fig. 4.11 and
 Tab. 4.3 in [25]), out of which silicon constitutes only a $50\text{-}\mu\text{m}$ -thick active part overlaid
 984 on a $300 \mu\text{m}$ substrate. If the active LGAD sensor limits its power density to about 30
 mW/cm^2 , the associated ASIC consumes and dissipates $\mathcal{O}(200 \text{ mW}/\text{cm}^2)$ (section 5.1 in
 986 [25]), needing for substantial cooling (liquid CO_2), and thus extra material, to maintain
 operations at -30°C .
 - 988 • the so-called *fill factor*, defined by the ratio between the active area of the sensor to the total
 surface of the latter, is restricted, *e.g.* 85% in the case of CMS LGAD (section 3.2.4.1 in
 990 [8]) and would in fact further decrease for smaller pad sizes due to incompressible no-gain
 areas and inter-pad guard rings ($\approx 40\text{-}80 \mu\text{m}$ currently). To recover a complete hermiticity,
 992 a stack of several contiguous layers is required (2 double-sided disks, *i.e.* 4 planes, for both
 CMS (Fig. 3.2 in [8]) and ATLAS (section 4.1 in [25]) and thus, coming with extra material
 994 budget.

Note that on the hybrid LGAD front, there are recent developments promising substantial im-
 996 provements in terms of spatial resolution $\mathcal{O}(50 \mu\text{m})$, thickness of the sensitive part $\mathcal{O}(50 \mu\text{m})$ ⁸
 and fill factor pushed at 100% while keeping similar timing resolution $\mathcal{O}(40 \text{ ps})$. This progress
 998 are connected to Trench-Isolated Low Gain Avalanche Diodes, *TI-LGADs* [26] and more espe-
 cially to Resistive AC-coupled LGAD referred to *RSD* and equivalently to *AC-LGAD* in the
 1000 literature [27, 28].

VII TOF measurements in ALICE-3 (HL-LHC run V)

VII-A Configuration with a TOF as barrel outer layer at $R = 1 \text{ m}$

1002 In the original proposal for the ALICE-3 experiment [1], there is only one TOF sub-detector,
 1004 covering a η range of ± 1.4 , located in the barrel region at a radius of about 1 m, immediately
 between the last tracking layer and the electromagnetic pre-shower.

1006 Such a configuration is part and parcel of the first set of exercises in place in the current work.
 As the exact magnetic field is not decided, 3 options are tested, two corresponding to ALICE-3
 1008 continuing to use the L3 magnet already available at the experimental point, offering the pos-
 sibility of 2 distinct field intensities, $B_z = \pm 0.2 \text{ T}$ and $\pm 0.5 \text{ T}$, one introducing the possibility to
 1010 build and use a new magnet delivering higher field, here considered at $\pm 1.0 \text{ T}$.

As far as the timing resolution is concerned, given the uncertainty on the retained technology,
 1012 3 values are tested, 10 ps, 20 ps and 30 ps. All in all, conjugating the B_z fields with the various
 timing resolutions, 9 figures are needed to present the TOF performances for the 1.0-m central
 1014 TOF configurations in ALICE-3, ranging from Fig. 30 to Fig. 38.

For any figure, the minimal inclination angle in barrel has been set to a value $\delta > 30^\circ$. Note
 1016 that, under such a request, if it turned out that particle detection or tracking indeed failed at
 such a low inclination angle, the graphs argue further that it would not make any sense to
 1018 instrument the central barrel to values above $\eta_\delta = 1.32$: particles beyond that threshold will

⁸ *i.e.* read-out thickness excluded. The sensitive silicon part that is thinned further from about $300 \mu\text{m}$ to the
 mentioned $50 \mu\text{m}$.

never be properly reconstructed and identified; the barrel detector in that more forward range would then be worth for nothing except producing secondary interactions.

On the domain where particles cross the TOF layer with a large enough angle, one can now discuss the accessible momentum span. A general observation is that, depending on B_z but independently of the timing resolution, the minimal p_T reach goes from 40 MeV/c to 180 MeV/c via 90 MeV/c for ($q = \pm 1e$) particles and with twice larger values for ($q = \pm 2e$).

At the other end of the momentum range, at high p_T , the magnetic field is of almost no consequence. For a given $R_{\text{TOF}}^{\text{barrel}}$, the timing resolution σ_{TOF} essentially drives the particle separation and sets the upper p_T limit, the latter being species dependent (m_0 and y). The larger the mass, the further upwards the last p_T is theoretically repelled. On that upper front, to maintain more or less the same separation power as in ALICE-1 ($R_{\text{TOF}}^{\text{barrel}} = 3.8$ m, $\sigma_{\text{TOF}} = 80$ ps), a timing resolution of 20 ps or below is necessary for the ALICE-3 TOF. (The TOF radial location being divided by a factor 4, the timing resolution needs correspondingly to be improved by a factor 4 or so...) This can be observed by comparing for instance Fig. 14 for ALICE-1 with Fig. 34 for ALICE-3, both having $B_z = 0.5$ T.

One may give dedicated considerations to specific separations :

separation (e^\pm/π^\pm) : the separation covers very low p_T , in the region where we can reconstruct low-mass di-electrons (study of the thermal radiations of virtual photons in the low energy side – that is, late in the medium history, when it is getting colder –, chiral symmetry restoration effects). The separation is such that, in a default configuration [$B_z = 0.5$ T; $\sigma_{\text{TOF}} = 20$ ps, Fig. 34(a)], the distinction e^\pm/π^\pm would be effective up to $2 \times p_T(e^\pm) \approx m[\phi(1020)] = 1.020$ GeV/c². On the opposite side, at high p_T , even with a 10-ps resolution, the identification will not permit di-electron identification in view of the reconstruction of charmonia $c\bar{c}$ (J/ψ , $\psi(2S)$, $\chi_{cJ} \rightarrow J/\psi$, ...) with $m[J/\psi] = 3.097$ GeV/c², and even less for bottomonia $b\bar{b}$ ($\Upsilon(\text{nS})$, ...) with $m[\Upsilon(1S)] = 9.460$ GeV/c². The pre-shower detector of ALICE-3 needs to relay TOF on such a higher-momentum front.

separation ($t/{}^3\text{He}$) : the case appears rather delicate, as already suggested earlier in sub-section IV-C.iv. The difference of path length \mathcal{L} between ($q = \pm 1e$)- and ($q = \pm 2e$) particles of similar masses remains a small quantity. In the most favourable case – high B_z field (1.0 T), lowest σ_{TOF} (10 ps), at the foreseen outmost radius for a TOF layer (1.0 m), that is Fig. 32 – the accessible phase space where a separation is possible is restricted to a momentum range going from $p_T = 0.35$ GeV/c to 1.49 GeV/c at $y = 0$ and in fact, unlike any other separation, (mildly) grows while moving to the edge of the central barrel (1.61 GeV/c). In contrast, for instance, the analytical separation d^\pm/t covers 13 GeV/c under the same experimental configuration. The endcap plays here no role : t and ${}^3\text{He}$ heading into the endcap acceptance, loopers or regulars, are simply never separated. Broadly speaking, the case is very sensitive to σ_{TOF} and B_z , it can vanish rapidly with reduced B_z and degraded σ_{TOF} .

VII-B Configuration with a TOF as barrel intermediate layer at $R = 0.2$ m

With a default field at $|B_z| = 0.5$ T, the transverse momentum entry of the TOF barrel acceptance at 1.0 m is evaluated analytically at 90 MeV/c. In the real experiment, the threshold will certainly be uplifted, especially for species of increasing mass m_0 for which the efficiency curve is usually shifted towards higher momenta (see sub-section IV-C.i).

In order to bridge the gap and still, uniquely at the LHC, enable particle identification at the lowest momenta, *i.e.* $p_T < 0.15$ GeV/c, one is led to consider a second TOF layer at lower radial

1064 position. This would be a prominent feature to have, in order to fully explore the “ultra soft
 1066 sector”. The physics cases go from the identification of soft electrons coming from thermal ra-
 1068 diations or from photon conversion of the soft γ issued by a χ_{cJ} decay that one is after for years,
 1070 to Fourier coefficients v_n for identified hadrons down to mild-relativistic momenta to dispute
 the validity limit of hydrodynamics, via ultra-soft charged pions to test the pions correlations at
 the chiral phase transition (Bose-Einstein pion condensate, Disoriented Chiral Condensate, ...)
 [29] or measurement of net quantum number fluctuations (charge, baryon number, strangeness)
 to challenge almost directly Lattice QCD sheer predictions [30].

1072 Here a configuration with $R = 0.2$ m is tested, again under the same various B_z and σ_{TOF} , with
 $\delta > 30^\circ$. The results can be seen from Fig. 39 to Fig. 47

1074 Note that the point would not be to choose among the TOF layer location at $R = 1.0$ m and
 at a lower radius, but to have both layers, thus providing frequently 2 TOF measurements per
 1076 track. This would help in terms of PID (for primary particles but also for identification of
 secondaries), it would help also in terms of tracking and pile-up management (primarily out-
 1078 of-bunch but also to a certain extent, in-bunch pile-up) by introducing a time component as
 extra information.

1080 For elegant the idea may appear, it needs nonetheless to be precisely evaluated technically. It
 goes without saying that placing a hybrid LGAD packed in a 7.5 cm-thick integration environ-
 1082 nment in the middle of one of the most lightweight tracker ever considered is not a viable option.
 For such a TOF idea to happen, it necessarily requests the TOF detection based on a MAPS
 1084 architecture⁹ to become a fact in the next 8 years. Furthermore, with a fill factor close to 100%
 in order to limit the number of sensor layers (2-3) to be stacked for the sake of hermeticity.
 1086 This way only, the extra material budget due to the integration of an extra intermediate TOF
 layer coming to complement a tracker one will be bearable, $+O(1\% \times X_0)$.

1088 In terms of area to instrument, a TOF at $R_{\text{TOF}}^{\text{barrel}} = 0.2$ m covering $\pm 1.4 \eta$ units is embodied by a
 cylinder extended to $\pm Z_{\text{TOF,max}}^{\text{barrel}} = \pm 0.38$ m, thus covering an area of $2\pi R_{\text{TOF}}^{\text{barrel}} \cdot 2Z_{\text{TOF,max}}^{\text{barrel}} \approx 1 \text{ m}^2$
 1090 per sensitive layer entering the TOF stack (typically 1-, 2- or 3-cylinder stack). Such a surface
 can be compared to the surface of the basic barrel option with $R_{\text{TOF}}^{\text{barrel}} = 1.0$ m; the surface per
 1092 sensitive cylinder is there $2\pi R_{\text{TOF}}^{\text{barrel}} \cdot 2Z_{\text{TOF,max}}^{\text{barrel}} \approx 2\pi(1 \text{ m}) \cdot 2(1.9 \text{ m}) \approx 24 \text{ m}^2$.

VII-C Possibility to have endcap TOF planes

1094 In the first thoughts given to ALICE-3 [1], no TOF endcap has been anticipated. The benefit
 of such an option has been studied in this document and the case is brought to the limelight for
 1096 the sake of the discussion. Note that, as the first attempt here, the TOF endcap has been chosen
 to be located at the extreme position of the forward tracker, at $Z_{\text{TOF}}^{\text{endcap}} = 2.0$ m, just before
 1098 the ultimate plane that the pre-shower defines. It is further considered here to cover a pseudo-
 rapidity scope ranging from 1.5 to 4.0. If it makes sense physics-wise to push the instrument as
 1100 forward as possible (and ignore for a moment the issues of radiation tolerance, integration, etc
 encountered there...), one must be at least reasonable for the starting upper edge of the endcap.
 1102 A gap of at least 0.1 unit in η is likely necessary to fit in the mechanical structure, to let the
 wires and services pass between the barrel and the endcap, not only for TOF layers and planes,
 1104 but also for tracker layers and planes. Still, at $R = 1$ m, 0.1 unit in η corresponds to a gap
 of about 10 cm only between the outmost z value of the TOF barrel $Z_{\text{TOF,max}}^{\text{barrel}}$ and the location
 1106 $Z_{\text{TOF}}^{\text{endcap}}$.

For any figure, the minimal inclination angle in endcap has been requested to a value $\lambda > 30^\circ$.

⁹ Given the prime role led by SPAD architectures in industry, SPAD would be the most promising candidates *a priori* to achieve this.

1108 On a general note, one can draw the reader’s attention upon the effects of the magnetic field.
 1109 These are manifold. As for the barrel region, B_z does not change (this time, *strictly* does not
 1110 change) the upper limits of TOF separations. B_z modifies however the acceptance in a sig-
 1111 nificant way. Stronger B_z implies that the “north” and “south” borders, $p_{T\min}^{\text{ECal}}$ and $p_{T\min}^{\text{endcap}}$,
 1112 are uplifted. Stronger and stronger magnetic also dig further the deadzones for the looper par-
 1113 ticles (the aforementioned orca’s dorsal fin appearing regularly), making the detection phase
 1114 space more and more splitted. Behind the scene, and on a positive note, one should how-
 1115 ever acknowledge that stronger B_z certainly also means that the p_T resolution of particles in
 1116 endcap acceptance may be characterised with a more precise transverse momentum resolution
 1117 (stronger curvature would be beneficial for tracks which total momentum can quickly become
 1118 quite high ($p_{\text{tot}} = p_T \cosh(\eta)$) and thus complicating the p_T determination : the particle escapes
 the experiment promptly before being bent timely).

1120 In terms of PID performances, looking at the endcap maps in ALICE-3 figures, the reader
 1121 may object that the $4\text{-}\sigma_{\text{TOF}}$ separation remains limited, in terms of p_T reach. Even sometimes
 1122 *very* limited in p_T as we move to more and more forward η ... “The endcap case for ALICE-3
 1123 looks feeble”, one may think. However, after second thoughts given along the present lines,
 1124 several reasons could in fact argue decisively in favour of having a TOF plane in the endcap.
 In the following, we list such rationale, from the most immediate to maybe the least obvious
 1126 argument.

1. Forward PID : The possibility to have PID information at forward rapidity would improve
 1128 the detector hermiticity on the identification front. It means that PID could be further
 1129 exploited over a complete η coverage and fair p_T range for complex cascade decays
 1130 hinged on 3 to 6 final state particles spread over large η domains [like multi-charm
 1131 baryons : $\Lambda_c^+(udc)$, $\Xi_c^+(usc)$, $\Xi_c^0(dsc)$, $\Omega_c^0(ssc)$, $\Xi_{cc}^{2+}(ucc)$ $\Omega_{ccc}^{2+}(ccc)$]. It means that studies
 1132 of n -particle correlations could be performed at (very) low p_T with PID over the whole
 1133 η coverage of the experiment. It means that multiplicity-dependent studies like the ones
 1134 performed with VOM in ALICE-1 [31] could be further tailored from $p_T \approx 0$ but now
 with supplemental PID information exploited for the multiplicity estimator.

2. Possible acceptance redundancy : for a TOF barrel layer located among the tracker layers
 1136 (*e.g.* $R = 0.2$ m), a TOF endcap would have in common some regions of phase space
 1137 with such an inner TOF layer, offering possibly double TOF information with a first hit
 1138 in barrel followed by its complement in endcap. This would be beneficial at least for
 1139 mutual calibration purposes. Figures 39 to Fig. 47 pin point the (p_T, y, m_0) locations
 1140 where such redundancies would happen.

1142 In concrete terms, the exact frequency of such opportunities per event would be to be
 1143 assessed with fast or full simulations, the exact experimental layout and the material
 1144 budget distribution will be of strong influence.

3. Pile-up tagger : if CMS and ATLAS may use their pile-up tagger as TOF detector, it could
 1146 be conversely convenient for ALICE-3 to use its TOF detectors as pile-up tagger. On the
 1147 one hand, ALICE intends to harvest Minimum Bias events in their individual entirety¹⁰
 1148 in astronomic quantities. On the other hand, such a collection has to be performed with,
 1149 ideally native “zero” pile-up contamination per event, at the very least, with thorough and
 1150 fully mastered pile-up tagging. Such a mitigation is a crest line to find in the data taking
 1151 strategy. It inescapably implies that the full-event record take its (necessary) time, while
 1152 we always wish/are wished to be faster. To that end, comprehensive timing information
 1153 will be much appreciated when LHC conditions will become more and more stringent for
 1154 the experiment / sub-detectors with the slowest read-out. (To give a leading-order idea

of the problem, bear in mind the 25-ns bunch spacing in LHC compared to the typical $\mathcal{O}(1-10 \mu\text{s})$ resolution of MAPS read-out in tracker.)

4. *Reducing $\sigma_{\text{evt}-t_0}$* : by extending the TOF acceptance and thus the additional particles at hand, one can reduce the uncertainty on $\sigma_{\text{evt}-t_0}$ (see sub-section IV-C.iii). This will be especially beneficial in low-multiplicity collisions like pp p-A and peripheral A-A.

5. *Escaping $y \rightarrow 0$* : the reader should note in the figures how the barrel coverage narrows down to y almost zero as one moves towards lower and lower p_T . For $p_T < 0.1 \text{ GeV}/c$, the full rapidity coverage of the central barrel is for most of the hadronic species reduced to $|y| < 0.3$; at $p_T < 0.05 \text{ GeV}/c$, to $|y| < 0.1$. And it is essentially $|y| = 0$ for light nuclei below $0.1 \text{ GeV}/c$. Provided that a low material budget preserves some decent or high $\mathcal{A} \cdot \varepsilon$ to the forward directions, the opportunity of an endcap TOF information put the ALICE experiment in capacity to extend its low- p_T studies to more forward rapidities. For protons and light nuclei, by profiting from the extra Lorentz boost given along p_z , TOF *forward* endcaps could become perhaps the only effective way to identify *mid-rapidity* populations at $p_T \approx 0$.

To follow-up on such a proposal, and foster any subsequent discussion to have in term of cost and integration issues, one can mention the corresponding detector surface at stakes. It would be a matter of instrumenting 2 sides of the experiments, forward and backward regions, to cover 1.5 to 4.0 units of $|\eta|$, at $Z_{\text{TOF}}^{\text{endcap}} \approx \pm 2.0 \text{ m}$. It translates to disks extending from $R_{\text{TOF,min}}^{\text{endcap}} = 0.073 \text{ m}$ to $R_{\text{TOF,max}}^{\text{endcap}} = 0.939 \text{ m}$. The corresponding ring surface to equip become then $\pi(R_{\text{TOF,max}}^{\text{endcap}^2} - R_{\text{TOF,min}}^{\text{endcap}^2}) = 2.75 \text{ m}^2$ per disk. Each TOF endcap would then consist of a stack of disks of that kind, 1 to 4 disks typically depending on the desired redundancy and the fill factor of the chosen MAPS architecture. Such an endcap surface of 2.75 m^2 per active disk can be related to the aforementioned 24 m^2 per active cylinder of the basic option for barrel TOF ($R_{\text{TOF}}^{\text{barrel}} = 1 \text{ m}$).

The integration and the radiation hardness specifications could potentially be eased by reducing the η most forward edge from 4.0 to a lower value (3.5, 3.0, ...).

The cost could be reduced essentially by reducing the equipped area. There are two pragmatic lever arms to do that :

- at a given $Z_{\text{TOF}}^{\text{endcap}}$, the upper radius of the endcap could be shrunked, which is likely not so desirable if we want to assure as much as possible the continuity of measurement (p_T upper reach for separations) with the barrel TOF at $R_{\text{TOF}}^{\text{barrel}} = 1.0 \text{ m}$.
- for a given η coverage, we could move the TOF endcap plane closer to the interaction point. This will come with a mild reduction of the p_T upper reach for separation but a clearly reduced area. Located at $Z_{\text{TOF}}^{\text{endcap}} = 1.5 \text{ m}$, still covering 1.5 to 4.0 units of pseudo-rapidity, the surface per disk would be reduced by 45% to $\pi(0.70^2 - 0.05^2) = 1.5 \text{ m}^2$. This implies that the chosen architecture and its integration appendices are of limited material budget, because under such circumstances, the TOF endcap will be located in the middle of the forward tracker. The forward direction coming intrinsically with the longitudinal boost p_z makes the consequences of the material budget less dramatic compared to mid-rapidity TOF at $R_{\text{TOF}}^{\text{barrel}} = 0.2 \text{ m}$ but still, given the targeted low momenta, the issue at forward rapidity may well remain a bottleneck.

¹⁰ We are not focusing on individual particles, QGP physics is a high-energy physics in which the event context does matter, being on a same footing with the particle species of interest. It entails that the collision “event” cannot be amputated, easily and harmlessly, without a potential loss of scientific material...

VIII TOF measurement in CMS (HL-LHC run IV and V)

1198 Among the choices already made by the CMS collaboration for its strategical upgrades (Long
1200 Shutdown 3, 2025-27) in view of HL-LHC run IV, a detector meant to tag and sort pile-up
1202 events has been casted, MIP Timing Detector (MTD) (see Technical Design Report [8]). The
task for a such a detector is to stamp particle detection with a time resolution below the HL-
LHC bunch spacing (typically $\mathcal{O}(25\text{ ns})$) and further help to parse in-bunch pile-up. The detec-
tor consists of two components :

- 1204 (i) one cylindrical layer at central rapidity, the Barrel Timing Layer, BTL, covering
1206 $|\eta| < 1.48$, based on LYSO/Ce crystals and SiPM readout, positioned at an average
radius $r = 1.16\text{ m}$.
- 1208 (ii) two endcap planes at forward and backward pseudo-rapidities, the Endcap Tim-
ing Layer, ETL, covering $1.6 < |\eta| < 3.0$, based on Low-Gain Avalanche Detectors
(LGAD), positioned at an average distance $|z| = \pm 3.04\text{ m}$.

1210 On both parts, the expected timing resolution should be of 30 ps, degrading a bit to 50 ps with
the accumulated luminosity (Fig. B.10 in [8]).

1212 A side-product of such a detector is its usage as a TOF detector, as reported in the same TDR
[8] in Fig. 1.5 p.8 (separation power for π^\pm/K^\pm and K^\pm/p^\pm) and Fig. 5.23 p.222 (simulation of
1214 β_{tot} distributions as a function of total momentum p_{tot} , with Hydjet in A–A for BTL and for
ETL).

1216 In the present document, the default results exposed in the TDR (Fig. 1.5) for a magnetic field
of 3.8 T have been extended with further cases of particle separations (Fig. 48). As an extra
1218 scenario, an example configuration with twice lower magnetic field (1.9 T) has been tested
(Fig. 49), in order to assess a possible gain towards low p_T at both mid- and forward rapidities
1220 due to a reduced magnetic field. In any case, the minimal inclination angle in the barrel has
been set to a value $\delta > 30^\circ$, in the endcap, to $\lambda > 30^\circ$.

1222 The TOF PID competitiveness of CMS with respect to ALICE-3 will be driven essentially by
aspects escaping the analytical formulae presented here. These aspects encompass considera-
1224 tions of scientific strategy, of detector as well as of native physics :

1226 1. One run ahead : the simple fact that MTD will exist and will be a reality almost for certain :
the project is already approved by CERN authorities and collaboration, the R&D has
1228 been carried out, the production is financed. And furthermore it should become a fact
with one HL-LHC run in advance compared to ALICE-3, that is, HL-LHC run IV by
2027.

1230 2. B_z field “s” : the possibility to collect data under various B_z field intensities (3.8 T only ?
3.8 T and possibly lower intensities ?)¹¹.

1232 3. Spatial resolution : the spatial granularity driven by the TOF pad sizes, in barrel ($\Delta r\phi =$
57 mm \times $\Delta z = 3\text{ mm}^2$ for LYSO bar crystals, Fig. 2.60 in [8]) and endcap ($1.3 \times 1.3\text{ mm}^2$
1234 for LGAD, Sec. 3.2 in [8]).

1236 4. Occupancy : the sub-detector occupancy depending on the collision system and pile-up con-
ditions.

1238 5. $\mathcal{A}.\varepsilon$: the impact of the tracker material budget on $\mathcal{A}.\varepsilon$ to reach the TOF sub-detector for
the individual identifiable species.

1240 *6. Relative abundancies* : the differential production rate per event for each particle species
 1242 with respect to all others, making more or less favourable balance between signal and
 background. The issue may not be on π^\pm , K^\pm and p^\pm , but rather on light nuclei, naturally
 scarce and so, being more vulnerable in that respect.

1244 Among the undecided points above, mostly all of them could be addressed with dedicated full
 simulations, in order to judge better of the underlying difficulties and relevance. Such Monte
 Carlo studies will naturally be as many long-standing and detailed work that would need to
 1246 be carried out collectively, not necessarily by relying on CMS members' shoulders only but
 potentially led by the "heavy-ion" LHC community as a whole.

1248 In the meantime, as extra considerations, it will be valuable to keep in mind the characteristics
 of the Phase-2 CMS tracker [32] in place by the time of the HL-LHC run IV and later, occu-
 1250 pying the volume between the interaction point and the MTD. Figure 24 gives the experiment
 layout, how the barrel and endcap components are organised. Figure 25 specifies the expected
 1252 material budget distribution in X/X_0 as function of $|\eta|$. Figures Fig. 26(a) and (b) provides
 respectively an estimate of the fluence (in 1-MeV n_{eq}/cm^{-2}) and the total ionising dose TID
 1254 (in Gray, Gy) distributed over the tracker geometry.

¹¹ Running the CMS experiment under various B_z fields recovers several orthogonal or complementary aspects : the collaboration-wide interest and approval for such magnetic configurations, ability of the 3.8-T supraconducting magnet to sustain additional hysteresis cycles, the existence of accurate field maps per B_z configuration throughout the geometry of the experiment, steering of the LHC beams through the experiment under unusual B_z , tracking recommissioning adapted to new B_z , recommissioning of the calorimeter responses as well, overall data taking time allotted (hours, days, weeks ?) per B_z configuration and per collision system (pp, p-A, A-A).

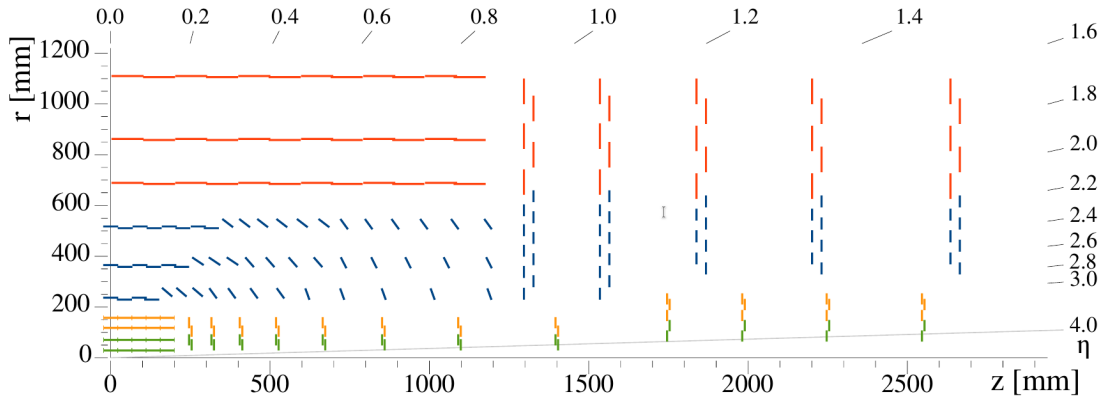


Fig. 24: CMS detector layout for the Phase-2 tracker, showing the barrel and endcap elements corresponding to Fig. 2.3 in [32]. Orange and green lines stands for the Inner Tracker (IT) consisting of pixel sensors, blue dashes and red segment define together the Outer Tracker (OT), with modules combining macro-pixels with micro-strips in blue (PS), and double-sided micro-strips in red (2S).

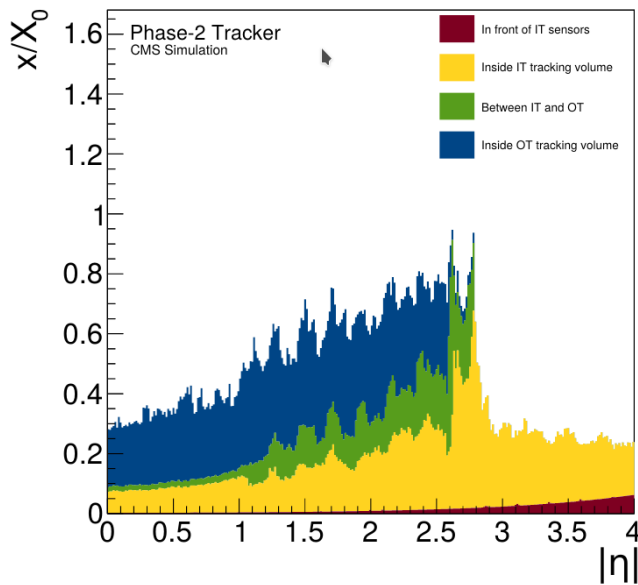


Fig. 25: CMS repartition of the radiation length as a function of $|\eta|$ corresponding to Fig. 6.2 in [32].

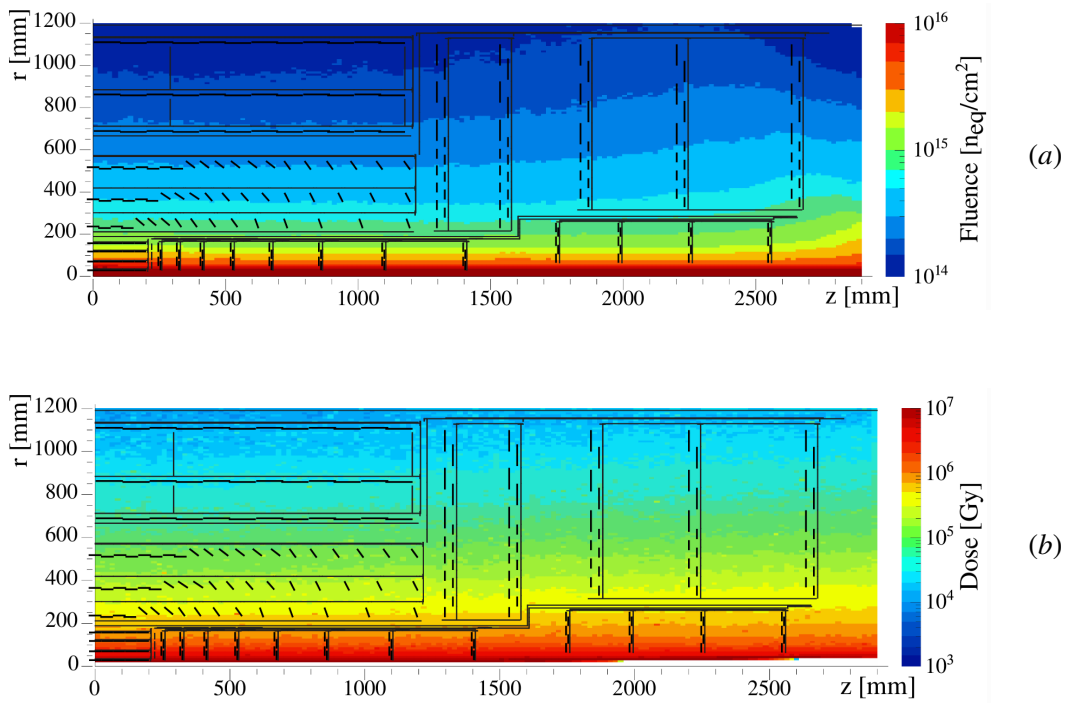


Fig. 26: CMS 2D maps for fluence (a) and total ionising dose (b) in the Phase-2 tracker detector, corresponding respectively to Figs. 2.2 and 8.3 in [32].

1256 IX TOF measurements in ATLAS (HL-LHC run IV and V)

1258 In a similar path followed by CMS, the ATLAS collaboration has also made the choice to set up a detector dedicated to pile-up tagging for HL-LHC run IV, the High Granularity Timing detector (HGTD). See the corresponding Technical Design Report [25].

1260 The peculiarity of this sub-detector is that it is only foreseen at forward and backward rapidities, as two endcap disks, covering $2.4 < |\eta| < 4.0$, based on LGAD architecture (as in the CMS case, with the same pad size of $1.3 \times 1.3 \text{ mm}^2$), occupying about 5-cm thickness, at distances $|z|$ between 3.435 m and 3.485 m, with a time resolution of 32 ps. The physics cases associated to TOF capabilities have not been discussed in the TDR but will certainly be a fact, as in the CMS case.

1266 In the work done here, performances of a HGTD configuration in the ATLAS default magnetic solenoidal field of 2.0 T is provided (Fig. 50, Fig. 52, Fig. 54 and Fig. 56). As proposed with the CMS configuration, a second configuration has been tested with a twice lower magnetic field, *i.e.* at 1.0 T here. (Fig. 51, Fig. 53, Fig. 55 and Fig. 57).

1270 The fact that, at the run IV horizon, the central rapidities will not be equipped with any timing detector opens the hypothesis of a future instrumentation at such a location, for instance, at the next milestone of Long Shutdown 4 (≈ 2030) before HL-LHC run V for a timeline similar to ALICE-3. To that end, two mid-rapidity configurations have been further added to the plots, considering a timing layer positioned either at a radius $R = 1.0 \text{ m}$ or at $R = 0.29 \text{ m}$.

The motivations of such chosen radii rely on a few prime considerations.

- 1276 (i) ITk layout illustrated in Fig. 27, taken from recent [33],
- (ii) ITk material budget estimated in Fig. 28, taken from the same note [33],
- 1278 (iii) ITk fluence and dose maps illustrated in Fig. 29, available from [34].

1280 If SPAD architecture were developed and ready for ALICE-3, with 1% x/X_0 per layer and radiation tolerance up to $\mathcal{O}(10^{15}) \text{ 1-MeV } n_{eq}/\text{cm}^{-2}$, why not imagining ATLAS using it as well in the middle of the tracking layers? – This calls for specific considerations about the radiation levels as a function of space and, looking at Fig. 29, the domain around $R = 0.29 \text{ m}$ or *a fortiori* around $R = 1.0 \text{ m}$ would match such an instrumentation idea.

1284 If the location would be defined, the next question to come concerns the zenithal angle coverage or the η coverage. Let's take a second look at the Fig. 27. At both radii, $R = 1.0 \text{ m}$ or $R = 0.29 \text{ m}$, it would be first accessible to cover $|\eta| < 1.0$. The corresponding foreseen layers at both radii in ITk must be constituted by simple cylindric geometries. Replacing such a given layer with one technology by another may be more manageable in terms of mechanics and integration.

Back to Fig. 27, what if one would now decide to enlarge the η coverage to ± 2.0 units? ...

- 1290 • at $R \approx 1.0 \text{ m}$, this would call for a revision of several endcap planes in addition to the previous layer, complexifying the enterprise and raising the associated costs;
- 1292 • at $R = 0.29 \text{ m}$, this would go with a modification in azimuth of all the tilted double-segments at the same radius (illustrated by the 9 red segments on the figure) in addition of the regular cylinder at mid-rapidity. The pros and cons would need to be discussed in details with experts but it is *a priori* not the most immediate sensor change to be integrated.

1296 A way out solving potentially the situation for both radii could be in fact to change only the outer endcap disk, appearing as blue vertical segment at $z = 1.5 \text{ m}$ in Fig. 27. Doing so, the pseudorapidity coverage from ≈ 1.0 to ≈ 2.2 would be assured by a single plane to be modified; this implies that this domain that is yet still at mid-rapidity would then be covered not by a cylindric *barrel* layer but by a vertical *endcap* disk.

1302 In a similar spirit to what has been discussed for ALICE-3, this would augur that the ultimate ATLAS TOF configuration could be hinged on the combination of four different TOF locations :

- 1304 (i) an outer barrel layer at $R_{\text{TOF}}^{\text{barrel}} = 1.0$ m, covering $|\eta| < 1.0$, based on MAPS,
 1306 (ii) an intermediate barrel layer at $R_{\text{TOF}}^{\text{barrel}} = 0.29$ m, covering $|\eta| < 1.0$, based on MAPS,
 1308 (iii) an close endcap disk at $Z_{\text{TOF}}^{\text{endcap}} = 1.50$ m, covering the range $1.1 < |\eta| < 2.2$, based on MAPS,
 (iv) a distant endcap disk embodied by the HGTD, located at $Z_{\text{TOF}}^{\text{endcap}} = 3.45$ m, spanning $2.4 < |\eta| < 4.0$, based on LGAD architecture.

1310 In any of the aforementioned ATLAS cases, the minimal inclination angle in barrel has been set to a value $\delta > 30^\circ$, for any vertical endcap planes, to $\lambda > 30^\circ$.

1312 As for The TOF PID competitiveness of ATLAS with respect to ALICE-3 and CMS, the same comments stressed in previous CMS section IX can be stressed again here.

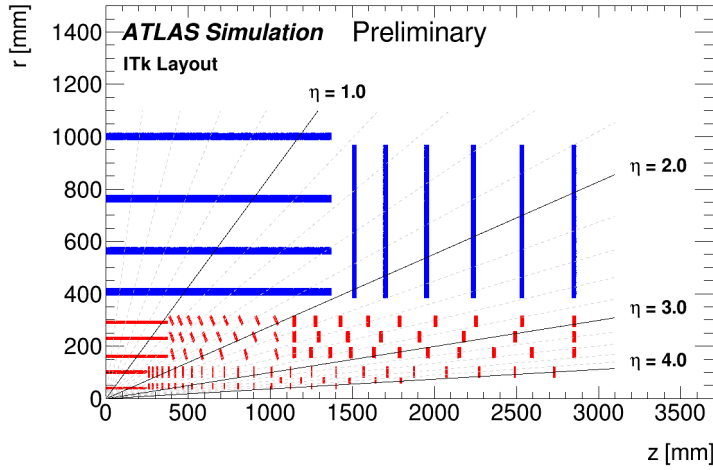


Fig. 27: Layout of the ATLAS tracker ITk corresponding to Fig. 1 in [33].

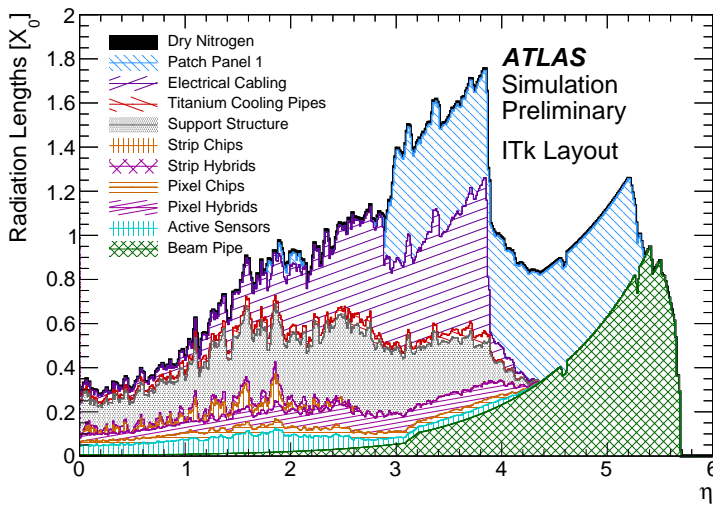


Fig. 28: Repartition of the material budget (in x/X_0) for the ATLAS tracker ITk corresponding to Fig. 3 in [33].

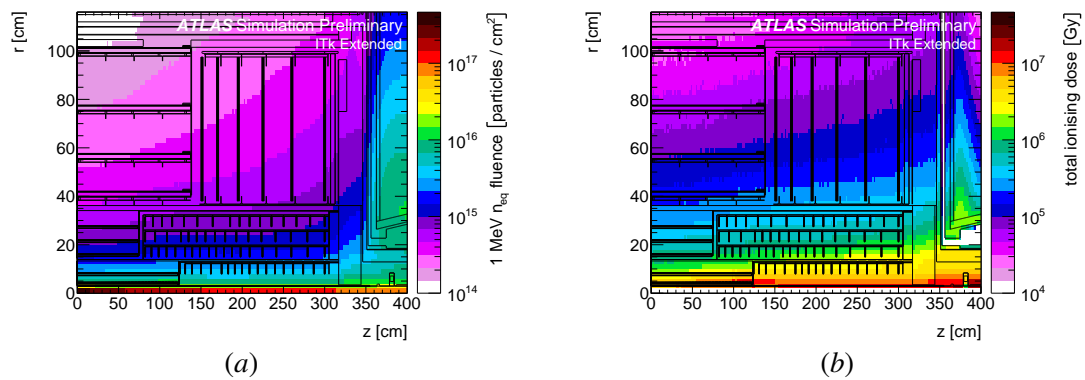


Fig. 29: ATLAS 2D maps for fluence (a) and total ionising dose (b) in the ITk detector taken from [34].

1314 **ALICE-3** configurations

Fig. 30: Expected TOF performances in terms of particle separations as a function of p_T and y for the configuration already foreseen or possibly anticipated for the [ALICE-3](#) experiment, with hypotheses :
i) $\langle r_{TOF}^{barrel} \rangle = 1.00$ m, *ii)* $\langle z_{TOF}^{endcap} \rangle = 2.00$ m, *iii)* TOF timing resolution = 10 ps, *iv)* $B_{field} = -0.2$ T.

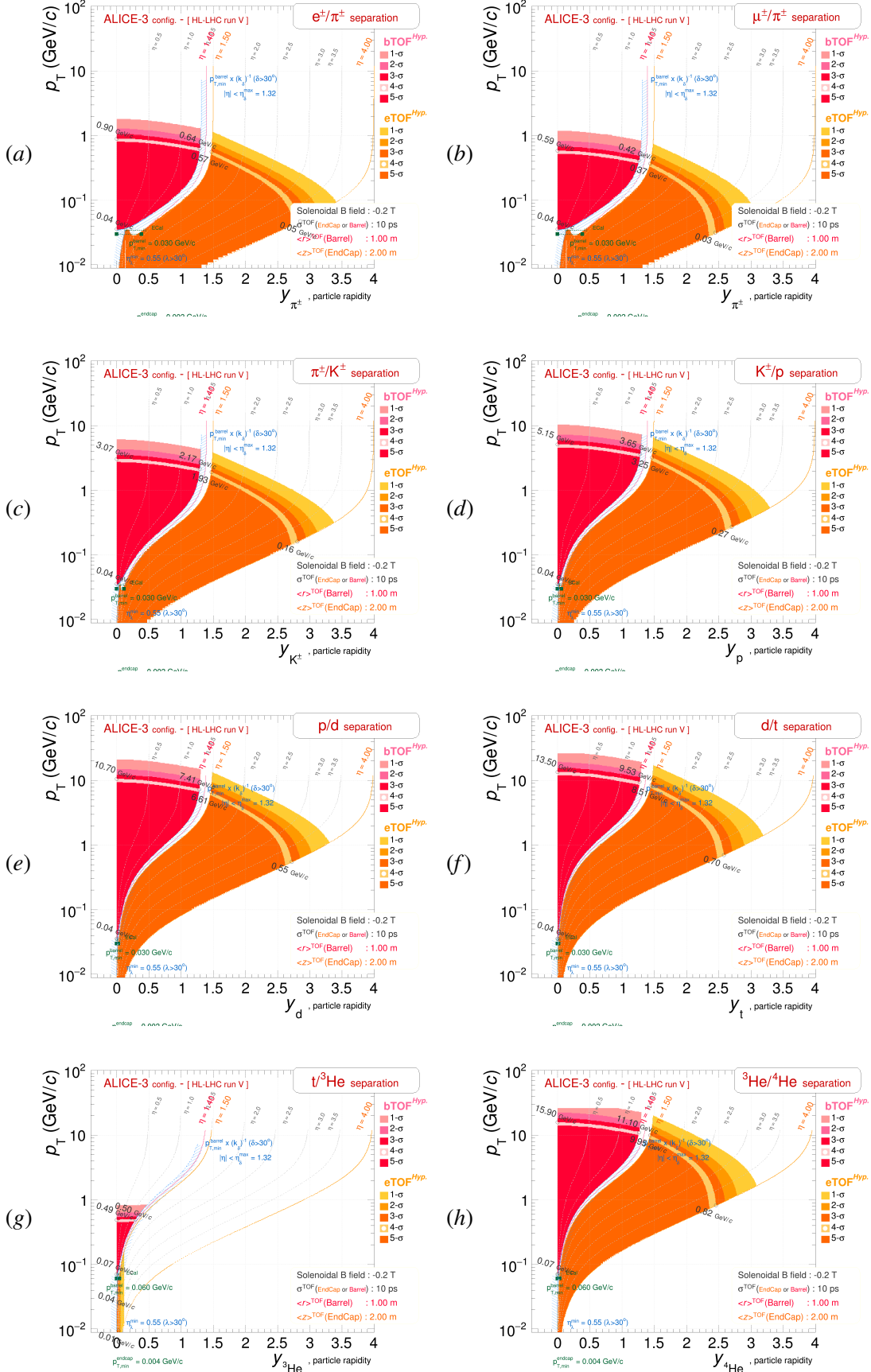


Fig. 31: Expected TOF performances in terms of particle separations as a function of p_T and y for the configuration already foreseen or possibly anticipated for the **ALICE-3** experiment, with hypotheses :
 i) $\langle r_{TOF}^{barrel} \rangle = 1.00$ m, ii) $\langle z_{TOF}^{endcap} \rangle = 2.00$ m, iii) TOF timing resolution = 10 ps, iv) $B_{field} = -0.5$ T.

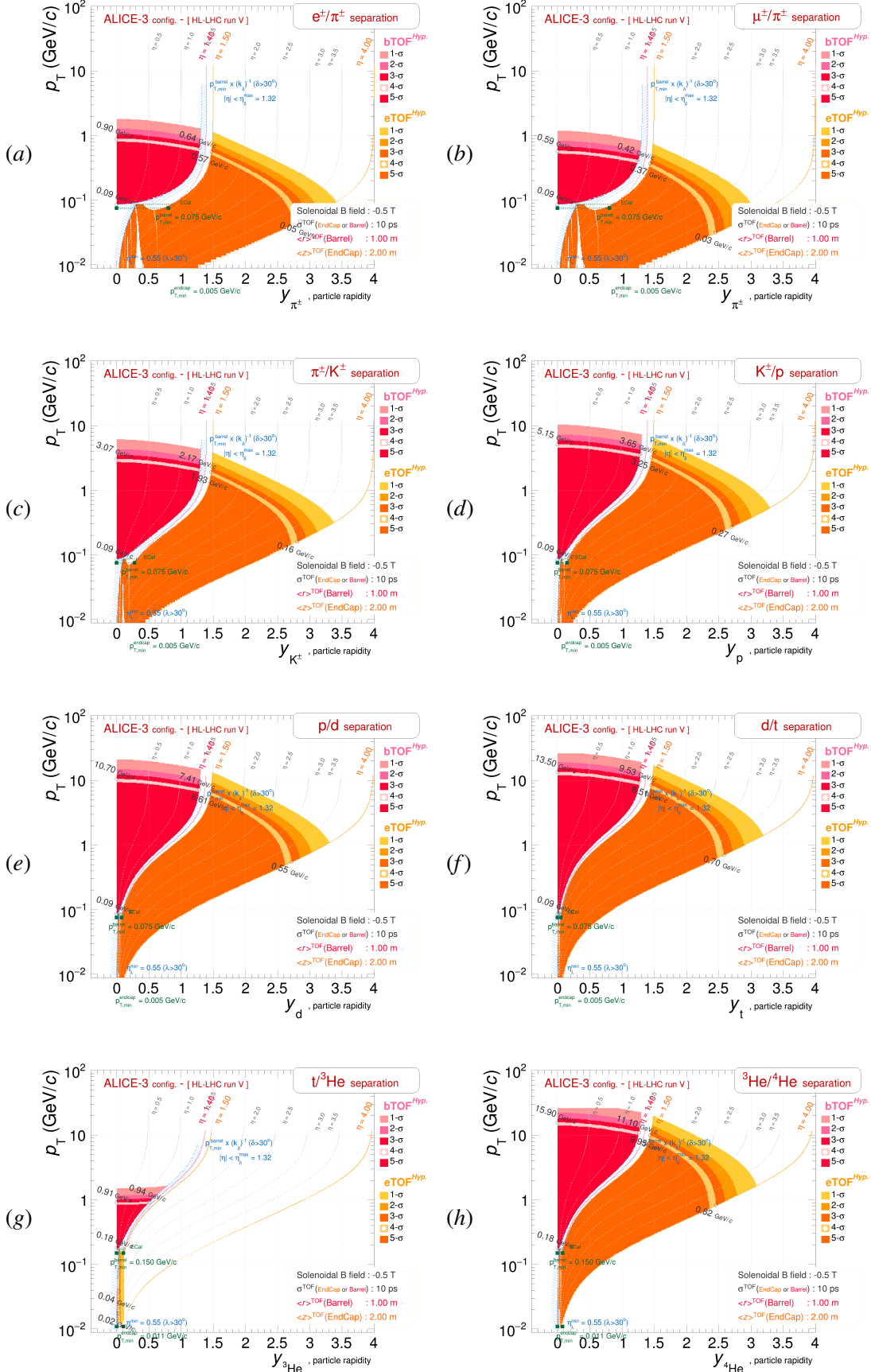


Fig. 32: Expected TOF performances in terms of particle separations as a function of p_T and y for the configuration already foreseen or possibly anticipated for the [ALICE-3](#) experiment, with hypotheses :
 i) $\langle r_{TOF}^{barrel} \rangle = 1.00$ m, ii) $\langle z_{TOF}^{endcap} \rangle = 2.00$ m, iii) TOF timing resolution = 10 ps, iv) $B_{field} = -1.0$ T.

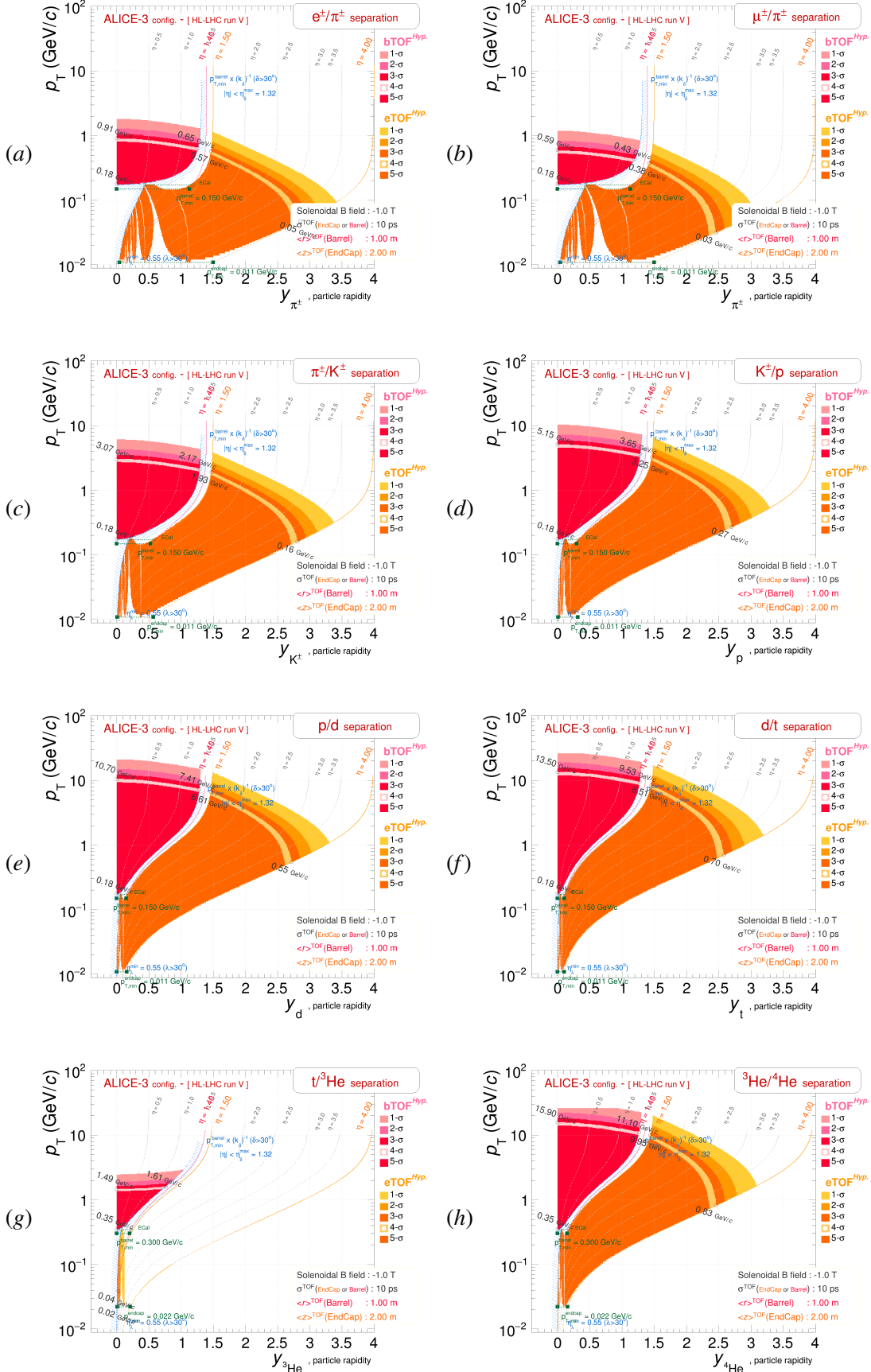


Fig. 33: Expected TOF performances in terms of particle separations as a function of p_T and y for the configuration already foreseen or possibly anticipated for the [ALICE-3](#) experiment, with hypotheses :
 i) $\langle r_{TOF}^{barrel} \rangle = 1.00$ m, ii) $\langle z_{TOF}^{endcap} \rangle = 2.00$ m, iii) TOF timing resolution = 20 ps, iv) $B_{field} = -0.2$ T.

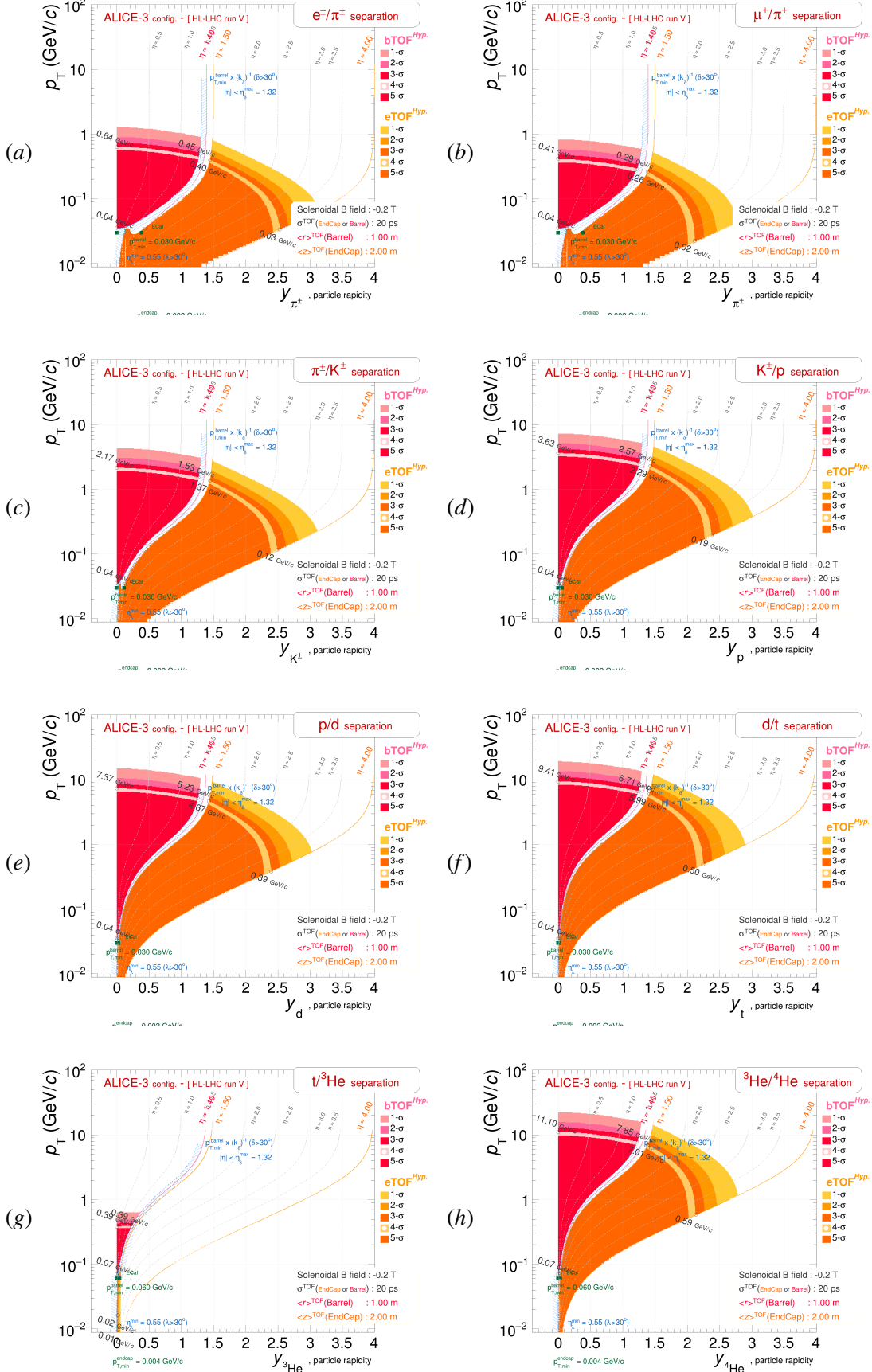


Fig. 34: Expected TOF performances in terms of particle separations as a function of p_T and y for the configuration already foreseen or possibly anticipated for the [ALICE-3](#) experiment, with hypotheses :
i) $\langle r_{TOF}^{barrel} \rangle = 1.00$ m, *ii)* $\langle z_{TOF}^{endcap} \rangle = 2.00$ m, *iii)* TOF timing resolution = 20 ps, *iv)* $B_{field} = -0.5$ T.

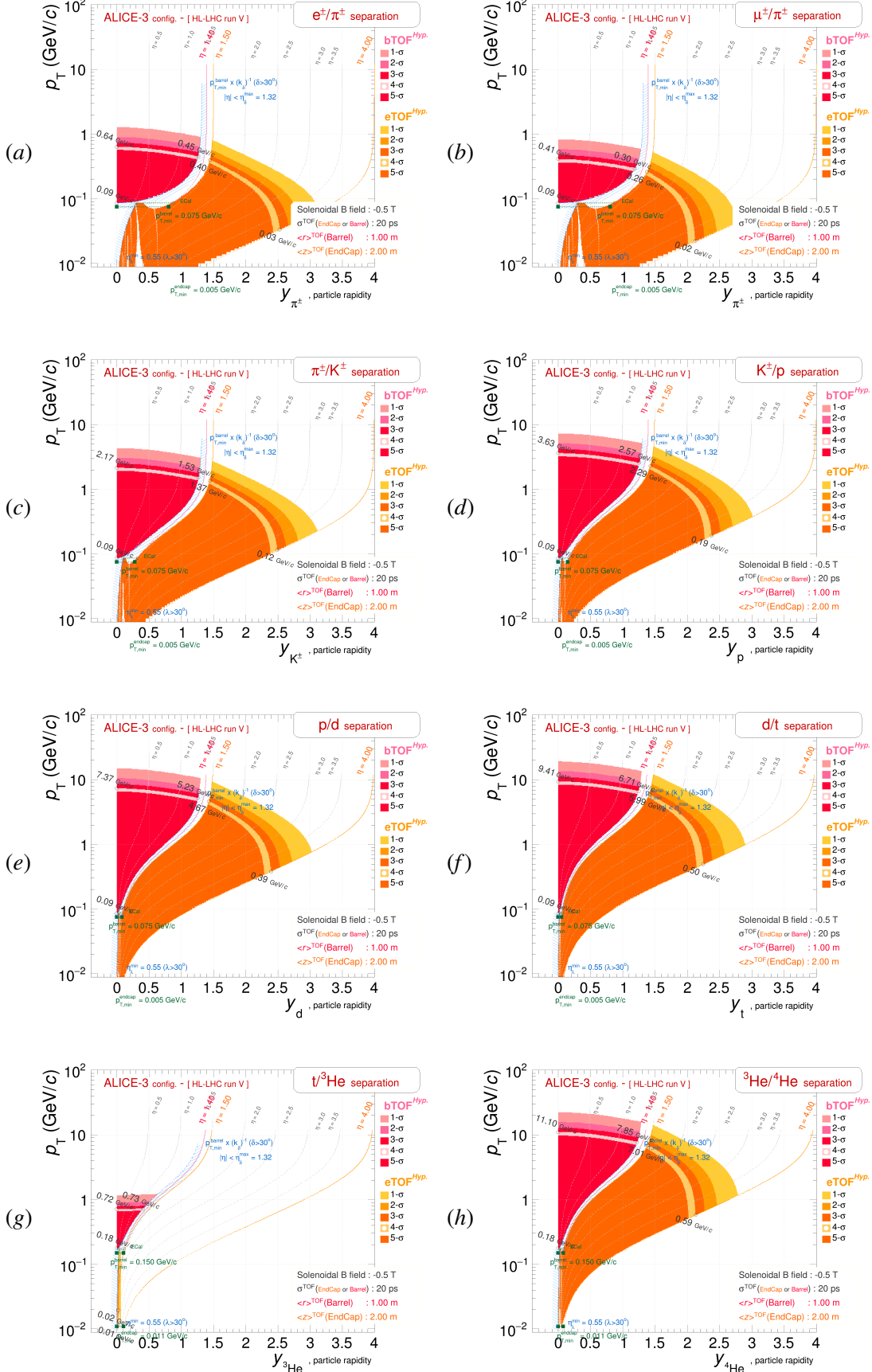


Fig. 35: Expected TOF performances in terms of particle separations as a function of p_T and y for the configuration already foreseen or possibly anticipated for the [ALICE-3](#) experiment, with hypotheses :
 i) $\langle r_{TOF}^{barrel} \rangle = 1.00$ m, ii) $\langle z_{TOF}^{endcap} \rangle = 2.00$ m, iii) TOF timing resolution = 20 ps, iv) $B_{field} = -1.0$ T.

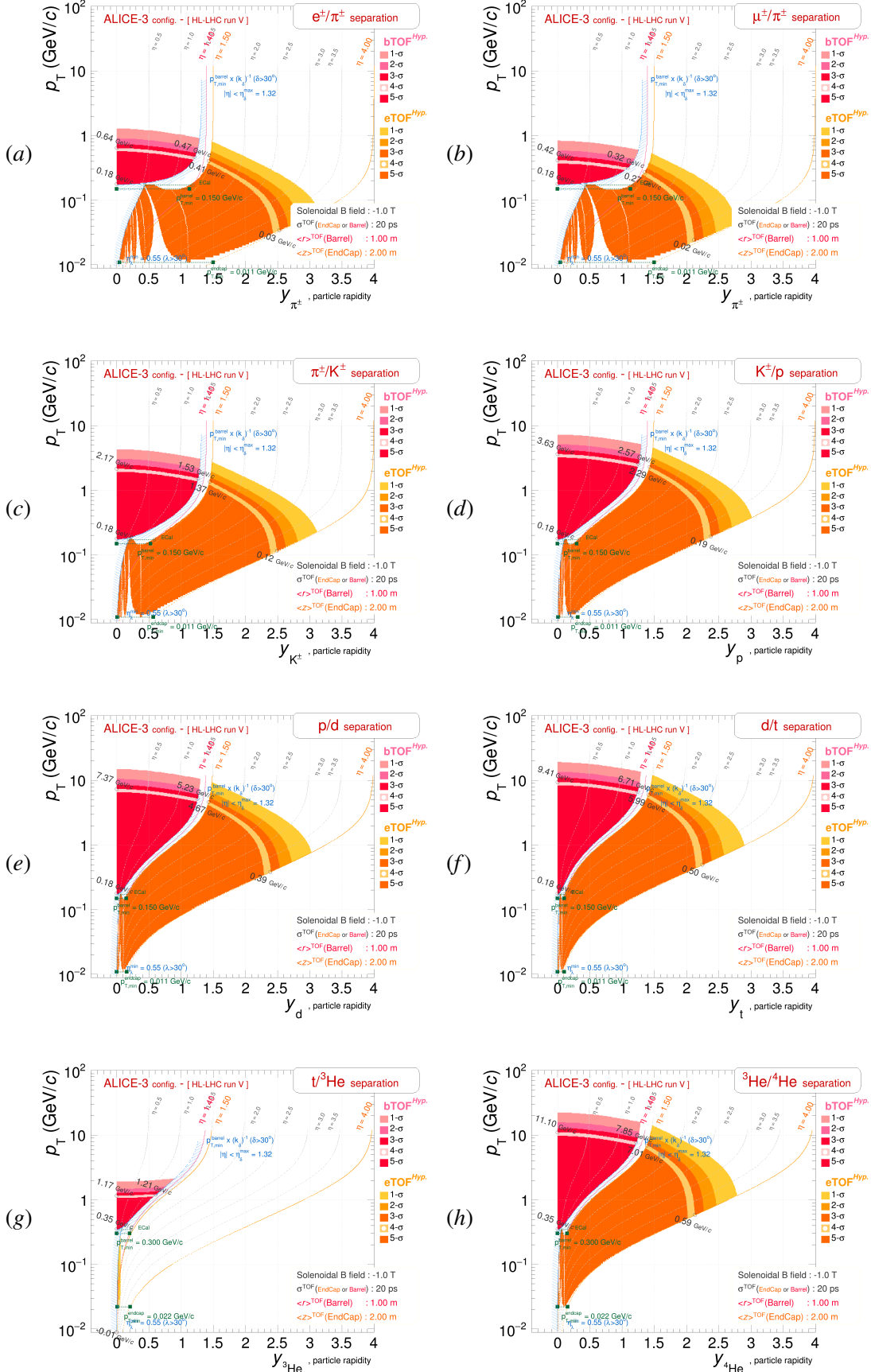


Fig. 36: Expected TOF performances in terms of particle separations as a function of p_T and y for the configuration already foreseen or possibly anticipated for the **ALICE-3** experiment, with hypotheses :
 i) $\langle r_{TOF}^{barrel} \rangle = 1.00$ m, ii) $\langle z_{TOF}^{endcap} \rangle = 2.00$ m, iii) TOF timing resolution = 30 ps, iv) $B_{field} = -0.2$ T.

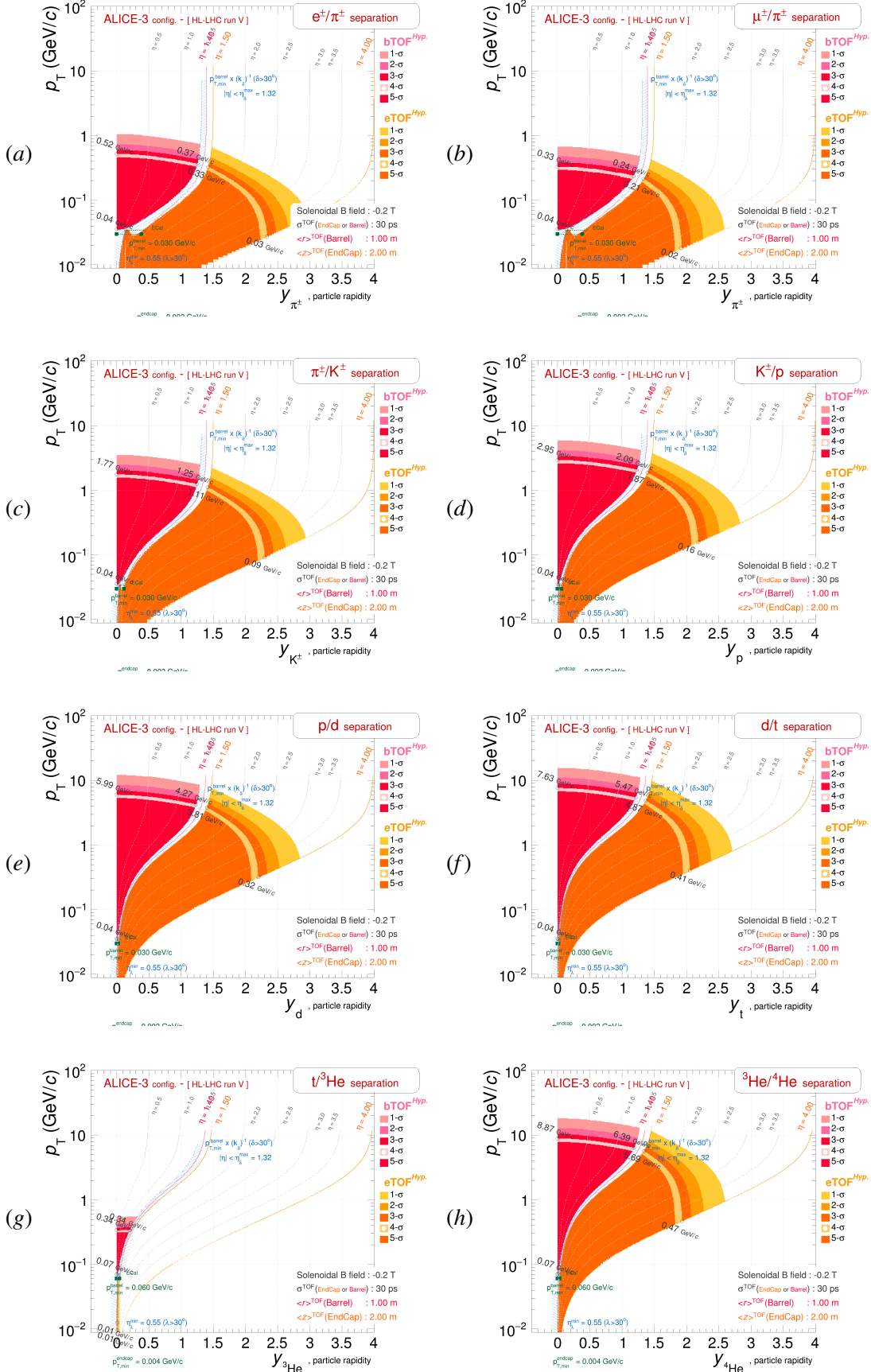


Fig. 37: Expected TOF performances in terms of particle separations as a function of p_T and y for the configuration already foreseen or possibly anticipated for the **ALICE-3** experiment, with hypotheses :
 i) $\langle r_{TOF}^{barrel} \rangle = 1.00$ m, ii) $\langle z_{TOF}^{endcap} \rangle = 2.00$ m, iii) TOF timing resolution = 30 ps, iv) $B_{field} = -0.5$ T.

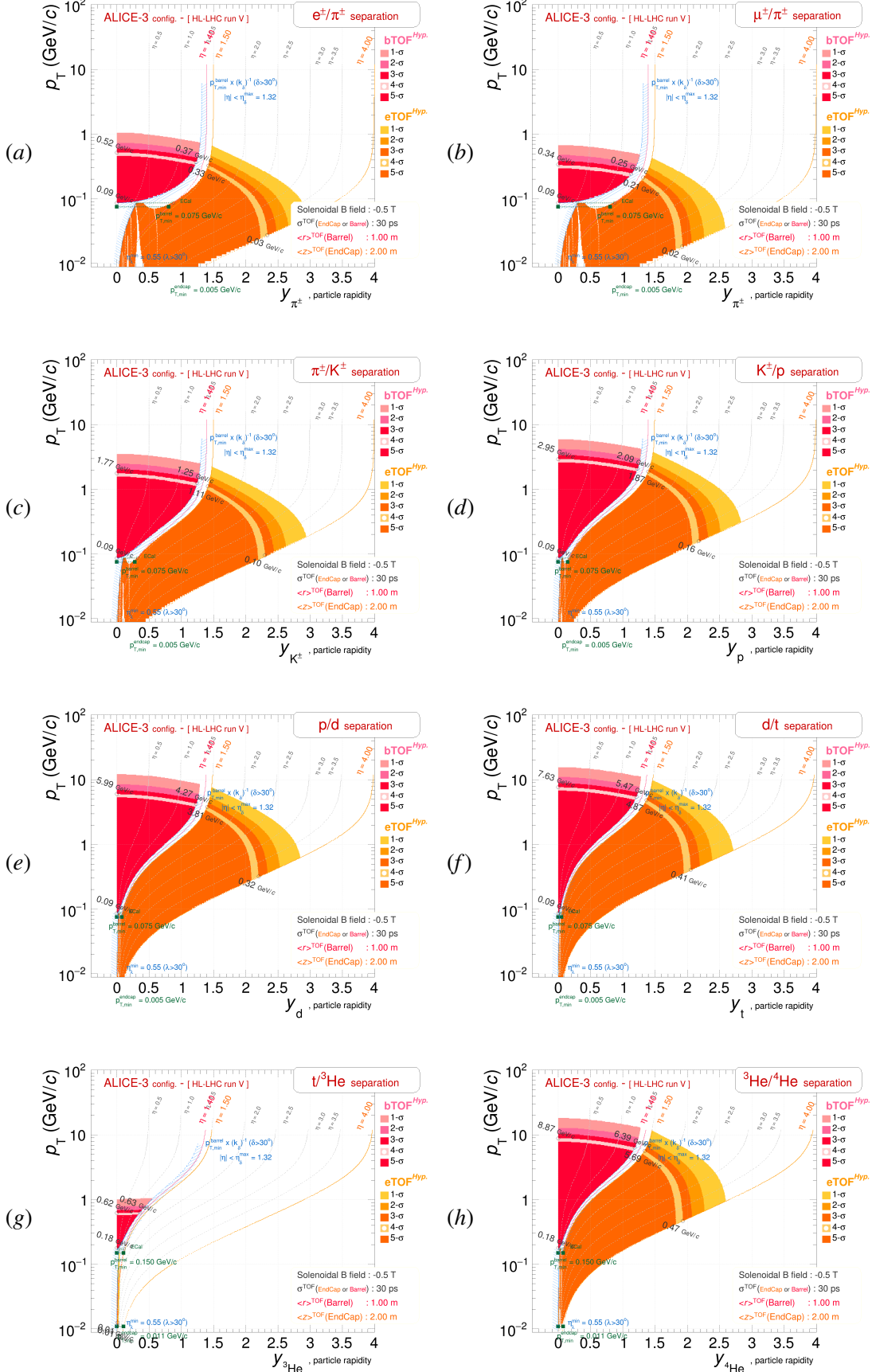


Fig. 38: Expected TOF performances in terms of particle separations as a function of p_T and y for the configuration already foreseen or possibly anticipated for the [ALICE-3](#) experiment, with hypotheses :
 i) $\langle r_{TOF}^{barrel} \rangle = 1.00$ m, ii) $\langle z_{TOF}^{endcap} \rangle = 2.00$ m, iii) TOF timing resolution = 30 ps, iv) $B_{field} = -1.0$ T.

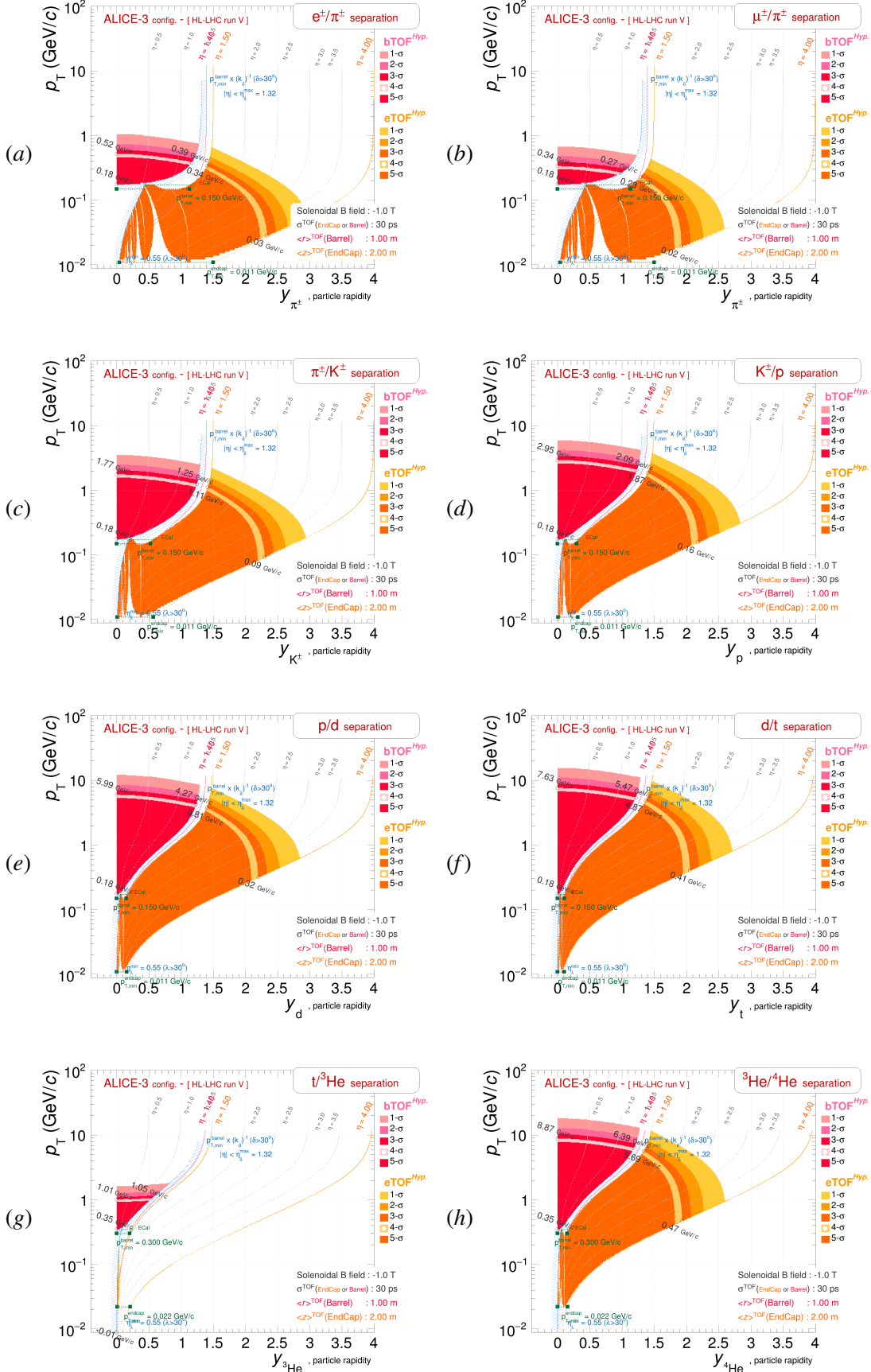


Fig. 39: Expected TOF performances in terms of particle separations as a function of p_T and y for the configuration already foreseen or possibly anticipated for the [ALICE-3](#) experiment, with hypotheses :
i) $\langle r_{TOF}^{barrel} \rangle = 0.20$ m, *ii)* $\langle z_{TOF}^{endcap} \rangle = 2.00$ m, *iii)* TOF timing resolution = 10 ps, *iv)* $B_{field} = -0.2$ T.

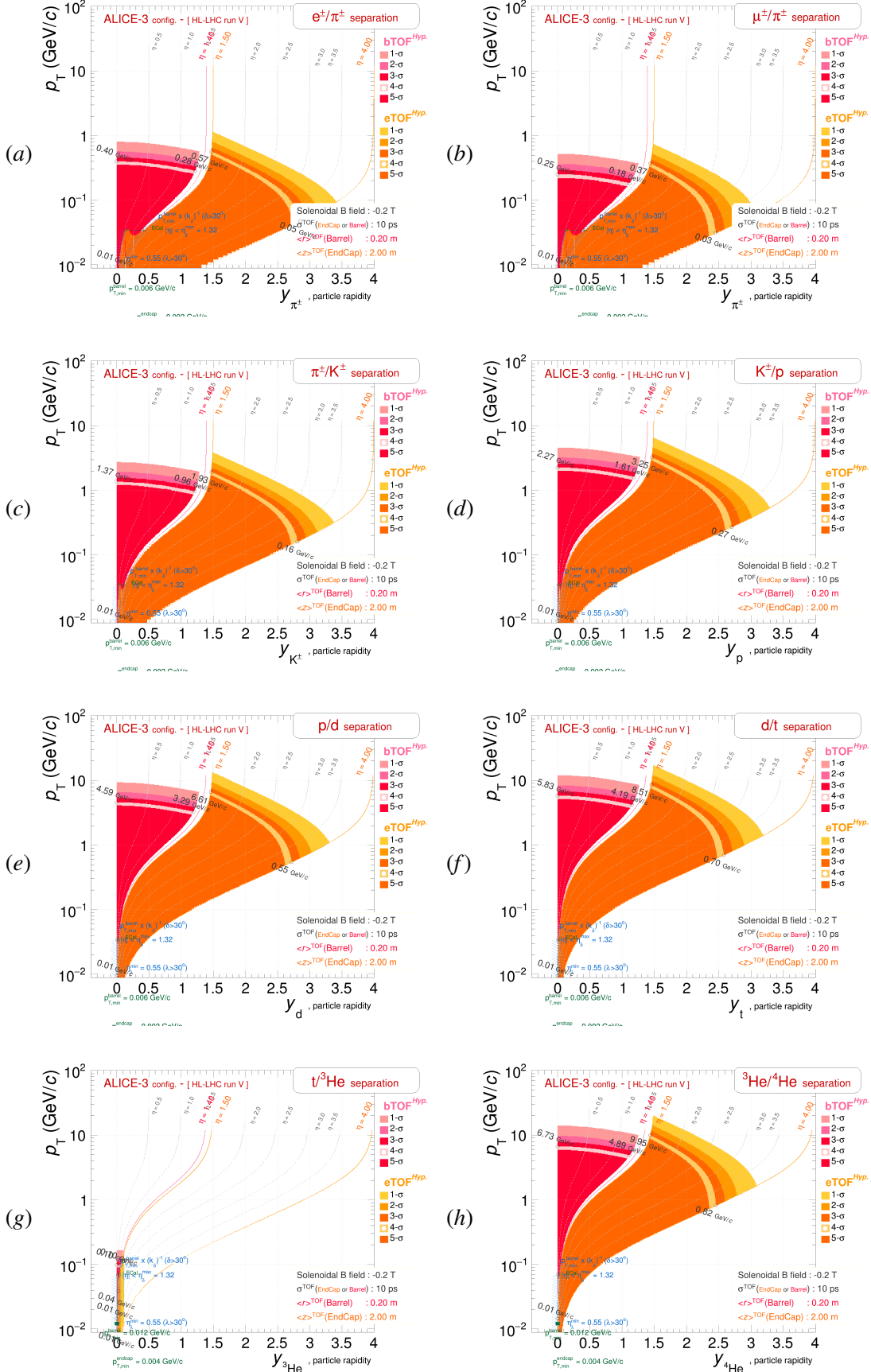


Fig. 40: Expected TOF performances in terms of particle separations as a function of p_T and y for the configuration already foreseen or possibly anticipated for the [ALICE-3](#) experiment, with hypotheses :
i) $\langle r_{TOF}^{barrel} \rangle = 0.20$ m, *ii)* $\langle z_{TOF}^{endcap} \rangle = 2.00$ m, *iii)* TOF timing resolution = 10 ps, *iv)* $B_{field} = -0.5$ T.

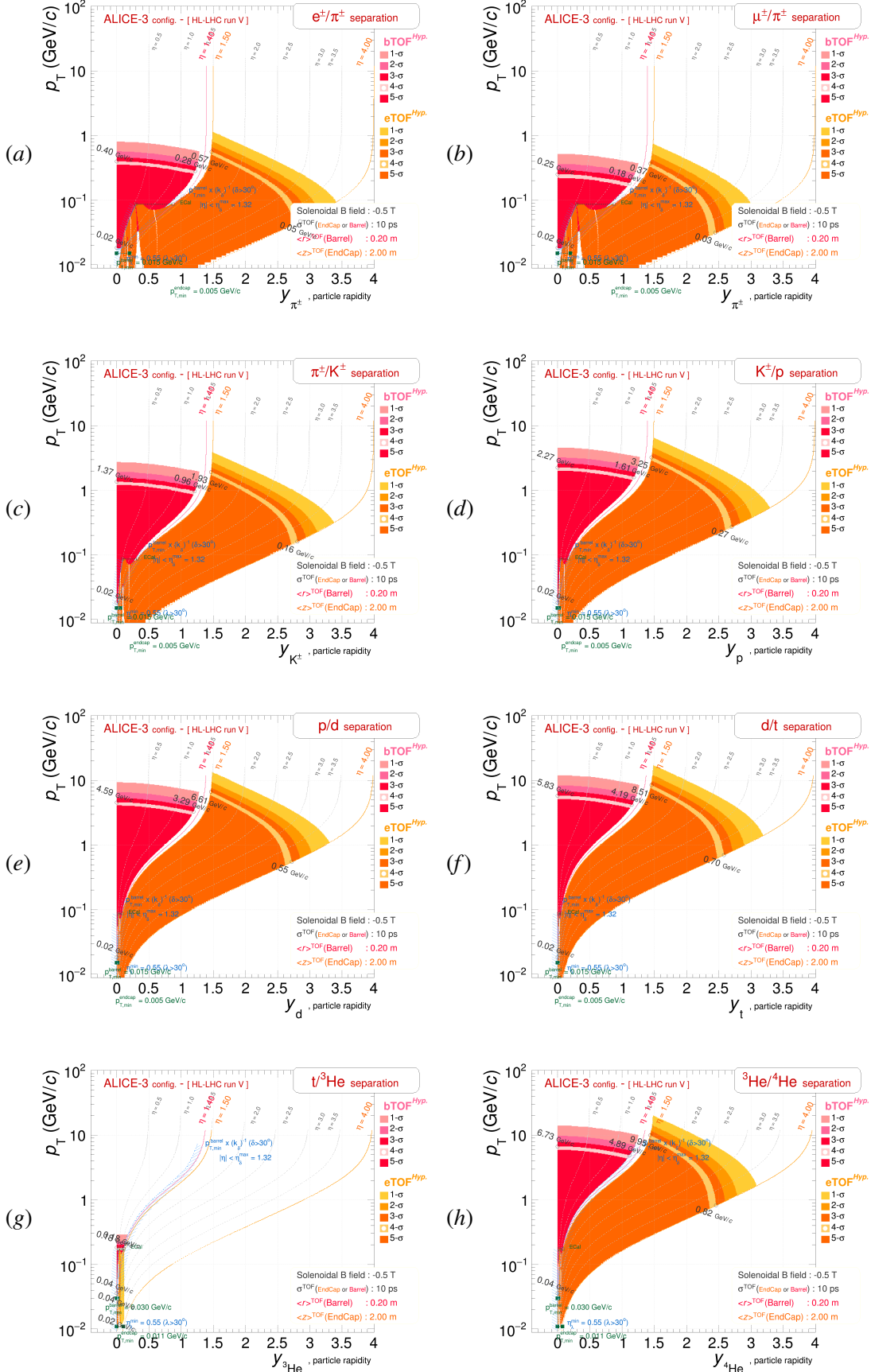


Fig. 41: Expected TOF performances in terms of particle separations as a function of p_T and y for the configuration already foreseen or possibly anticipated for the [ALICE-3](#) experiment, with hypotheses :
 i) $\langle r_{TOF}^{barrel} \rangle = 0.20$ m, ii) $\langle z_{TOF}^{endcap} \rangle = 2.00$ m, iii) TOF timing resolution = 10 ps, iv) $B_{field} = -1.0$ T.

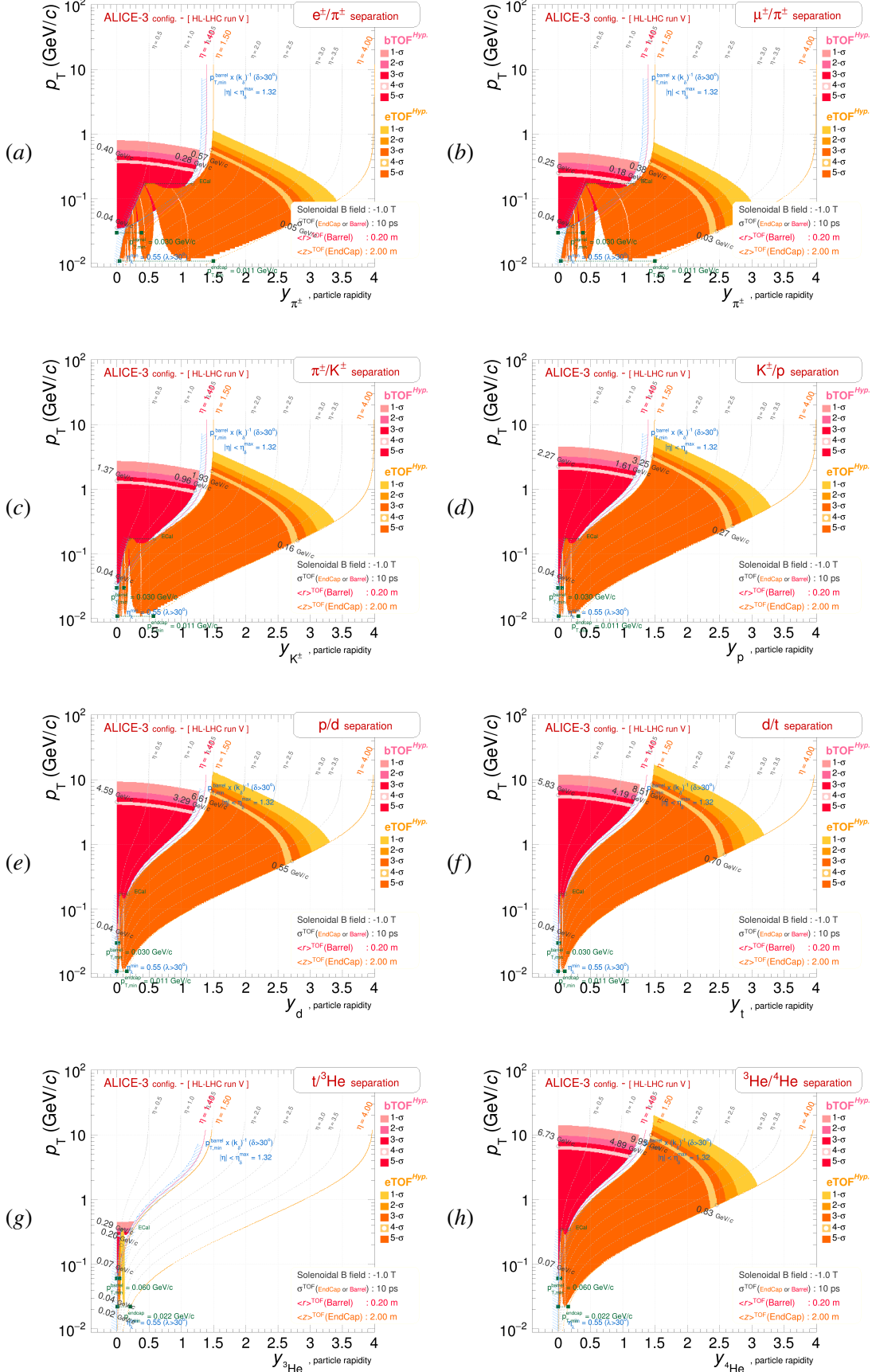


Fig. 42: Expected TOF performances in terms of particle separations as a function of p_T and y for the configuration already foreseen or possibly anticipated for the [ALICE-3](#) experiment, with hypotheses :
i) $\langle r_{TOF}^{barrel} \rangle = 0.20$ m, *ii)* $\langle z_{TOF}^{endcap} \rangle = 2.00$ m, *iii)* TOF timing resolution = 20 ps, *iv)* $B_{field} = -0.2$ T.

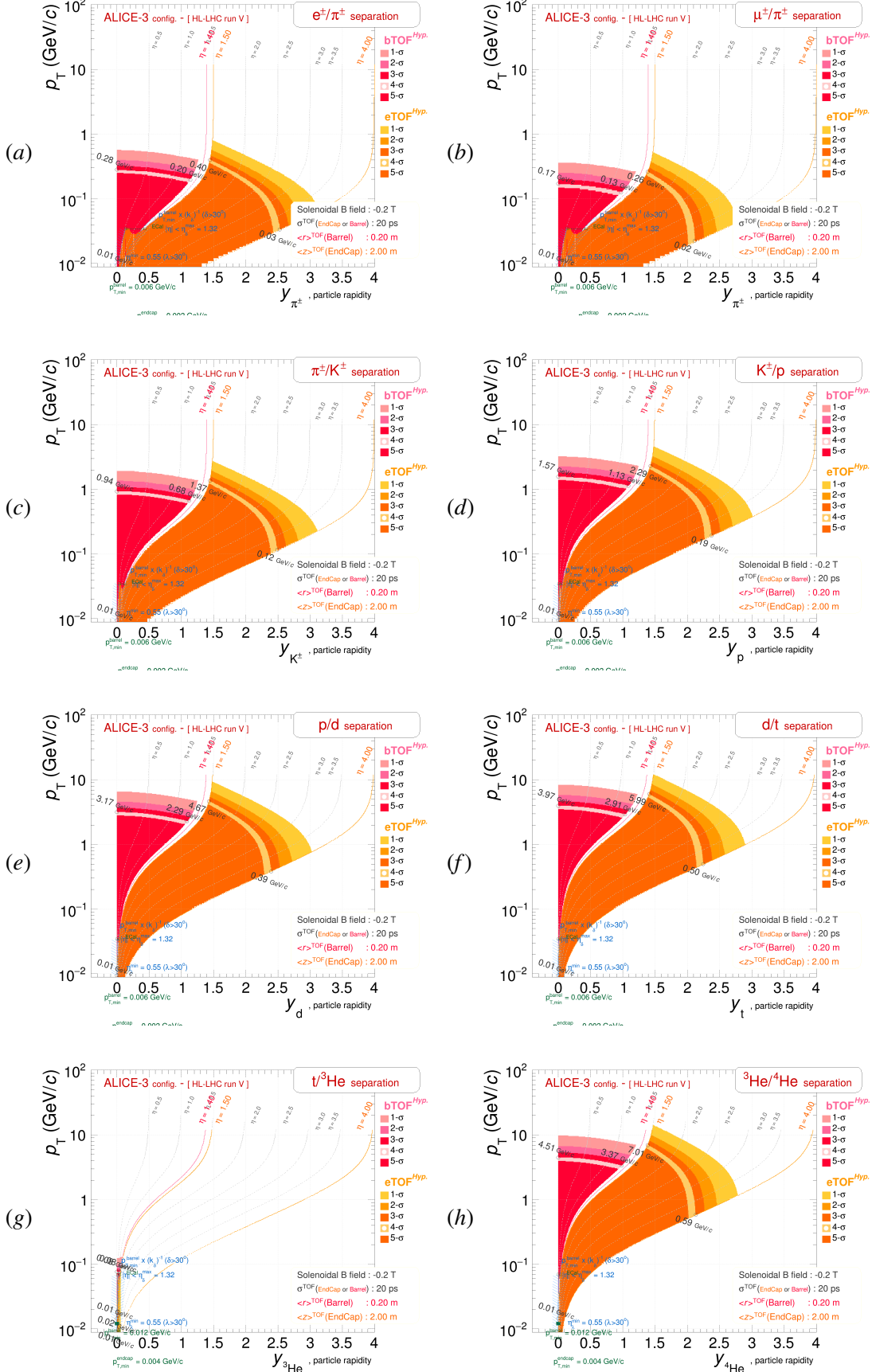


Fig. 43: Expected TOF performances in terms of particle separations as a function of p_T and y for the configuration already foreseen or possibly anticipated for the **ALICE-3** experiment, with hypotheses :
 i) $\langle r_{TOF}^{barrel} \rangle = 0.20$ m, ii) $\langle z_{TOF}^{endcap} \rangle = 2.00$ m, iii) TOF timing resolution = 20 ps, iv) $B_{field} = -0.5$ T.

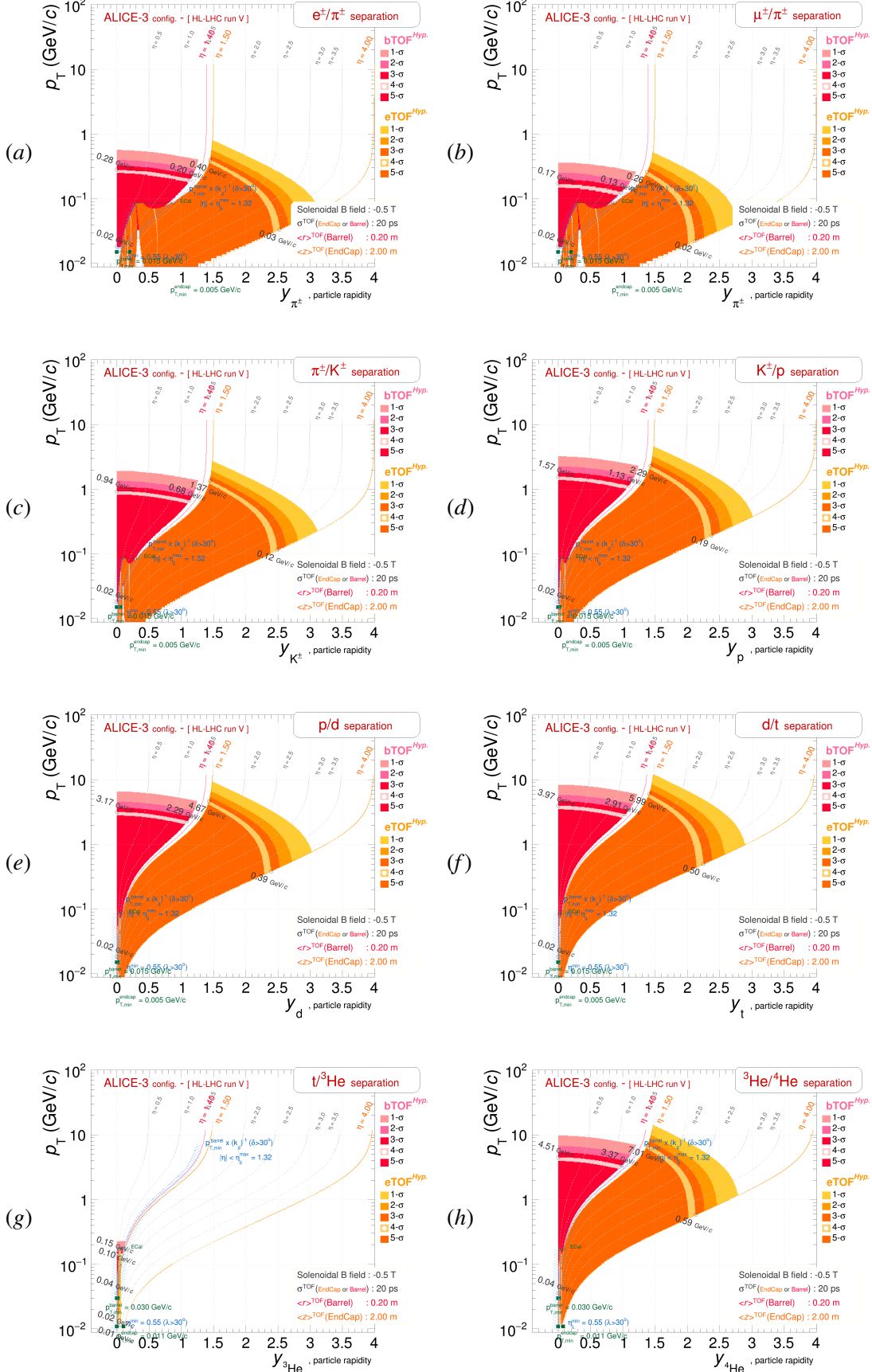


Fig. 45: Expected TOF performances in terms of particle separations as a function of p_T and y for the configuration already foreseen or possibly anticipated for the [ALICE-3](#) experiment, with hypotheses :
 i) $\langle r_{TOF}^{barrel} \rangle = 0.20$ m, ii) $\langle z_{TOF}^{endcap} \rangle = 2.00$ m, iii) TOF timing resolution = 30 ps, iv) $B_{field} = -0.2$ T.

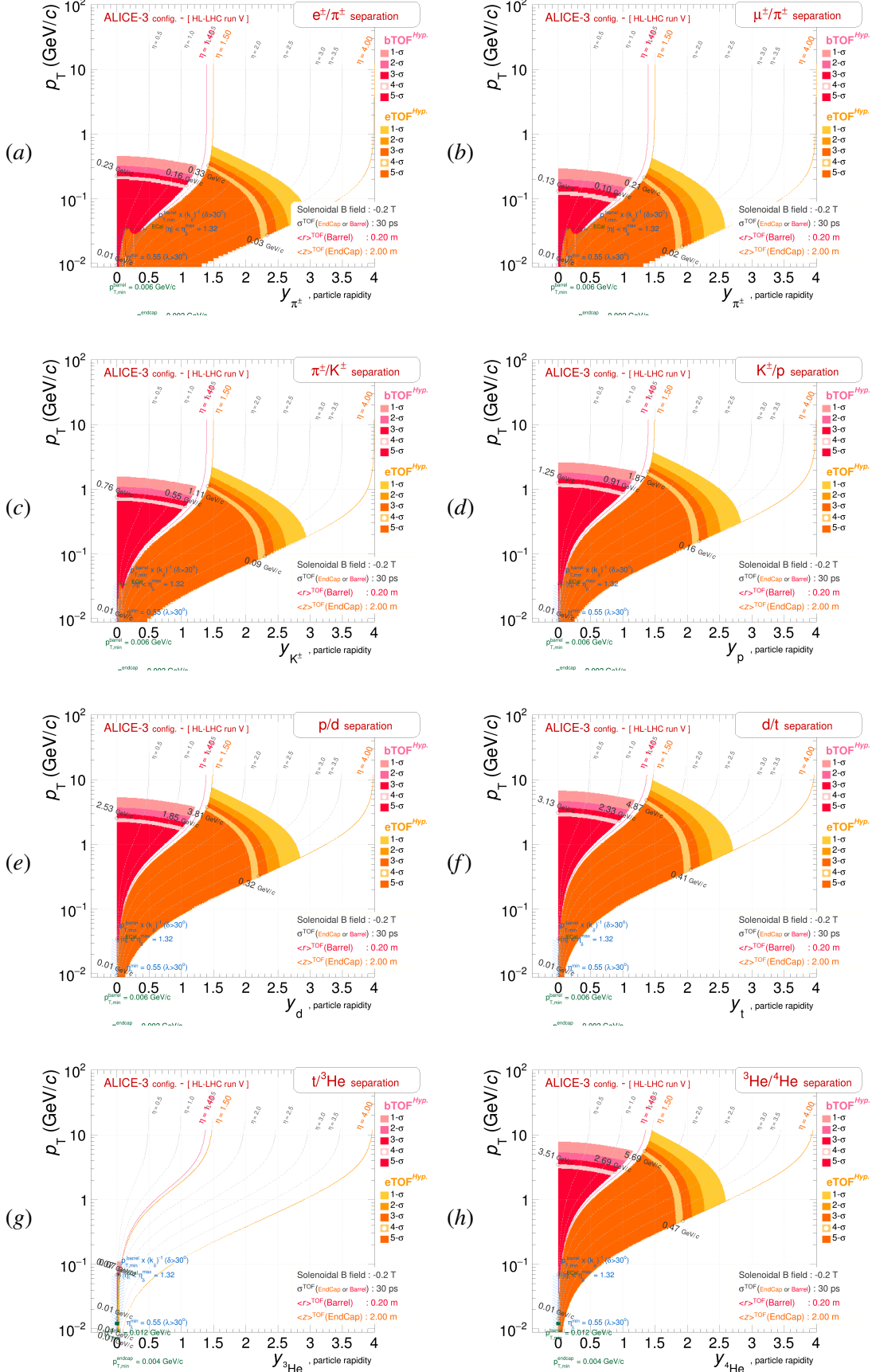


Fig. 46: Expected TOF performances in terms of particle separations as a function of p_T and y for the configuration already foreseen or possibly anticipated for the [ALICE-3](#) experiment, with hypotheses :
 i) $\langle r_{TOF}^{barrel} \rangle = 0.20$ m, ii) $\langle z_{TOF}^{endcap} \rangle = 2.00$ m, iii) TOF timing resolution = 30 ps, iv) $B_{field} = -0.5$ T.

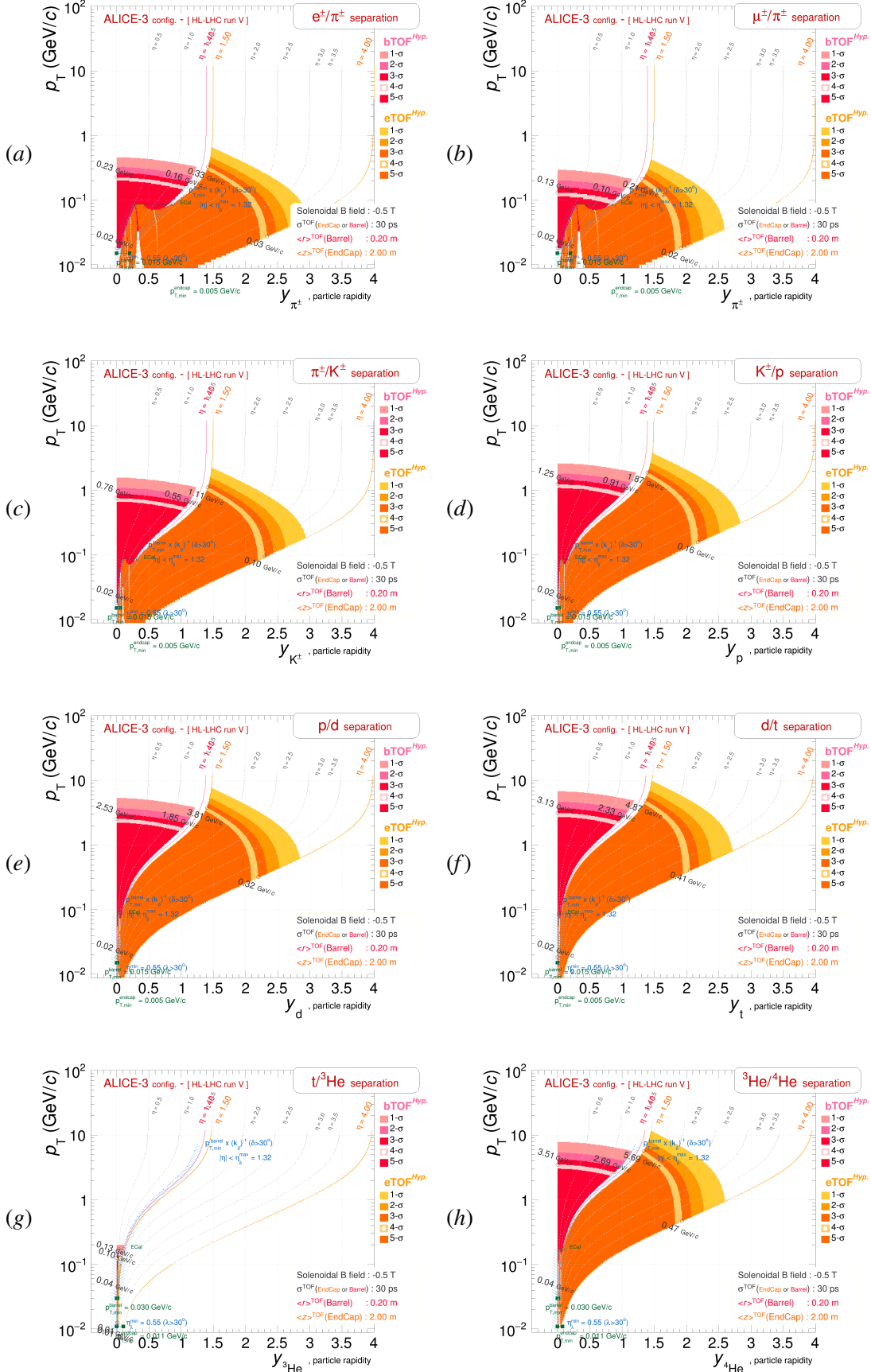
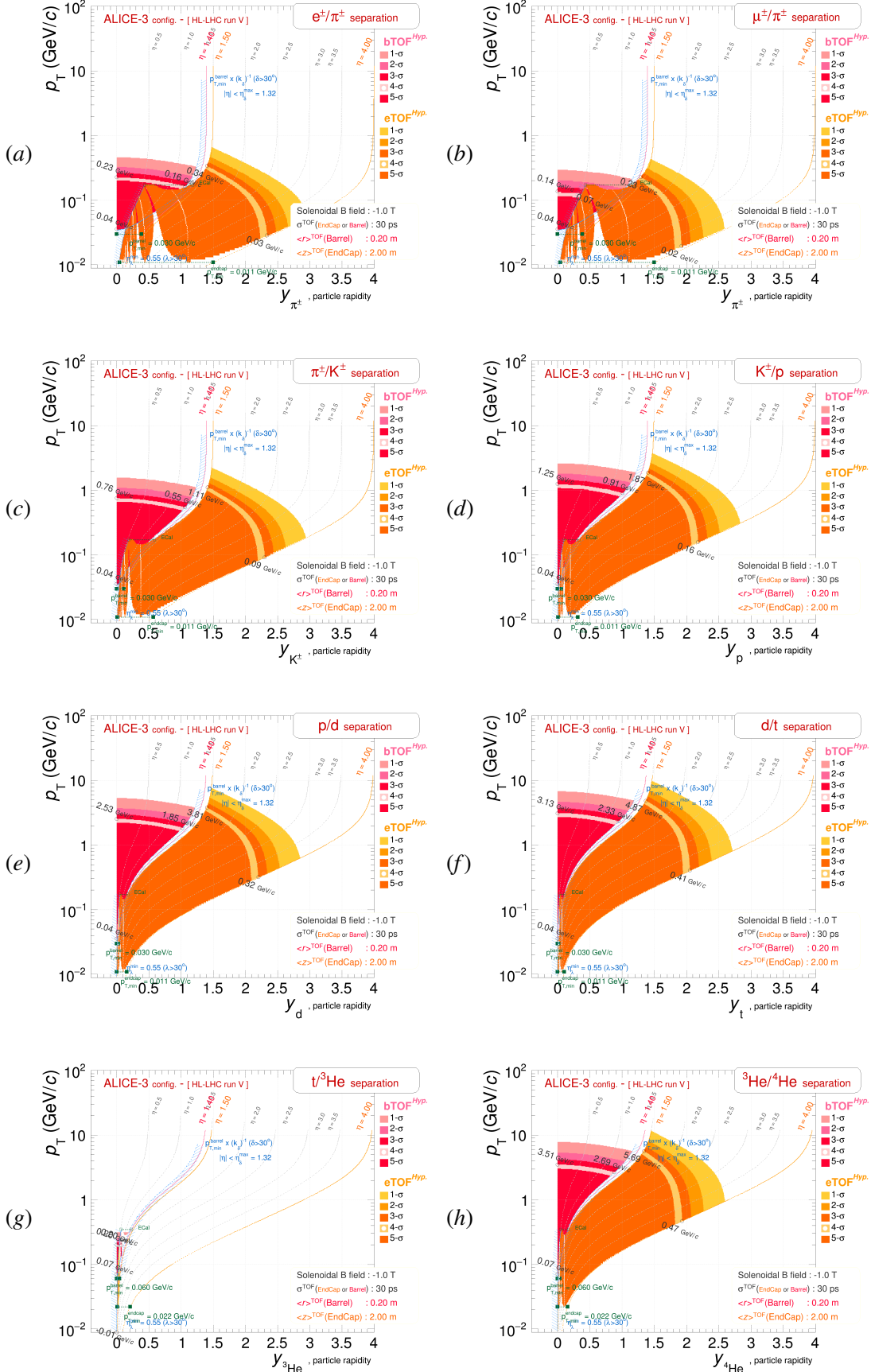


Fig. 47: Expected TOF performances in terms of particle separations as a function of p_T and y for the configuration already foreseen or possibly anticipated for the [ALICE-3](#) experiment, with hypotheses :
 i) $\langle r_{TOF}^{barrel} \rangle = 0.20$ m, ii) $\langle z_{TOF}^{endcap} \rangle = 2.00$ m, iii) TOF timing resolution = 30 ps, iv) $B_{field} = -1.0$ T.



CMS configurations

Fig. 48: Expected TOF performances in terms of particle separations as a function of p_T and y for the configuration already foreseen or possibly anticipated for the **CMS** experiment, with hypotheses :

- i) $\langle r_{TOF}^{barrel} \rangle = 1.16$ m, ii) $\langle z_{TOF}^{endcap} \rangle = 3.04$ m, iii) TOF timing resolution = 30 ps, iv) $B_{field} = -3.8$ T.

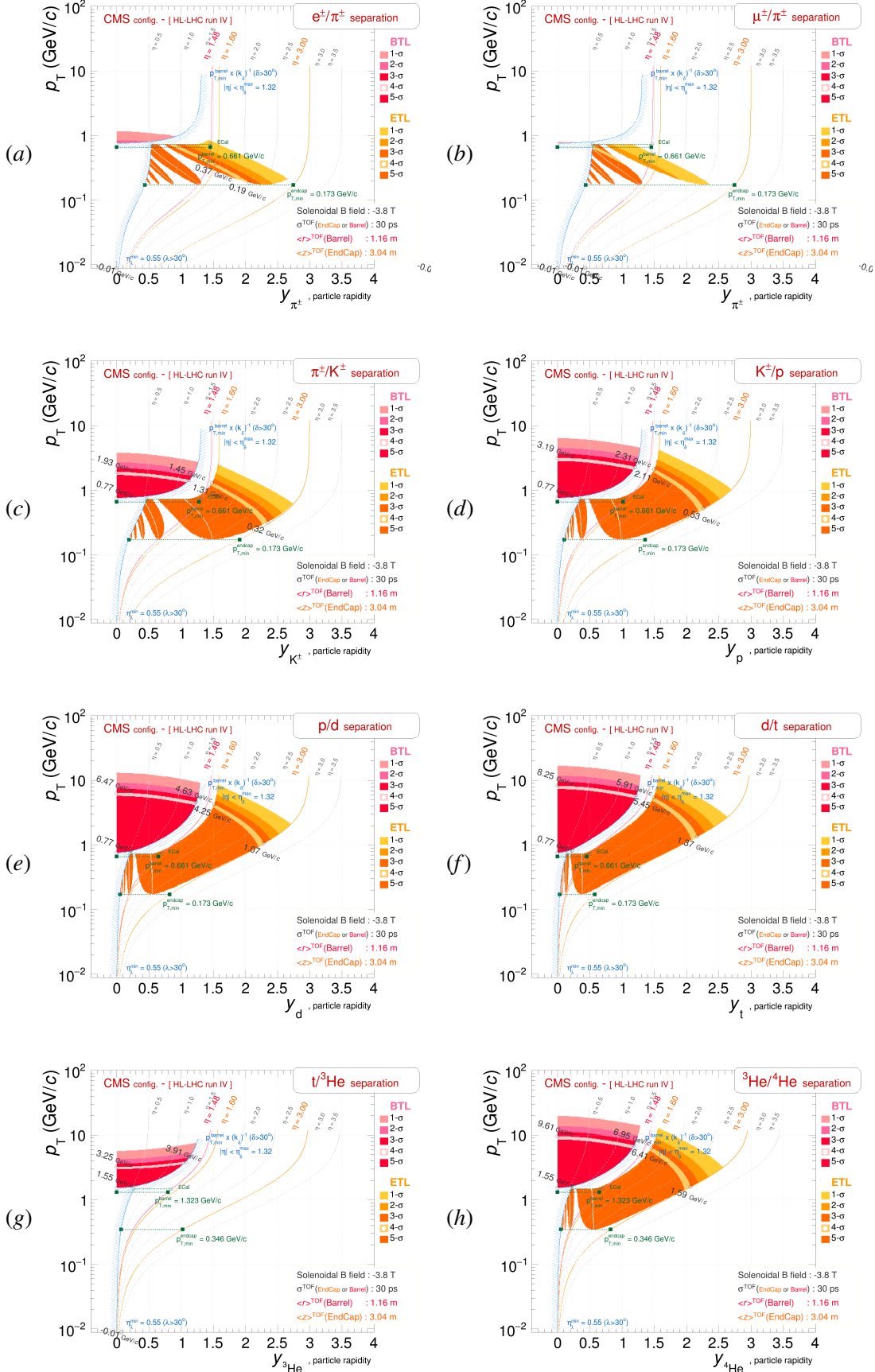
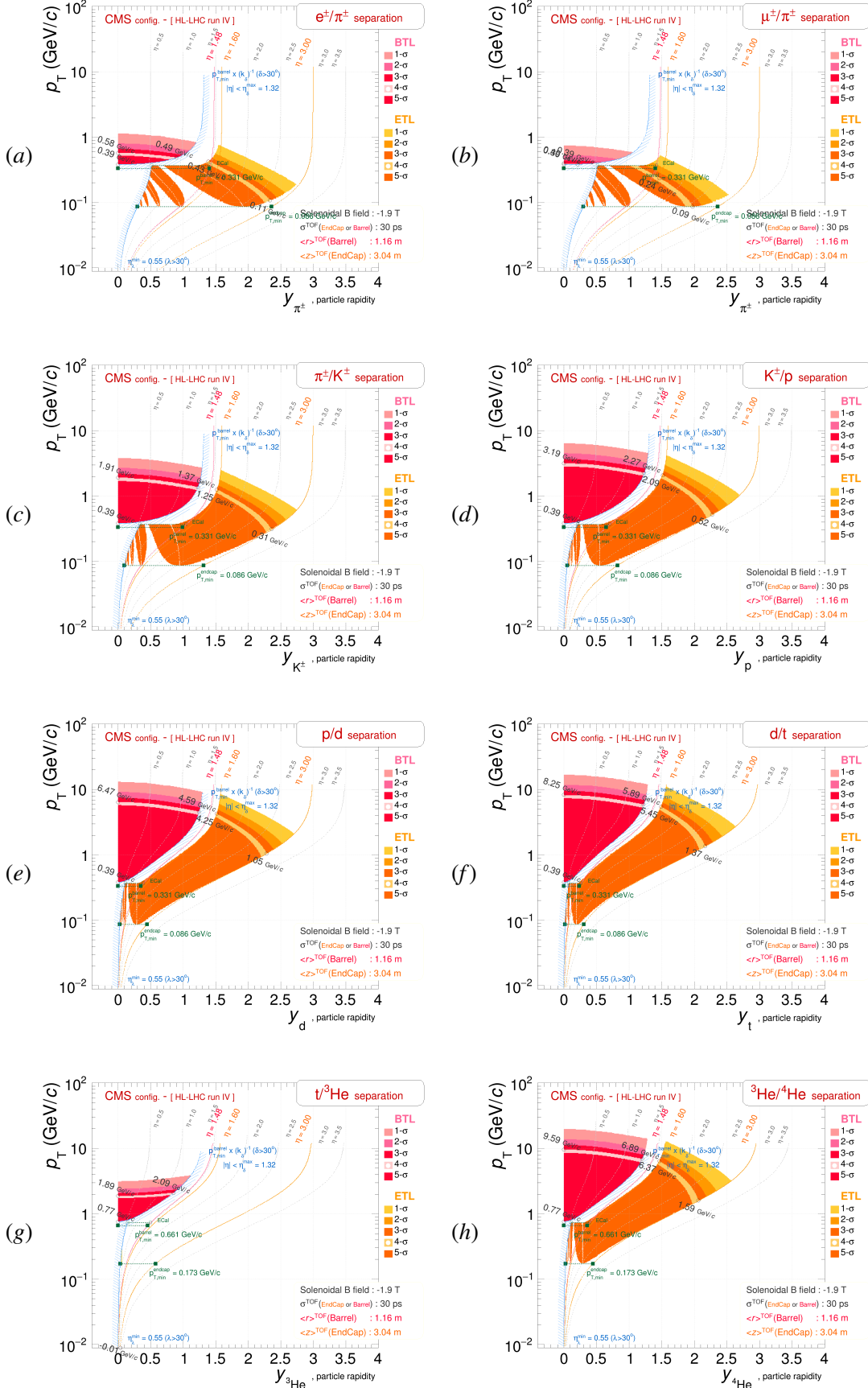


Fig. 49: Expected TOF performances in terms of particle separations as a function of p_T and y for the configuration already foreseen or possibly anticipated for the **CMS** experiment, with hypotheses :

- i) $\langle r_{TOF}^{barrel} \rangle = 1.16$ m, ii) $\langle z_{TOF}^{endcap} \rangle = 3.04$ m, iii) TOF timing resolution = 30 ps, iv) $B_{field} = -1.9$ T.



1316 **ATLAS** configurations

Fig. 50: Expected TOF performances in terms of particle separations as a function of p_T and y for the configuration already foreseen or possibly anticipated for the [ATLAS](#) experiment, with hypotheses :
 i) $\langle r_{TOF}^{barrel} \rangle = 0.29$ m, ii) $\langle z_{TOF}^{endcap} \rangle = 3.45$ m, iii) TOF timing resolution = 32 ps, iv) $B_{field} = -2.0$ T.

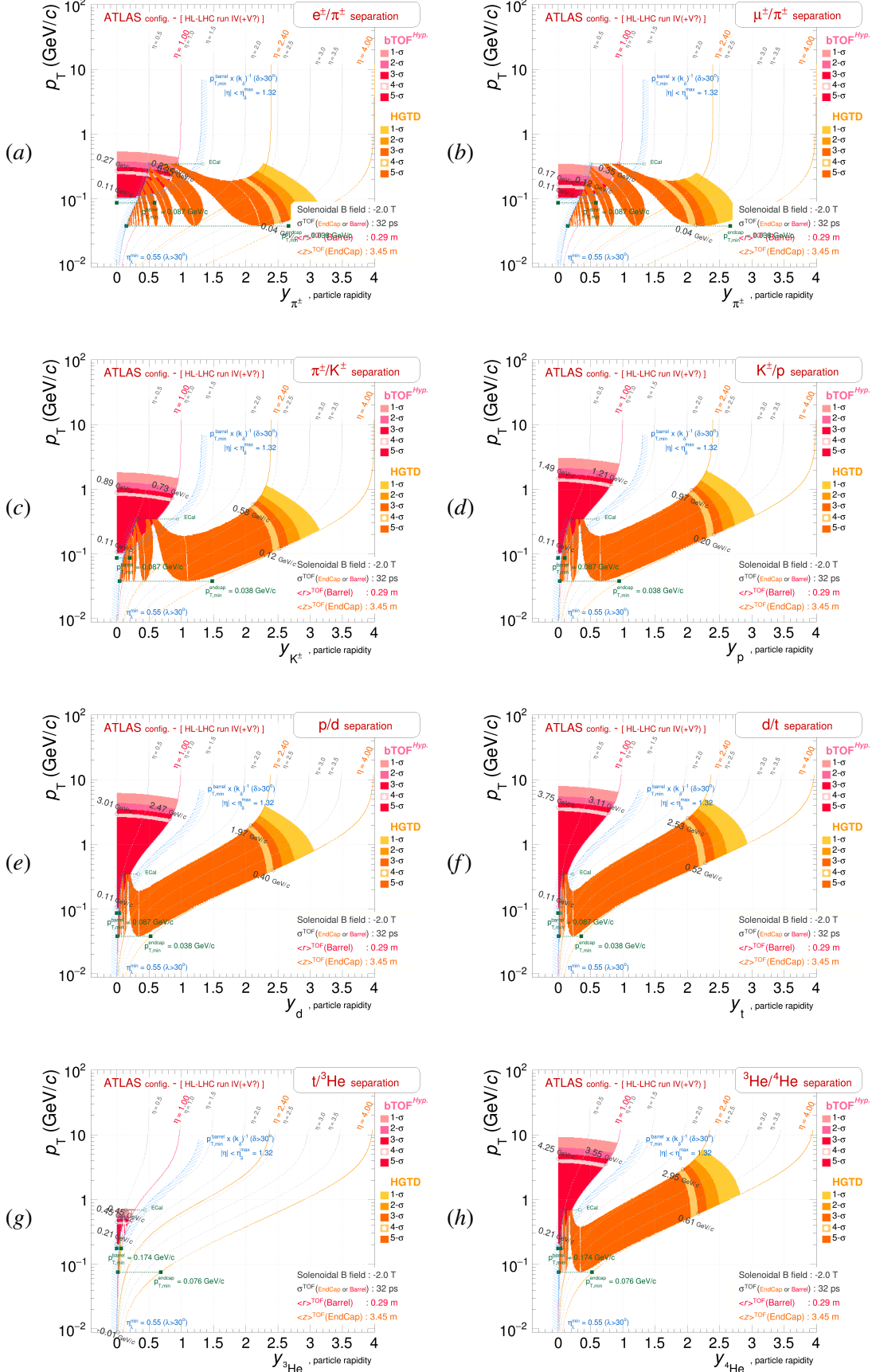


Fig. 51: Expected TOF performances in terms of particle separations as a function of p_T and y for the configuration already foreseen or possibly anticipated for the [ATLAS](#) experiment, with hypotheses :
i) $\langle r_{TOF}^{barrel} \rangle = 0.29$ m, *ii)* $\langle z_{TOF}^{endcap} \rangle = 3.45$ m, *iii)* TOF timing resolution = 32 ps, *iv)* $B_{field} = -1.0$ T.

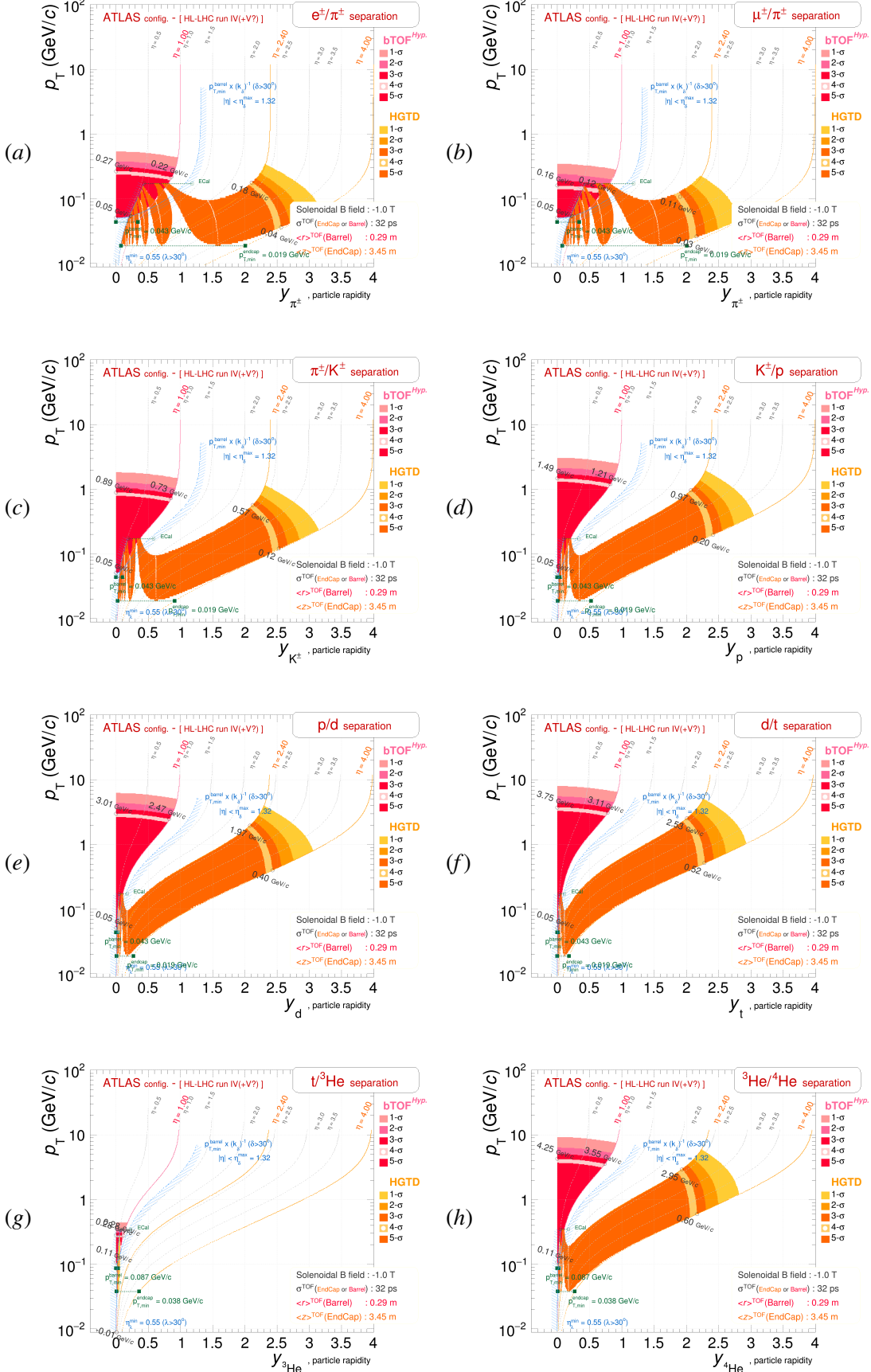


Fig. 52: Expected TOF performances in terms of particle separations as a function of p_T and y for the configuration already foreseen or possibly anticipated for the [ATLAS](#) experiment, with hypotheses :

- i) $\langle r_{TOF}^{barrel} \rangle = 1.00$ m, ii) $\langle z_{TOF}^{endcap} \rangle = 3.45$ m, iii) TOF timing resolution = 32 ps, iv) $B_{field} = -2.0$ T.

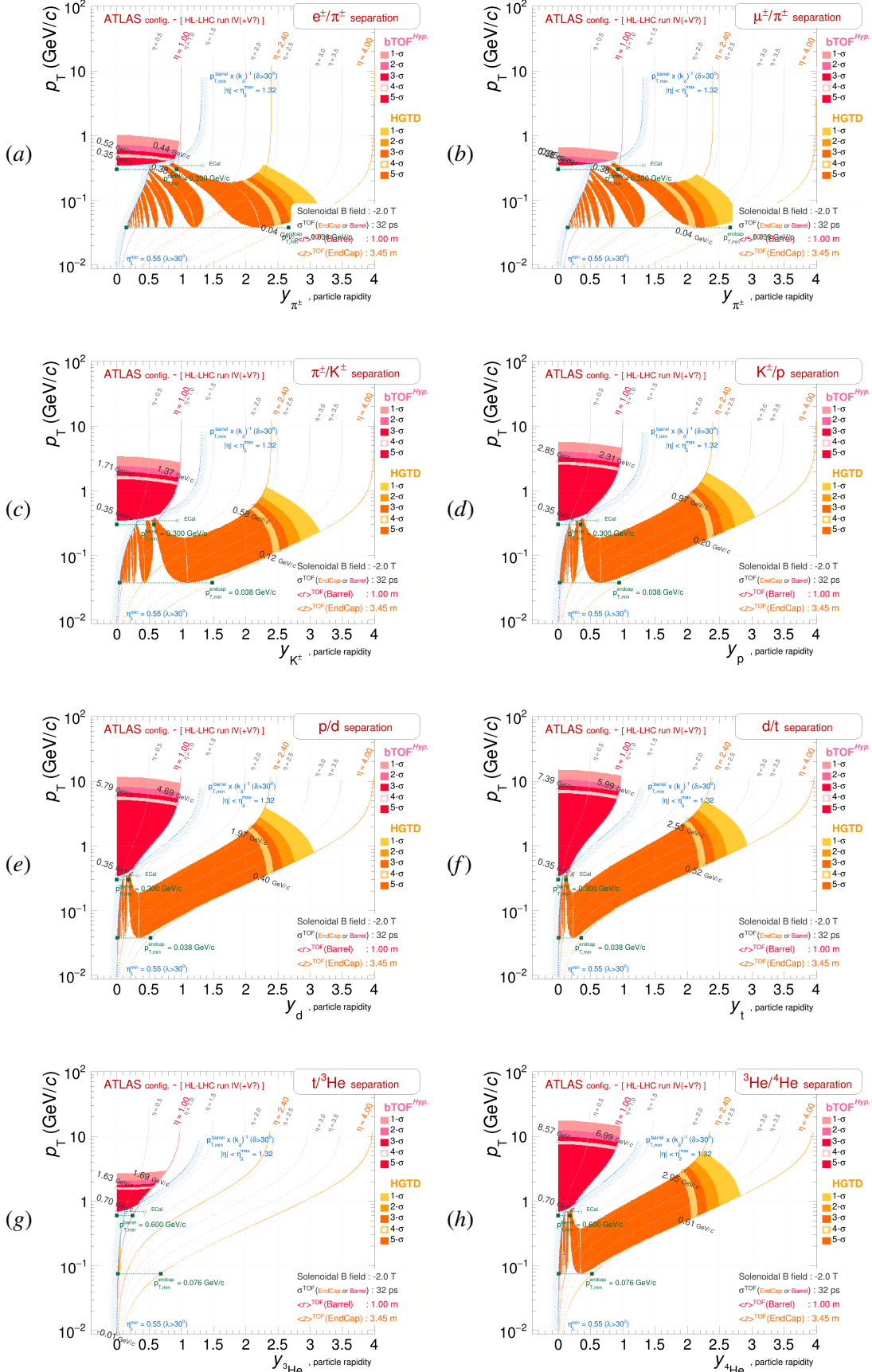


Fig. 53: Expected TOF performances in terms of particle separations as a function of p_T and y for the configuration already foreseen or possibly anticipated for the [ATLAS](#) experiment, with hypotheses :
 i) $\langle r_{TOF}^{barrel} \rangle = 1.00$ m, ii) $\langle z_{TOF}^{endcap} \rangle = 3.45$ m, iii) TOF timing resolution = 32 ps, iv) $B_{field} = -1.0$ T.

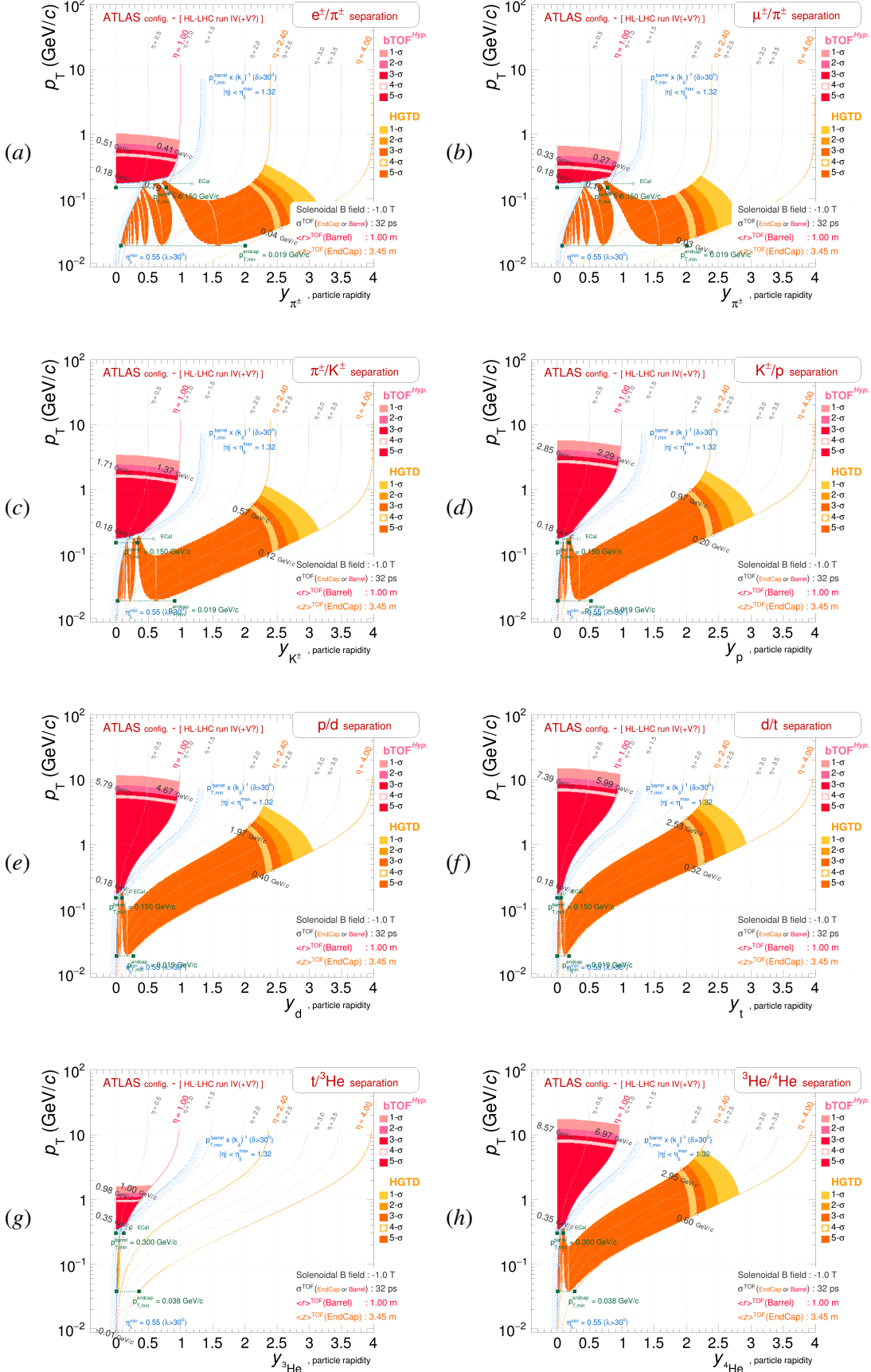


Fig. 54: Expected TOF performances in terms of particle separations as a function of p_T and y for the configuration already foreseen or possibly anticipated for the [ATLAS](#) experiment, with hypotheses :

- i) $\langle r_{TOF}^{barrel} \rangle = 0.29$ m, ii) $\langle z_{TOF}^{endcap} \rangle = 1.50$ m, iii) TOF timing resolution = 20 ps, iv) $B_{field} = -2.0$ T.

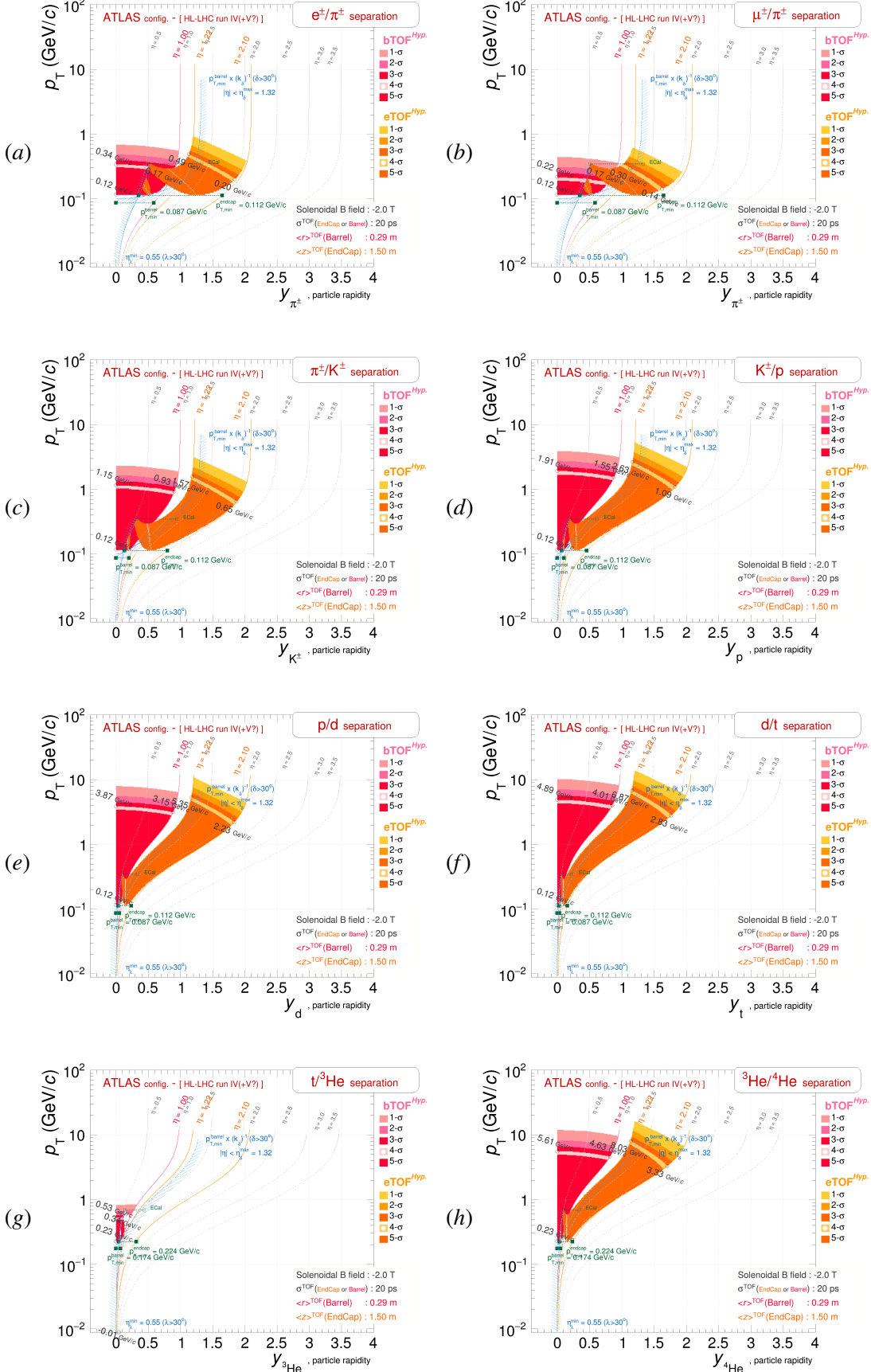


Fig. 55: Expected TOF performances in terms of particle separations as a function of p_T and y for the configuration already foreseen or possibly anticipated for the [ATLAS](#) experiment, with hypotheses :
 i) $\langle r_{TOF}^{barrel} \rangle = 0.29$ m, ii) $\langle z_{TOF}^{endcap} \rangle = 1.50$ m, iii) TOF timing resolution = 20 ps, iv) $B_{field} = -1.0$ T.

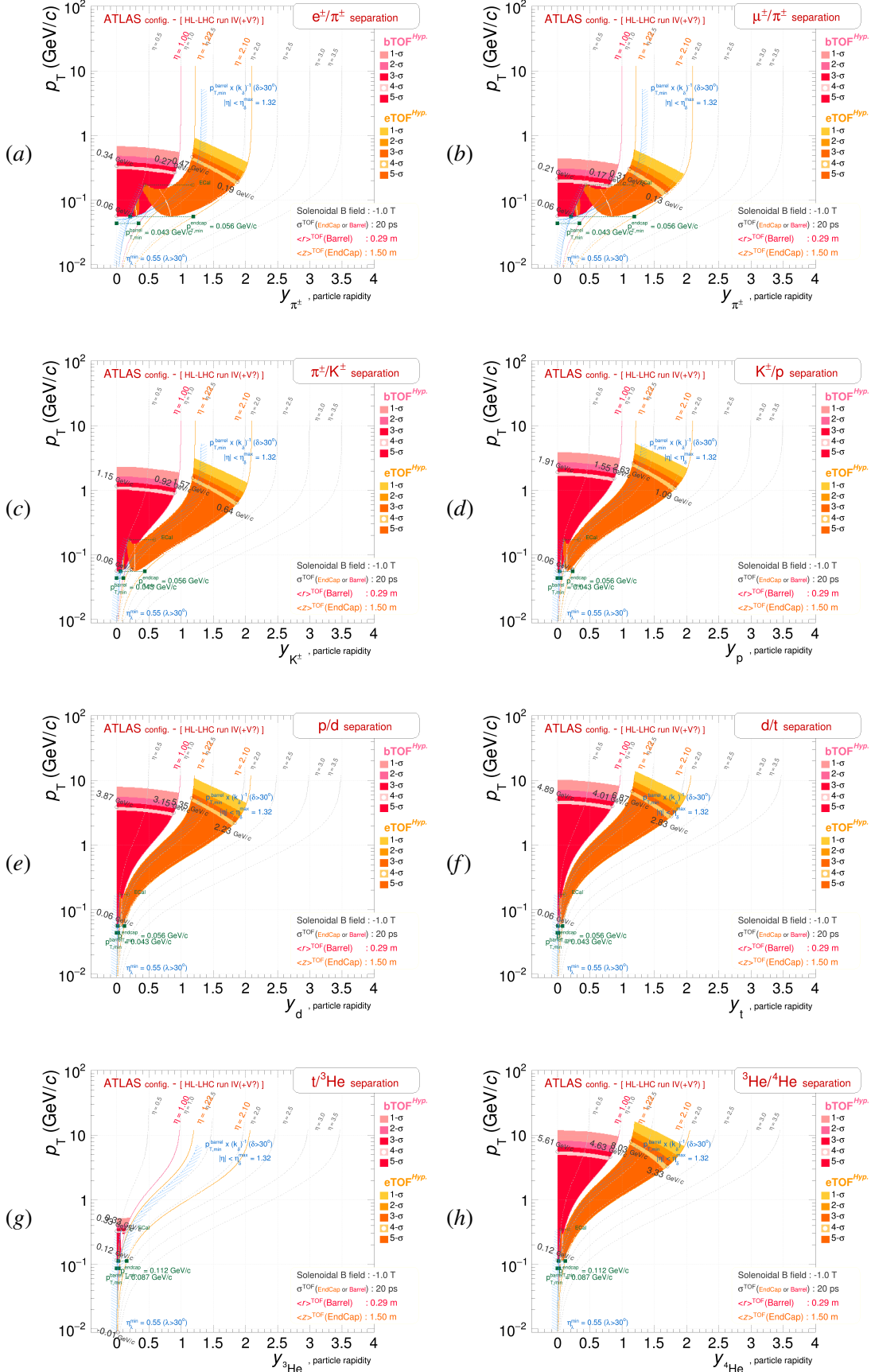


Fig. 56: Expected TOF performances in terms of particle separations as a function of p_T and y for the configuration already foreseen or possibly anticipated for the [ATLAS](#) experiment, with hypotheses :

i) $\langle r_{TOF}^{barrel} \rangle = 1.00$ m, ii) $\langle z_{TOF}^{endcap} \rangle = 1.50$ m, iii) TOF timing resolution = 20 ps, iv) $B_{field} = -2.0$ T.

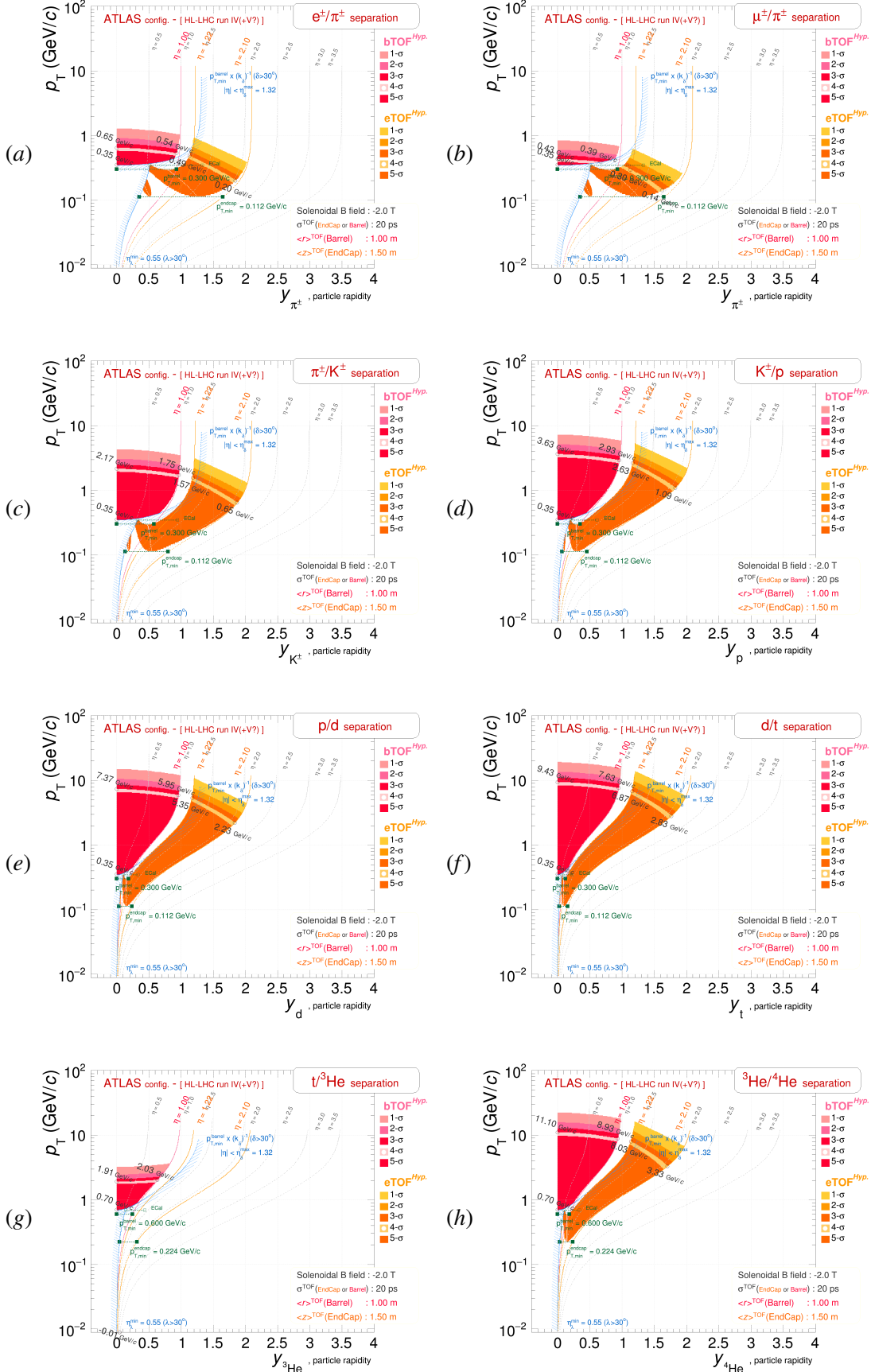
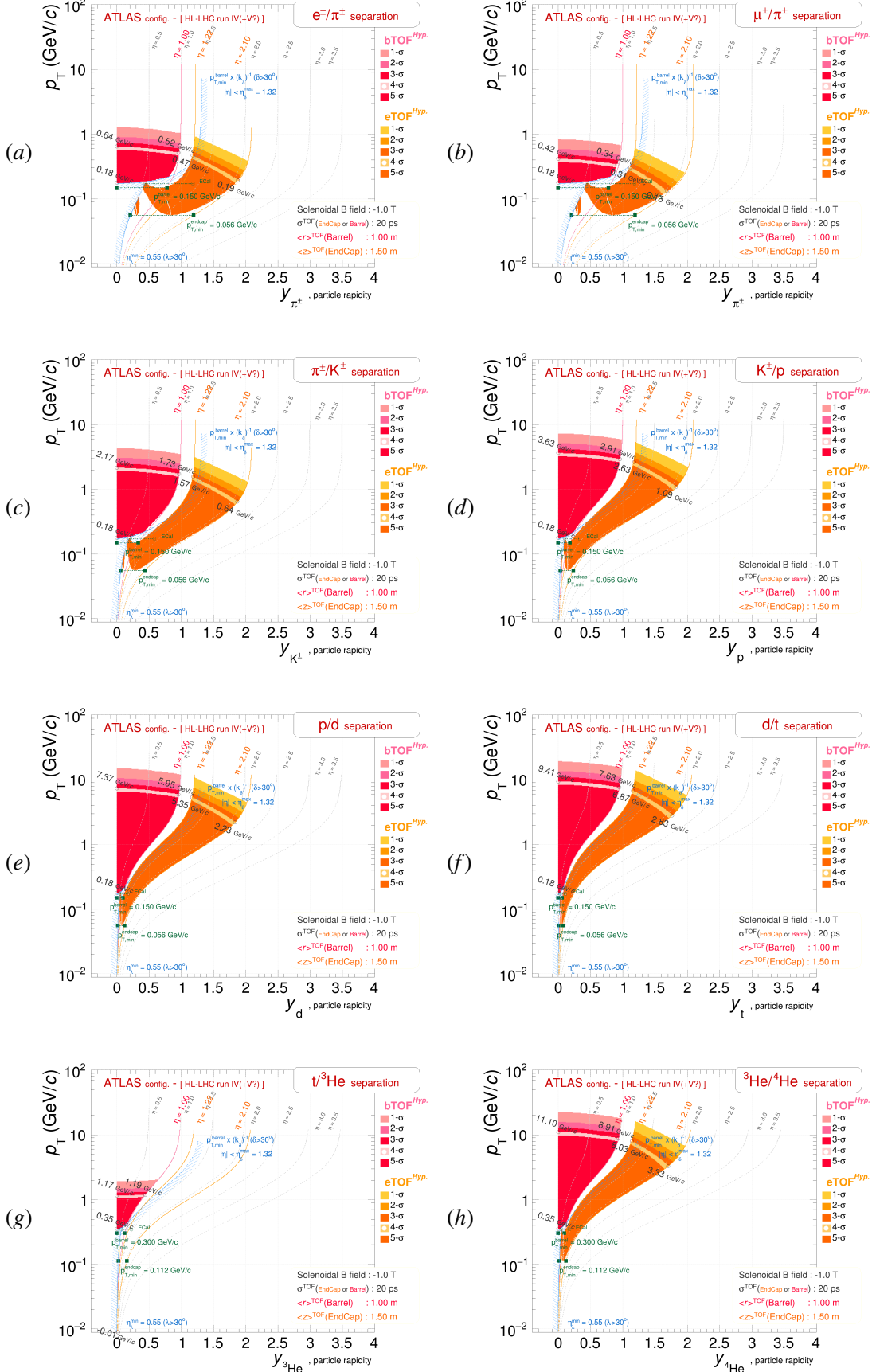


Fig. 57: Expected TOF performances in terms of particle separations as a function of p_T and y for the configuration already foreseen or possibly anticipated for the [ATLAS](#) experiment, with hypotheses :
 i) $\langle r_{TOF}^{barrel} \rangle = 1.00$ m, ii) $\langle z_{TOF}^{endcap} \rangle = 1.50$ m, iii) TOF timing resolution = 20 ps, iv) $B_{field} = -1.0$ T.



X Conclusion

1318 The document has presented the “analytical” figures of merit of various Time-Of-Flight configurations either at a proposal stage or already planned to take place at the HL-LHC, in the experiments ALICE-3, ATLAS and CMS, at the horizon of HL-LHC runs IV (≈ 2027 -2029) or V (> 2030). The calculated performances have been first discussed in view of the known performances of the existing TOF sub-detector in the ALICE-1 experiment at the LHC; the case can be considered as a litmus test to comprehend where the limits of the analytical exercise lay. 1320
 1322 The figures have been derived from analytical formulae describing purely helical trajectories in a solenoidal magnetic field of relativistic charged primary particles. The study is developed under the potentially crude hypothesis that there will be no alteration of any kind of the particle path and energy. This is carried out for different species (e^\pm , μ^\pm , π^\pm , K^\pm , p^\pm , d^\pm , t^\pm , ${}^3\text{He}^{2\pm}$, ${}^4\text{He}^{2\pm}$) allowing to assess the separation power 2-by-2 among the species, depending on the TOF locations, magnetic field intensity and time resolution. 1324
 1326
 1328

1330 Among the tested configurations, ALICE-3 shows the most extended potential in terms of p_T coverage, towards the low as well as the high transverse momenta.

1332 On the high p_T side, the 3 experiments exhibit more or less the same reach. For instance, for the casual π^\pm , K^\pm , p^\pm , the three experiments and their various configurations tested stay in a similar ballpark of 0.5 GeV/c. At high momentum, the magnitude of the magnetic field is of second-order effects; the impact of the material budget and $\mathcal{A} \cdot \mathcal{E}$ is getting less and less significant for $p_T > 2$ GeV/c. The crucial parameters are the position of the TOF sub-detector (the further away from the collision point, the better) and first and foremost the intrinsic timing resolution σ_{TOF} . The possible configurations of the various experiments are based more or less on the same distances to TOF, $\mathcal{O}(1$ m) at most for the barrels, $\mathcal{O}(2$ -3 m) for the endcaps, meaning that the stress is put, from one instrument to the next, on the σ_{TOF} difference. 1334
 1336
 1338
 1340

On the low-momentum side ($p_T < 1$ GeV/c), there, the access to phase space is quite different from one experiment to the other; the intensity of magnetic field is the prime parameter on paper, the material budget and $\mathcal{A} \cdot \mathcal{E}$ will be as well of decisive influences in practice. These are certainly the keys that will make measurements possible or simply forbid them irretrievably. Along the same line but with an impact even more exacerbated, on the ultra-low p_T ($p_T < 0.1$ GeV/c), only ALICE-3 may have the potential to explore such uncharted territories. 1342
 1344
 1346

All in all, ALICE-3 shows theoretically the most extended potential. But if the potential is the deepest, this is for the moment still only on paper... This raises the question of the competitiveness of ATLAS and CMS on the real ground. ATLAS and CMS already have a starting basis on track. Incomplete, one may say, with some caveats, admittedly, but still in position to contribute on the identification front. It is clear that, in the move from analytics presented here to concrete detector realisations in 5 to 10 years or so, ALICE-3 should be the experiment with the least PID chasm between the theoretical design and the real behaviour : with specifications on total material budget restricted to $\mathcal{O}(10\% X/X_0)$ only at mid-rapidity and similarly at forward rapidities, the distortions and surprises must be minimalised. But this will come with a certain price (after all, it is essentially a brand new experiment...) and with its lot of challenges : the detector prototype still needs to be demonstrated in great details, funded and, ultimately, produced. 1348
 1350
 1352
 1354
 1356
 1358

ALICE-3 appears as the ideal instrument to perform particle identification measurements in HL-LHC run V. On several aspects, it even seems that measurements will happen with ALICE-3 or nowhere else. The ultimate question can thus become how far the ALICE collaboration and experiment could *really* go, how far the measurements with the *real* instrument can be pushed. 1360
 1362

1364 **Acknowledgements**

1366 I would like here to warmly thank Wei Li from Rice University ([link](#)), member of the CMS
collaboration. The reader may notice similarities between the figures plotted in the present
1368 work and the Fig. 1.5 p.8 in the Technical Design Report of MTD detector [8]. And indeed,
Wei have kindly shared the original source code producing such a CMS figure, it has been the
first inspiration of the current code, adapted and enriched for the present work.

1370 I would also like to thank Iouri Belikov, Daniel Husson and Romain Schotter from the IPHC
for their time and contradiction on the mathematical derivation of the analytical formulae; my
1372 gratitude also goes to Boris Hippolyte and Yves Schutz as well as Federico Antinori, Jérôme
Baudot, David d'Enterria, Tanguy Pierog, Patrick Robbe and Isabelle Wingerter-Seez for hav-
1374 ing taken the long time of a careful and complete reading, in the frame of the "Habilitation"
(HDR) process.

1376 **A ROOT code snippet**

Listing 1: Macros/CodeSnippet-TOFseparation-Computation-v2020-08-08.C

```
1378 1
1379 2
1380 3
1381 4
1382 5 double cLight = 0.299792458; // = kB2C in AliRoot, [m.s^-1.V^-1]
1383 6 double qElem = 1.602176634e-19; // in Coulomb
1384 7
1385 8 ...
1386 9
1387 10
1388 11 double L1=0;
1389 12 double L2=0;
1390 13 Double_t cT_diff = 0;
1391 14 Double_t lTransvRotAngle = 0;
1392 15 UShort_t lAbsNbHalfTurns_Barrel1 = 0;
1393 16 UShort_t lAbsNbHalfTurns_Endcap1 = 0;
1394 17
1395 18 Int_t iDbleAcceptance = 0;
1396 19
1397 20
1398 21
1399 22 Bool_t kAbovePtMinEndcap = kFALSE;
1400 23 Bool_t kAbovePtMinBarrel = kFALSE;
1401 24 Bool_t kAbovePtMinCalo = kFALSE;
1402 25 Bool_t kAboveDeltaMinAngle = kFALSE;
1403 26 Bool_t kAboveLambdaMinAngle = kFALSE;
1404 27 Bool_t kLooper = kFALSE;
1405 28 Bool_t kWithinRZbarrelAcptce = kFALSE;
1406 29 Bool_t kWithinRZendcapAcptce = kFALSE;
1407 30 Bool_t IsPartForeseenInBarrel = kFALSE;
1408 31 Bool_t IsPartForeseenInEndcap = kFALSE;
1409 32 Bool_t IsPartForeseenBeyondEndcap = kFALSE;
1410 33
1411 34
1412 35
1413 36 for(Int_t iPt= 0; iPt < npt ; iPt++)
1414 37 {
1415 38 double pt = vPtBinning[ iPt ];
1416 39
1417 40 for(Int_t iEta = 0; iEta < neta; iEta++)
1418 41 {
1419 42
1420 43 // Reset booleans to start from clean ground at every sub-loop turn
1421 44 kAbovePtMinEndcap = kFALSE;
1422 45 kAbovePtMinBarrel = kFALSE;
1423 46 kAbovePtMinCalo = kFALSE;
1424 47 kAboveDeltaMinAngle = kFALSE;
1425 48 kAboveLambdaMinAngle = kFALSE;
1426 49 kLooper = kFALSE;
1427 50 kWithinRZbarrelAcptce = kFALSE;
1428 51 kWithinRZendcapAcptce = kFALSE;
1429 52 IsPartForeseenInBarrel = kFALSE;
1430 53 IsPartForeseenInEndcap = kFALSE;
1431 54 IsPartForeseenBeyondEndcap = kFALSE;
```

```

1432 55
1433 56 lAbsNbHalfTurns_Barrel1 = 0;
1434 57 lAbsNbHalfTurns_Endcap1 = 0;
1435 58
1436 59
1437 60 if(pt < lPtMinEndcap) continue; // below the endcap minimum pT, so no detection at all allowed
1438 61 else kAbovePtMinEndcap = kTRUE;
1439 62
1440 63
1441 64 if(pt > lPtMinBarrel) kAbovePtMinBarrel = kTRUE;
1442 65 // above the endcap minimum pT (loopers, regular endcap, regular barrel)
1443 66
1444 67 if(pt > lPtMinCalo) kAbovePtMinCalo = kTRUE;
1445 68 // above the reach of barrel calorimeter -> forget about double acceptance (barrel +endcap) loopers
1446 69
1447 70
1448 71
1449 72 Double_t eta = iEta*etastep;
1450 73 Double_t pl = pt * TMath::SinH(eta);
1451 74 Double_t ptot = TMath::Sqrt(pl*pl + pt*pt);
1452 75
1453 76
1454 77 Double_t energy1 = TMath::Sqrt(pt*pt + pl*pl + m1*m1);
1455 78 Double_t energy2 = TMath::Sqrt(pt*pt + pl*pl + m2*m2);
1456 79 Double_t rapidity1 = 0.5*log((energy1+pl)/(energy1-pl));
1457 80 Double_t rapidity2 = 0.5*log((energy2+pl)/(energy2-pl));
1458 81 Double_t gamma1 = TMath::Sqrt(1. + ptot*ptot/m1/m1);
1459 82 Double_t gamma2 = TMath::Sqrt(1. + ptot*ptot/m2/m2);
1460 83
1461 84
1462 85 if( eta > EtaMinLambda) kAboveLambdaMinAngle = kTRUE;
1463 86
1464 87 if( eta < EtaMaxDelta-etastep && pt > fnPtMinBarrelDelta->Eval(eta) ) kAboveDeltaMinAngle = kTRUE;
1465 88 // NOTE : due to discretisation of eta, one needs to remove one last etastep to avoid rounding effects between EtaMaxDelta and eta = i*etastep
1466 89
1467 90 if(
1468 91 kAboveLambdaMinAngle
1469 92 && kAbovePtMinEndcap
1470 93 && kAbovePtMinCalo == kFALSE
1471 94 && eta < lEtaMinEndcap
1472 95 && kActivateEndcap) kLooper = kTRUE;
1473 96
1474 97
1475 98
1476 99
1477 100
1478 101 // Wei's Lee code
1479 102 Bool_t kWeiCodeSwitch = kFALSE;
1480 103
1481 104
1482 105 if(!kWeiCodeSwitch){// Antonin Maire's math core of the code
1483 106
1484 107 Double_t AngFreq1 = (q1*qElem * lBz) / (gamma1 * m1InKg); // in rad.s-1, from var with international system unit q*e (C), m (kg), etc
1485 108 Double_t AngFreq2 = (q2*qElem * lBz) / (gamma2 * m2InKg);
1486 109
1487 110
1488 111 Double_t rho1 = pt / (clight * lBz * q1);
1489 112 Double_t rho2 = pt / (clight * lBz * q2);

```

```

1490 113
1491 114 Double_t betaZ1      = pt * TMath::SinH( eta ) / ( gamma1 * m1 );
1492 115 Double_t betaZ2      = pt * TMath::SinH( eta ) / ( gamma2 * m2 );
1493 116
1494 117
1495 118
1496 119 Double_t lPhit0 = 0.; // Initial azimuthal angle, by default = 0, could be anything in [0, 2pi] : TMath::Pi()/2. , ...
1497 120 // NOTE : ok for the trajectory
1498 121 // but still to be cured for the other displays : centre of curvature location, tan(t0)...
1499 122 // The physics quantities : path length, TOF time, straight lengths, Rt, rotation angle ...
1500 123 // should be left unchanged by this rotation
1501 124 // NOTE the helix will be rotated in block around the z axis, like a door on its hinges, by the side
1502 125 // so that in terms of acceptance the initial phi(t0) has NO effect, if the detector is invariant by rotation
1503 126 // the final TOF hit will end up always in the same circle, same radius, same z, just at a different location on it.
1504 127 // -> it has been proved here with phi(t0) = 90, 60, 45 deg, all the output looks the same
1505 128
1506 129 Double_t lTmpX = 0;
1507 130 Double_t lTmpY = 0;
1508 131
1509 132 Double_t ltf1 = 0;
1510 133 Double_t ltf2 = 0;
1511 134
1512 135
1513 136
1514 137 // Math for potential barrel case
1515 138 Double_t ltf_Barrel1 = TMath::Abs(1./AngFreq1) * 2 * TMath::ASin( lRbarrelTOF/ (2. * TMath::Abs(rho1)) );
1516 139 Double_t ltf_Barrel2 = TMath::Abs(1./AngFreq2) * 2 * TMath::ASin( lRbarrelTOF/ (2. * TMath::Abs(rho2)) );
1517 140
1518 141 Double_t lXtf_Barrel1 = -rho1 * TMath::Sin( AngFreq1 * ltf_Barrel1 ) ;
1519 142 Double_t lYtf_Barrel1 = -rho1 * ( TMath::Cos( AngFreq1 * ltf_Barrel1 ) - 1);
1520 143 Double_t lZtf_Barrel1 = betaZ1 * TMath::C() * ltf_Barrel1 ;
1521 144
1522 145 lTmpX = lXtf_Barrel1;
1523 146 lTmpY = lYtf_Barrel1;
1524 147
1525 148 lXtf_Barrel1 = lTmpX * TMath::Cos( lPhit0 ) - lTmpY * TMath::Sin( lPhit0 ); // trigo formula cos(a+b) : x = r. cos( phit ) -> x' = r. cos( phit + phi0 ) -> x'
1526 149 = x. cos(phi0) - y. sin(phi0)
1527 150 lYtf_Barrel1 = lTmpY * TMath::Cos( lPhit0 ) + lTmpX * TMath::Sin( lPhit0 ); // trigo formula sin(a+b) : y = r. sin( phit ) -> y' = r. sin( phit + phi0 ) -> y'
1528 151 = y. cos(phi0) + x. sin(phi0)
1529 152
1530 153 Double_t lXtf_Barrel2 = -rho2 * TMath::Sin( AngFreq2 * ltf_Barrel2 ) ;
1531 154 Double_t lYtf_Barrel2 = -rho2 * ( TMath::Cos( AngFreq2 * ltf_Barrel2 ) - 1);
1532 155 Double_t lZtf_Barrel2 = betaZ2 * TMath::C() * ltf_Barrel2 ;
1533 156
1534 157 lTmpX = lXtf_Barrel2;
1535 158 lTmpY = lYtf_Barrel2;
1536 159
1537 160 lXtf_Barrel2 = lTmpX * TMath::Cos( lPhit0 ) - lTmpY * TMath::Sin( lPhit0 ); // trigo formula cos(a+b)
1538 161 lYtf_Barrel2 = lTmpY * TMath::Cos( lPhit0 ) + lTmpX * TMath::Sin( lPhit0 ); // trigo formula sin(a+b)
1539 162
1540 163 Double_t lRt_tfBarrel1 = TMath::Sqrt( lXtf_Barrel1 * lXtf_Barrel1 + lYtf_Barrel1 * lYtf_Barrel1 );
1541 164 Double_t lRt_tfBarrel2 = TMath::Sqrt( lXtf_Barrel2 * lXtf_Barrel2 + lYtf_Barrel2 * lYtf_Barrel2 );
1542 165
1543 166
1544 167
1545 168 Double_t lTransvRotAngle_Barrel1 = 2 * TMath::ASin( lRt_tfBarrel1 /2. *1/(-rho1) );

```

```

1548 169 // NOTE : beware = signed angle here, in accordance with right-angled frame (0;x,y,z)
1549 170
1550 171
1551 172 // NOTE : should be valid for both TOF barrel and endcap...
1552 173 // NOTE : It is just that, in the barrel case, lRt_tf should be = lRbarrelTOF ...
1553 174 // NOTE : but ... not valid if several half-turns !
1554 175 // This is only valid within [0, pi] = via visible final and concrete Rtf
1555 176 // i.e. valid for a track that stays in the 1st quadrant, phi in [0;pi/2]
1556 177 // = rotation around centre between [0;pi]
1557 178 // That is typically true for that track meant to TOF barrel layer.
1558 179 // But may not always be true for endcap (>180 deg or loopers, etc)
1559 180 // Hence the need to compute a specific angle for endcap...
1560 181
1561 182 lAbsNbHalfTurns_Barrel1 = TMath::Floor( TMath::Abs( lTransvRotAngle_Barrel1 *TMath::RadToDeg()/180.));
1562 183 // NOTE : number of completed half turn(s)
1563 184 // Should always be 0 in the physics case for barrel, no loopers allowed
1564 185
1565 186
1566 187
1567 188
1568 189
1569 190
1570 191
1571 192 // Math for potential endcap case
1572 193 Double_t ltf_Endcap1 = TMath::Abs( lZendcapTOF / ( TMath::C() * betaZ1 ) );
1573 194 Double_t ltf_Endcap2 = TMath::Abs( lZendcapTOF / ( TMath::C() * betaZ2 ) );
1574 195
1575 196 Double_t lXtf_Endcap1 = -rho1 * TMath::Sin( AngFreq1 * ltf_Endcap1 ) ;
1576 197 Double_t lYtf_Endcap1 = -rho1 * ( TMath::Cos( AngFreq1 * ltf_Endcap1 ) - 1);
1577 198 Double_t lZtf_Endcap1 = betaZ1 * TMath::C() * ltf_Endcap1 ;
1578 199
1579 200 lTmpX = lXtf_Endcap1;
1580 201 lTmpY = lYtf_Endcap1;
1581 202
1582 203 lXtf_Endcap1 = lTmpX * TMath::Cos( lPhit0 ) - lTmpY * TMath::Sin( lPhit0 ); // trigo formula cos(a+b)
1583 204 lYtf_Endcap1 = lTmpY * TMath::Cos( lPhit0 ) + lTmpX * TMath::Sin( lPhit0 ); // trigo formula sin(a+b)
1584 205
1585 206
1586 207
1587 208 Double_t lXtf_Endcap2 = -rho2 * TMath::Sin( AngFreq2 * ltf_Endcap2 ) ;
1588 209 Double_t lYtf_Endcap2 = -rho2 * ( TMath::Cos( AngFreq2 * ltf_Endcap2 ) - 1);
1589 210 Double_t lZtf_Endcap2 = betaZ2 * TMath::C() * ltf_Endcap2 ;
1590 211
1591 212 lTmpX = lXtf_Endcap2;
1592 213 lTmpY = lYtf_Endcap2;
1593 214
1594 215 lXtf_Endcap2 = lTmpX * TMath::Cos( lPhit0 ) - lTmpY * TMath::Sin( lPhit0 ); // trigo formula cos(a+b)
1595 216 lYtf_Endcap2 = lTmpY * TMath::Cos( lPhit0 ) + lTmpX * TMath::Sin( lPhit0 ); // trigo formula sin(a+b)
1596 217
1597 218
1598 219 Double_t lRt_tfEndcap1 = TMath::Sqrt( lXtf_Endcap1 * lXtf_Endcap1 + lYtf_Endcap1 * lYtf_Endcap1 );
1599 220 Double_t lRt_tfEndcap2 = TMath::Sqrt( lXtf_Endcap2 * lXtf_Endcap2 + lYtf_Endcap2 * lYtf_Endcap2 );
1600 221
1601 222
1602 223 Double_t lTransvRotAngle_Endcap1 = lZtf_Endcap1/(-rho1 * TMath::SinH(eta)); // e22 in South face p.9
1603 224 lAbsNbHalfTurns_Endcap1 = TMath::Floor( TMath::Abs( lTransvRotAngle_Endcap1 *TMath::RadToDeg()/180.));
1604 225
1605 226

```

```

1606 227
228
1608 229
230
1610 231
232
1612 233   if(      kLooper
234         && (lRt_tfEndcap1 < lRminEndcap || lRt_tfEndcap1 > lRmaxEndcap)
1614 235       )
236         // acceptance check : track ends up below lRminEndcap, so undo the flag if necessary.
1616 237
238         // if(kLooper && lAbsNbHalfTurns_Endcap1 != 1) kLooper = kFALSE;
1618 239         // NOTE : For investigations on rotation for loopers : isolate a given number of half turn + apply 1.1427 (~15 lines below)
240
1620 241
242
1622 243
244   if(
1624 245       TMath::Abs(lZtf_Barrel1) < lZmaxBarrel
246       && TMath::Abs(lRt_tfBarrel1 - lRbarrelTOF) < 2e-3
1626 247       //&& lAbsNbHalfTurns_Barrel1 == 0
248     ){
1628 249         kWithinRZbarrelAcptce = kTRUE; }
250
1630 251   if( lRt_tfEndcap1 < lRmaxEndcap           // WARNING : not a else if, but an independent if to allow for double acceptance !
252       && lRt_tfEndcap1 > lRminEndcap
1632 253       && TMath::Abs(lZtf_Endcap1 - lZendcapTOF) < 2e-3
254       //&& lAbsNbHalfTurns_Endcap1 == 1
1634 255     ){
256         kWithinRZendcapAcptce = kTRUE; }
1636 257
258
1638 259
260
1640 261   if ( kWithinRZbarrelAcptce  && kWithinRZendcapAcptce && kActivateEndcap){
262     ++iDbleAcceptance;
1642 263     if(lDebug > 1) Printf("Double acceptance (barrel + endcap) Point [pT = %6.4g GeV/c ; y1 = %6.4f / eta = %6.4f ] :", pt, rapidity1, eta );
264
1644 265
266     // 2nd thought needed : Reevaluate the assignment in terms of acceptance : only in barrel, only in endcap or in both, finally
1646 267
268     if( kWithinRZbarrelAcptce && kAbovePtMinCalo )           kWithinRZendcapAcptce = kFALSE;
1648 269     // NOTE : the track, first and foremost a barrel track, will stop in calorimeter,
270     //         so for sure will not manage to further loop back towards the endcap plane
1650 271     //         In practice, it can only be a barrel TOF measurement
272
1652 273     if( kWithinRZbarrelAcptce && kAboveLambdaMinAngle == kFALSE ) kWithinRZendcapAcptce = kFALSE;
274     // NOTE : track, first and foremost a barrel track, is here a priori allowed to loop
1654 275     //         - above the TOF barrel radius
276     //         - but below the calorimeter one
1656 277     //         and thus loop towards the endcap !
278     //         But then , the requirement about the minimal inclination angle is not met : lambda too small
1658 279     //         In practice, it will remain a clean measurement only in barrel TOF.
280
1660 281     if(kRelaxAngConstraints)           kWithinRZendcapAcptce = kTRUE;
282     // NOTE : to visualise the full phase ~without constraints (calo, lambda, delta angles)
1662 283
284   }

```

```

1664 285
1666 286
1666 287
1666 288
1668 289   if(kLooper  && kActivateEndcap){
1670 290       ltf1 = ltf_Endcap1;
1670 291       ltf2 = ltf_Endcap2;
1672 292   }
1672 293   else if(kWithinRZendcapAcptce  && kActivateEndcap){ // simplistic case : eta > lEtaMinEndcap   or more advanced version : kWithinRZendcapAcptce
1674 294       IsPartForeseenInEndcap = kTRUE;
1674 295       ltf1 = ltf_Endcap1;
1674 296       ltf2 = ltf_Endcap2;
1676 297   }
1676 298   else if(kWithinRZbarrelAcptce){ // simplistic case : eta < lEtaMaxBarrel   or more advanced version : kWithinRZbarrelAcptce
1678 299       IsPartForeseenInBarrel = kTRUE;
1680 300       ltf1 = ltf_Barrel1;
1680 301       ltf2 = ltf_Barrel2;
1682 302   }
1682 303
1682 304
1684 305   cT_diff = TMath::Abs( ltf1 - ltf2 ) * 1e9; // time, from seconds to nanoseconds
1686 306   // if(IsPartForeseenInBarrel){
1686 307   // if( TMath::Abs(pt - 1.00) < 0.01 && TMath::Abs(eta - 0.65) < 1e-2   )
1688 308   //   Printf("Point [pT = %6.4g GeV/c ; y1 = %6.4f / y2 = %6.4f / eta = %6.4f ] : ctdiff = [tf1 = %8.6g] - [tf2 = %8.6g] = %8.6g ns", pt, rapidity1, rapidity2, eta, ltf1,
1690 309   //         ltf2, cT_diff);
1690 310   // }
1692 311
1692 312 }
1694 313 }
1694 314 else{// Wei Li's core code
1694 315   if(eta<lEtaMaxBarrel){
1696 316       L1 = pt/clight*cosh(eta)/lBz/q1*acos(1-lBz*lBz*q1*q1*lRbarrelTOF*lRbarrelTOF/pt/pt*clight*clight/2.);
1696 317       L2 = pt/clight*cosh(eta)/lBz/q2*acos(1-lBz*lBz*q2*q2*lRbarrelTOF*lRbarrelTOF/pt/pt*clight*clight/2.);
1698 318   }
1700 319   else if(eta>lEtaMinEndcap && kActivateEndcap){
1700 320       L1 = lZendcapTOF / tanh(eta);
1700 321       L2 = lZendcapTOF / tanh(eta);
1702 322   }
1704 323   else{
1704 324       L1 = 0;
1704 325       L2 = 0;
1706 326   }
1706 327
1708 328   double beta1_inv = sqrt(m1*m1/pt/pt/cosh(eta)/cosh(eta)+1);
1708 329   double beta2_inv = sqrt(m2*m2/pt/pt/cosh(eta)/cosh(eta)+1);
1710 330   cT_diff = fabs( beta1_inv*L1 - beta2_inv*L2 )/clight;
1710 331
1712 332   if(eta<lEtaMaxBarrel) IsPartForeseenInBarrel = kTRUE;
1712 333   if(eta>lEtaMinEndcap) IsPartForeseenInEndcap = kTRUE;
1714 334
1714 335   // NB : No looper anticipated in Wei's code
1716 336
1716 337 }// end Wei's code
1718 338
1718 339
1720 340   if(IsPartForeseenInBarrel && kAboveDeltaMinAngle){
1720 341

```

```

1722 342     if( cT_diff > n5sigma*cDeltaT )     h5sigm_barrel[ iCan ] ->SetBinContent( h5sigm_barrel[ iCan ] ->FindBin(rapidity1,pt), 1);
343     if( cT_diff > n4sigma*cDeltaT )     h4sigm_barrel[ iCan ] ->SetBinContent( h4sigm_barrel[ iCan ] ->FindBin(rapidity1,pt), 1);
1724 344     if( cT_diff > n3sigma*cDeltaT )     h3sigm_barrel[ iCan ] ->SetBinContent( h3sigm_barrel[ iCan ] ->FindBin(rapidity1,pt), 1);
345     if( cT_diff > n2sigma*cDeltaT )     h2sigm_barrel[ iCan ] ->SetBinContent( h2sigm_barrel[ iCan ] ->FindBin(rapidity1,pt), 1);
1726 346     if( cT_diff > n1sigma*cDeltaT )     h1sigm_barrel[ iCan ] ->SetBinContent( h1sigm_barrel[ iCan ] ->FindBin(rapidity1,pt), 1);
347 }
1728 348
349 if(IsPartForeseenInEndcap && kAboveLambdaMinAngle){
1730 350     if( cT_diff > n5sigma*cDeltaT )     h5sigm_ecap [ iCan ] ->SetBinContent( h5sigm_ecap [ iCan ] ->FindBin(rapidity1,pt), 10+1AbsNbHalfTurns_Endcap1);
351     if( cT_diff > n4sigma*cDeltaT )     h4sigm_ecap [ iCan ] ->SetBinContent( h4sigm_ecap [ iCan ] ->FindBin(rapidity1,pt), 10+1AbsNbHalfTurns_Endcap1);
1732 352     if( cT_diff > n3sigma*cDeltaT )     h3sigm_ecap [ iCan ] ->SetBinContent( h3sigm_ecap [ iCan ] ->FindBin(rapidity1,pt), 10+1AbsNbHalfTurns_Endcap1);
353     if( cT_diff > n2sigma*cDeltaT )     h2sigm_ecap [ iCan ] ->SetBinContent( h2sigm_ecap [ iCan ] ->FindBin(rapidity1,pt), 10+1AbsNbHalfTurns_Endcap1);
1734 354     if( cT_diff > n1sigma*cDeltaT )     h1sigm_ecap [ iCan ] ->SetBinContent( h1sigm_ecap [ iCan ] ->FindBin(rapidity1,pt), 10+1AbsNbHalfTurns_Endcap1);
355 }
1736 356
357 if(kLooper){
1738 358     if( cT_diff > n5sigma*cDeltaT )     h5sigm_loop [ iCan ] ->SetBinContent( h5sigm_loop [ iCan ] ->FindBin(rapidity1,pt), 10+1AbsNbHalfTurns_Endcap1);
359     if( cT_diff > n4sigma*cDeltaT )     h4sigm_loop [ iCan ] ->SetBinContent( h4sigm_loop [ iCan ] ->FindBin(rapidity1,pt), 10+1AbsNbHalfTurns_Endcap1);
1740 360     if( cT_diff > n3sigma*cDeltaT )     h3sigm_loop [ iCan ] ->SetBinContent( h3sigm_loop [ iCan ] ->FindBin(rapidity1,pt), 10+1AbsNbHalfTurns_Endcap1);
361     if( cT_diff > n2sigma*cDeltaT )     h2sigm_loop [ iCan ] ->SetBinContent( h2sigm_loop [ iCan ] ->FindBin(rapidity1,pt), 10+1AbsNbHalfTurns_Endcap1);
1742 362     if( cT_diff > n1sigma*cDeltaT )     h1sigm_loop [ iCan ] ->SetBinContent( h1sigm_loop [ iCan ] ->FindBin(rapidity1,pt), 10+1AbsNbHalfTurns_Endcap1);
363 }
1744 364
365
1746 366
367
1748 368 }// end loop iEta
1750 369 }// end loop pt

```

101

References

- 1752 [1] F. Antinori, A. Morsch, L. Musa, et al., *A next-generation LHC heavy-ion experiment*, arXiv, Input for the
2019 CERN council Open Symposium in Granada (May 2019), in view of the 2020 update of the European
1754 Strategy for Particle Physics, Feb. 2019. [arXiv:1902.01211](#).
- [2] J. W. Holt, M. Rho, and W. Weise, *Chiral symmetry and effective field theories for hadronic, nuclear and
1756 stellar matter*, *Phys. Rept.* **621** (2016) 2–75, [[arXiv:1411.6681](#)].
- [3] F. Low, *Bremsstrahlung of very low-energy quanta in elementary particle collisions*, *Phys. Rev. Lett.* **110**
1758 (1958) 974–977. [DOI Link](#).
- [4] A. Strominger, *Lectures on the Infrared Structure of Gravity and Gauge Theory*, [arXiv:1703.05448](#).
- 1760 [5] C. Lippmann, *Particle identification*, *Nucl. Instrum. and Methods A* **666** (2011) 148–172,
[\[arXiv:1101.3276\]](#). [DOI Link](#).
- 1762 [6] **Fluka collab.**, *Fluka home page*, Web, 2020. [www.fluka.org/](#).
- [7] **Geant4 collab.**, *Geant4 home page*, Web, 2020. [/geant4.web.cern.ch/](#).
- 1764 [8] **CMS collab.**, *A MIP Timing Detector for the CMS Phase-2 Upgrade*, technical design report, CERN, 2019.
CERN-LHCC-2019-003 / CMS-TDR-020, [/cds.cern.ch/record/2667167](#).
- 1766 [9] A. Maire, *GitHub - TOFseparationPowerAsFuncPtY, source code*, GitHub, GNU GPL v3.0 / Corresponding
article : arXiv:..., March 2021. [/github.com/maireiphc/TOFseparationPowerAsFuncPtY](#).
- 1768 [10] A. Akimov, A. Alici, A. Agostinelli, P. Antonioli, S. Arcelli, M. Basile, F. Bellini, G. Cara Romeo,
1770 L. Cifarelli, F. Cindolo, M. Colocci, A. De Caro, D. De Gruttola, S. De Pasquale, K. Doroud,
M. Fusco Girard, B. Guerzoni, D. Hatzifotiadou, D. Kim, J. Kim, S. Kiselev, S. Lee, D. Malkevich,
1772 A. Margotti, R. Nania, A. Nedosekin, F. Noferini, P. Pagano, A. Pesci, O. Pinazza, R. Preghenella,
E. Scapparone, G. Scioli, K. Voloshin, M. Williams, C. Zampolli, and A. Zichichi, *Performance of the
ALICE Time-Of-Flight detector at the LHC*, *Eur. J. Phys. Plus* **128** (2013) 44. [DOI Link](#).
- 1774 [11] **ALICE collab.**, *Performance of the ALICE Experiment at the CERN LHC*, *Int. J. Mod. Phys. A* **29** (2014)
1430044, [[arXiv:1402.4476](#)]. [DOI Link](#).
- 1776 [12] F. Carnesecchi (on behalf of the ALICE Collaboration), *Performance of the ALICE Time-Of-Flight detector
at the LHC*, [arXiv:1806.03825](#).
- 1778 [13] **ALICE collab.**, *Production of charged pions, kaons and (anti-)protons in Pb-Pb and inelastic pp collisions
at $\sqrt{s_{NN}} = 5.02$ TeV*, *Phys. Rev. C* **101** (2020) 044907, [[arXiv:1910.07678](#)]. [DOI Link](#).
- 1780 [14] **ALICE collab.**, *Determination of the event collision time with the ALICE detector at the LHC*, *Eur. Phys. J.
Plus* **132** (2017) 99, [[arXiv:1610.03055](#)]. [DOI Link](#).
- 1782 [15] **ALICE collab.**, *Centrality dependence of pion, kaon, and proton production in Pb-Pb collisions at $\sqrt{s_{NN}} =$
2.76 TeV*, *Phys. Rev. C* **88** (2013) 044910, [[arXiv:1303.0737](#)]. [DOI Link](#).
- 1784 [16] **ALICE collab.**, *Measurement of pion, kaon and proton production in proton-proton collisions at $\sqrt{s} = 7$ TeV*,
Eur. Phys. J. C **75** (2015) 226, [[arXiv:1504.00024](#)]. [DOI Link](#).
- 1786 [17] **ALICE collab.**, *Multiplicity dependence of π , K, and p production in pp collisions at $\sqrt{s} = 13$ TeV*, *Eur.
Phys. J. C* **80** (2020) 693, [[arXiv:2003.02394](#)]. [DOI Link](#).
- 1788 [18] **ALICE collab.**, *Production of deuterons, tritons, ^3He nuclei and their anti-nuclei in pp collisions at $\sqrt{s} =$
0.9, 2.76 and 7 TeV*, *Phys. Rev. C* **97** (2018), no. 2 024615, [[arXiv:1709.08522](#)]. [DOI Link](#).
- 1790 [19] **ALICE collab.**, *Multiplicity dependence of (anti-)deuteron production in pp collisions at $\sqrt{s} = 7$ TeV*, *Phys.
Lett. B* **794** (2019) 50–63, [[arXiv:1902.09290](#)]. [DOI Link](#).
- 1792 [20] **ALICE collab.**, *(Anti-)Deuteron production in pp collisions at $\sqrt{s} = 13$ TeV*, [arXiv:2003.03184](#).
- 1794 [21] **ALICE collab.**, *Measurement of deuteron spectra and elliptic flow in Pb-Pb collisions at $\sqrt{s_{NN}} = 2.76$ TeV
at the LHC*, *Eur. Phys. J. C* **77** (2017) 658, [[arXiv:1707.07304](#)]. [DOI Link](#).

- 1796 [22] **ALICE collab.**, ${}^3_{\Lambda}\text{H}$ and ${}^3_{\Lambda}\bar{\text{H}}$ production in Pb-Pb collisions at $\sqrt{s_{\text{NN}}} = 2.76$ TeV, *Phys. Lett. B* **754** (2016) 360–372, [[arXiv:1506.08453](#)]. [DOI Link](#).
- 1798 [23] **ALICE collab.**, ${}^3_{\Lambda}\text{H}$ and ${}^3_{\Lambda}\bar{\text{H}}$ lifetime measurement in Pb-Pb collisions at $\sqrt{s_{\text{NN}}} = 5.02$ TeV via two-body decay, [arXiv:1907.06906](#).
- 1800 [24] **RD50 collab.**, *RD50 - Radiation hard semiconductor devices for very high luminosity colliders*, Web, 2012-. [/rd50.web.cern.ch/](#).
- 1802 [25] **ATLAS collab.**, *Technical Proposal: A High-Granularity Timing Detector for the ATLAS Phase-II Upgrade*, tech. rep., CERN, 2018. CERN-LHCC-2018-023, [/cds.cern.ch/record/2623663](#).
- 1804 [26] G. Paternoster, G. Borghi, M. Boscardin, N. Cartiglia, M. Ferrero, F. Ficorella, F. Siviero, A. Gola, and P. Bellutti, *Trench-Isolated Low Gain Avalanche Diodes (TI-LGADs)*, *IEEE Electron Device Letters* **41** (2020) 884–887. [DOI Link](#).
- 1806 [27] N. Cartiglia, R. Arcidiacono, G. Borghi, M. Boscardin, M. Costa, Z. Galloway, F. Fausti, M. Ferrero, F. Ficorella, M. Mandurrino, S. Mazza, E. J. Olave, G. Paternoster, F. Siviero, H. F.-W. Sadrozinski, V. Sola, A. Staiano, A. Seiden, M. Tornago, and Y. Zhao, *LGAD designs for future particle trackers*, *Nucl. Instrum. A* (2020) [[arXiv:2003.13990](#)]. [DOI Link](#).
- 1810 [28] M. Mandurrino, N. Cartiglia, M. Tornago, M. Ferrero, F. Siviero, G. Paternoster, F. Ficorella, M. Boscardin, L. Pancheri, and G. F. D. Betta, *High performance picosecond- and micron-level 4D particle tracking with 100% fill-factor Resistive AC-Coupled Silicon Detectors (RSD)*, [arXiv:2003.04838](#).
- 1812 [29] E. Grossi, A. Soloviev, D. Teaney, and F. Yan, *Transport and hydrodynamics in the chiral limit*, *Phys. Rev. D* **102** (2020) 014042, [[arXiv:2005.02885](#)]. [DOI Link](#).
- 1814 [30] M. Bluhm, M. Nahrgang, A. Kalweit, M. Arslanok, P. Braun-Munzinger, S. Floerchinger, E. S. Fraga, M. Gazdzicki, C. Hartnack, C. Herold, R. Holzmann, I. Karpenko, M. Kitazawa, V. Koch, S. Leupold, A. Mazeliauskas, B. Mohanty, A. Ohlson, D. Oliinychenko, J. M. Pawlowski, C. Plumberg, G. W. Ridgway, T. Schäfer, I. Selyuzhenkov, J. Stachel, M. Stephanov, D. Teaney, N. Touroux, V. Vovchenko, and N. Wink, *Dynamics of critical fluctuations: Theory – phenomenology – heavy-ion collisions*, [arXiv:2001.08831](#).
- 1816 [31] **ALICE collab.**, *Multiplicity dependence of light-flavor hadron production in pp collisions at $\sqrt{s} = 7$ TeV*, *Phys. Rev. C* **99** (2019) 024906, [[arXiv:1807.11321](#)]. [DOI Link](#).
- 1818 [32] **CMS collab.**, *The Phase-2 Upgrade of the CMS Tracker*, tech. rep., CERN, 2018. CERN-LHCC-2017-009 ; CMS-TDR-014, [/cds.cern.ch/record/2272264](#).
- 1820 [33] **ATLAS collab.**, *Expected Tracking Performance of the ATLAS Inner Tracker at the HL-LHC*, tech. rep., CERN, 2019. ATL-PHYS-PUB-2019-014, [cdsweb.cern.ch/record/2669540](#).
- 1822 [34] **ATLAS collab.**, *Fluence distributions for ITk extended at 4 layout*, tech. rep., CERN, Oct. 2016. ITK-2016-002, [/atlas.web.cern.ch/Atlas/GROUPS/PHYSICS/PLOTS/ITK-2016-002/](#).